DEFORMATION AND FAILURE OF ADDITIVELY MANUFACTURED DUCTILE METALS WITH INTERNAL POROSITY

A Dissertation
Presented to
The Academic Faculty

by

John Carter Miers

In Partial Fulfillment
of the Requirements for the Degree
Doctor of Philosophy in the
George W. Woodruff School of Mechanical Engineering

Georgia Institute of Technology
December of 2021

DEFORMATION AND FAILURE OF ADDITIVELY MANUFACTURED DUCTILE METALS WITH INTERNAL POROSITY

Approved by:

Dr. Christopher J. Saldana Advisor
School of Mechanical Engineering
Georgia Institute of Technology

Dr. Tejas Murthy
School of Mechanical Engineering
Indian Institute of Science

Dr. Yan Wang
School of Mechanical Engineering
Georgia Institute of Technology

Dr. Bradley Jared
Department of Mechanical, Aerospace, and Biomedical Engineering
University of Tennessee, Knoxville

Dr. Thomas Kurfess
School of Mechanical Engineering
Georgia Institute of Technology

Dr. Brad L Boyce
R&D, S&E, Material Science
Sandia National Laboratory

Mr. David G. Moore
R&D S&E, Mechanical Engineering
Sandia National Laboratory

Date Approved: [August 10, 2021]

[To C. Sheppard Miers and Carter S. Miers, my beginning and end]

ACKNOWLEDGEMENTS

This journey was not possible without the help and support of many people. None more crucial than the support from my wife, Savannah. K. Miers. Thank you, Savannah for all of your support and hardships. I would like to thank my mother, Jane F. Miers for all that she has done for me in life. I would like to thank my father Charles S. Miers, for sharing with me his unique view on life and for his love over the years; you will always be missed. I would like to especially thank my advisor, Christopher J. Saldana, for his guidance along this journey. I want to give my gratitude to each member of my committee, David Moore, Bradley Jared, Tejas Murthy, Brad Boyce, Yan Wang, and Tom Kurfess. I am thankful that I can have such wide range of technical skill in this committee to review this work for its worth. I would like to thank my lab-mates Jaime and Elliott for their insight and humor over the years. Lastly, I give special thanks to Max, Joon, and Vinh, lab-mates and friends that are without equal. This work was partially supported by Sandia National Laboratories and the National Science Foundation through CMMI 185640.

TABLE OF CONTENTS

LIST OF TABLES

LIST OF FIGURES

SUMMARY

Interrupted in-situ tensile tests in a lab-based x-ray computed tomography machine were used to investigate the evolution of the strain field around internal defects. Digital volume correlation was utilized to directly determine local strain levels within the additively manufactured components in the vicinity of porosity defects. Effects of porosity on strain localization and eventual failure of the samples were evaluated. The influence of defect characteristics on the localization of strain was investigated. A non-local field analytical model for approximating the localization of strain based on defect geometry and loading direction was formulated. Correlation of the local characteristics and the non-local field with the local axial strain was evaluated. The non-local field, at both 1-to-1 voxel resolution and at the down sampled measurement point locations, was found to be the most correlated with the localization of strain followed by pore volume. Shallow neural network models were utilized to predict the local strain magnitude from the local characteristics in the undeformed frame and the magnitude of the tensile load applied to the component. Models were found to be accurate at predicting local strain magnitude before failure. With greater than 92% accuracy in predicting the variation in the measured strain field. Synthetic porosity alterations were applied to each sample to measure how small changes in porosity characteristics would affect the accumulation and distribution of strain in components. Volumetric alterations were found to have the greatest effect on magnitude regionally, but translations of the porosity were found to have a greater effect on the intervoid ligament location and shape and the overall likely path of ductile rupture.

The direct measurements of strain field evolution in the present study established understanding regarding how internal defect structure characteristics influence the evolution of the local strain fields for additively manufactured components. Early onset of failure was found to be associated with the availability of neighboring porosity in the vicinity of large defects that allowed for rapid progression of the fracture path. This high-fidelity characterization and the associated phenomenological observations have bearing for supporting validation of numerical modeling frameworks for describing failure in these materials. The correlations established between local-characteristics and local-strain provide valuable information to designers to understand the hyperplane of specifying porosity tolerances. In addition, these correlations can improve the implementation of locally changing material properties and adaptation of constitutive relationships in numerical modelling frameworks of highly porous AM materials. The results of the non-local field analysis allow for the identification of strain localization hotspots and thus identifies areas that are more critical to model with finite element techniques. Utilization of the high-fidelity characterization and non-local fields via machine learning provides a procedural framework for the use of machine learning in component assessment and qualification. Additionally, predictions on altered data allowed for the generation of valuable engineering knowledge for understanding local porous material behavior.

CHAPTER 1. BACKGROUND

1.1 Additive Manufacturing

1.1.1 Additive Manufacturing

The American Society of Mechanical Engineers defines additive manufacturing (AM) as the "process of joining materials to make objects from three-dimensional (3D) model data, usually layer by layer," [1]. There has been extensive growth and development in AM technologies since the mid-1980s and the list of AM processes now includes: stereolithography (SLA), fused deposition modeling (FDM), Direct Energy Deposition (DED), inkjet printing, and selective laser melting (SLM) processes like powder bed fusion (PBF) to name a few [2]. Components made by AM technologies are broken up into a series of cross-sections of the component geometry that are then constructed in series by an AM process. This allows for complex features and internal structures to be fabricated with relative ease compared to more traditional manufacturing processes [3]. In addition to those already discussed, other advantages AM offers over traditional manufacturing methods include: significantly less material waste due to the fabrication of a near net-shape part from a single setup, parts can be made on-demand for quick turnarounds and little to no tooling cost, and weight reduction of components through the use of topology optimization and embedded lattice frameworks that are only feasibly producible using AM technologies [4]. Thus, it is clear that AM, in particular

metal AM, stands to revolutionize manufacturing industries, however there are a few drawbacks to AM that are preventing its widespread adoption.

While additive manufacturing (AM) technologies such as laser powder bed fusion (LPBF) are being used in industrial practice, qualification of such approaches is still relatively nascent, and parts based on such frameworks require significant empirical testing. Of particular importance to qualification are the criticality of defects that form during the AM process [5]. Metal AM is subject to pervasive manufacturing defects that can differ significantly from those common in traditional fabrication techniques like casting [6] and, consequently, their effect on mechanical behavior is not well understood [7, 8, 9]. Defects associated with AM processes can affect the mechanical properties of these components. The problem is complicated by the fact that laser and scanning parameters, powder quality, size and distribution, as well as surface chemistries of the wetted melt pools all play a role in influencing the quality of the fused material [10, 11].

1.1.2 Defects in AM

Given that there is a link between defect structure and mechanical performance in porous components, identification of defects prior to use is necessary to ensure component safety [12]. Common surface defects in AM parts include cracking, un-melted powder particles and roughness [13]. However, other surface defects such as keyhole porosity can be

devastating to the mechanical performance of the part [14, 15]. In the majority of research discussing internal defects for AM components is often just reduced to a discussion of their porosity, although for technical purposes internal can also include microstructure anomalies and inclusions. These porosity analyses often only focus on the size, the volume fraction, distribution, and location of pores within the material volume, but other parameters like sphericity, compactness, and orientation are mentioned in a few works [14]. For more complex defect characterizations, some have turned to expensive commercial software solutions like Volume Graphics [16, 17] and Avizo [18]. Note: Due to the large number of AM processes and the differences in their resultant mechanical processes, for the remainder of this proposal AM techniques/processes/methods and the properties associated with AM components will be in reference to metal powder techniques with a focus on L-PBF.

Among the defects that are found in AM parts, inclusions arise from impure metal powders, contamination to the powders from exterior sources, and oxidation [19]. While inclusions are typically orders of magnitude smaller than the porosity discussed in relation to AM, it is at inclusion sites that void nucleation commonly occurs [9]. There are 2 primary types of porosity that occur in AM components: gas porosity and porosity due to lack of fusion. Gas porosity is most commonly attributed to entrapped shielding/inert gas in the material matrix. Three mechanisms give rise to the entrapped gas: 1) to high powder flow rates and thus lower specific energies of the melt pool in DED processes, 2) gas trapped inside the powder particles from the start, 3) Marangoni flow [20]. In fact, components

made from powders produced via gas atomization (GA) show 3 times greater porosity that those produced by plasma rotating electrode process (PREP) [21]. Lack of fusion (LOF) porosity is caused by an insufficient energy in the melt pool and thus an inability to fully melt powder particles. Due to the layer-wise build method of AM, the un-melted particles from the previous pass can compound with the next layer of powder deposited causing LOF pores to typically be larger and more tortuous that gas porosity [22]. Geometric anomalies are also common in AM. The most common type of geometric abnormality is due to melt pool flow due to gravity, but other common sources are overgrowth due to excess heat in the build volume and balling behavior in the melt pool powder interaction [23]. Geometric abnormalities are most often associated with dimensional inaccuracies when measuring AM parts, so a common work around has been the use of post processing of AM components to achieve their net shape. For more complete reviews of additive manufacturing defects, the works of H. Taheri et al. [20] and F. H. Kim and S. P. Moylan [24].

1.1.3 Qualification of Additively Manufactured Components

Inspection external to the part usually consists of measurements of part dimensions and surface topology, but in the case of AM components should also include attention to surface roughness [25, 26, 27]. Given that AM parts are subject to large amounts of internal defects and that surface inspection techniques, such as coordinate measurement machines

(CMM) and structured light scanning, are limited in that they can only measure surface topology [28]. As discussed above AM components are subjects to high levels of internal defects, as such proper inspection of AM components requires inspection of internal malformities. The metrology of internal features can be functionally divided into two categories: destructive and non-destructive techniques. Destructive techniques require some form of cutting, deforming, eroding, or otherwise destroying of a part to create or reveal internal surfaces for measurement. By contrast, non-destructive techniques do not require destruction of the component measured, although destructive processes can be brought into non-destructive techniques as discussed later with in-situ experiments. Common destructive techniques for internal inspection are fractography, and serial sectioning [29], but due to the nature of the present work these techniques are not employed. Similarly, the non-destructive technologies of ultrasonic and thermographic metrology are also not used because they are not typically used to produce 3D reconstructions of components [30, 31]. In terms of research attractiveness by far the most popular non-destructive technique for inspecting additive manufactured parts is X-ray computed tomography (XCT). XCT has been used to measure defects such as cracks, inclusions, pores, and geometry variations in components [32, 33]. XCT has also been used to show the effects of defects and inhomogeneities on lattice struts [34], and to determine the damage evolution and morphological changes in stainless steel components [35]. XCT is further set apart from other techniques by its application in digital volume correlation

(DVC) analysis to quantify the deformation of an object between scans [36], however, the application of DVC to AM components is still extremely scarce [14].

Originally developed for medical applications, XCT is capable of obtaining full 3D reconstructions of the internal and external structures of given specimen. Industrial XCT systems consist of 3 primary components: an X-Ray source, 4-axis positioning system (X, Y, Z, C) for the component, and a flat panel detector. For each increment of the rotational stage, a radiograph of the x-ray energy at the detector is recorded (each radiograph can be averaged, summed, or otherwise extracted from multiple frames at each increment). By allowing for at least a full Nyquist-Shannon sampling of radiographs from the objects 360° rotation, a reconstruction in the form a voxel volume can be obtained [37, 38]. A more thorough review of the principles and parameters behind XCT can be found in [39, 40].

1.2 Modelling Strain Localization and Ductile Failure

Community efforts such as the Sandia Fracture Challenges [41, 42, 43] have tried to bridge the gap between bulk experimental measurements, such as those taken from XCT analyses, and computational modelling of deformation. The third Sandia Fracture Challenge found that local strain rates were more critical than the loading rate during failure [43]. Other studies have found that porosity can lower the strength of the component in proportion to the reduction in cross-section due to porosity [44], and that AM components

often have greater yield strength than their wrought alternatives [45]. One commonality in all this research is that the presence of defects lowers the elongation to failure of components under tensile loading [35, 46]. Still other efforts in recent years have focused on how advanced nondestructive measurement tools and machine learning can be used to understand and predict strain behavior in defect driven localization. Kim et al. have used XCT to peer inside of AM components and apply the internal structures to unique numerical models for the components scanned [47], additionally he has employed 3D DIC to monitor the deformation of components and develop models with this data [32]. Leicht et al. also applied DIC to study advance material deformation [48]. Dressler et al. used XCT to investigate inhomogeneities in AM struts in terms of strain localization [34].

Taking a step away from the realm of AM, Bourcier et al. in 1984 showed that strain in porous solids can be understood in terms of both bulk porosity and local porosity effects [49]. Bulk properties are characteristics like the ratio of pore volume to matrix volume for either the whole component or for a section of the component. These bulk properties can be used to understand the certain aspects of the mechanical behavior: increasing pore volume fraction results in lower bulk flow stress [49]. Local porosity effects occur on the scale of the pores and include things like the effect of internal void ligaments, internal necking and highly localized plastic zones in this interpore space [50, 51]. It is explained

in the ensuing that these local effects are responsible for the overall reduction in the parts ductility.

1.3 The Gap

The arbitrary geometry and non-uniform distribution, size, and orientation of pores and other defects in AM components complicate modeling efforts. Local deformation and strain are driven by these features and are thus tied to the spatial distribution and length scales of the local microstructure. However, the majority of 2D and 3D micro-mechanics investigations are performed with simple geometry and assumptions of distribution uniformity [35, 52, 53, 54]. These models fail to capture the spatial correlation and complex contributions of real 3D microstructures, especially highly porous micro-structures like those of AM. There are often mixed, cooperative, and competitive mechanisms of ductile rupture occurring in real components that FE-based simulations often miss due their assumptions of periodic defect distributions and constitutive law modifications based on models that use simple defect geometry [55]. As such, these models are unable to accurately assess the response of real multi-length scale and complex geometry microstructures. Homogenization of this kind fails to account for the influence that microstructure at greater length scales have on the response at small length scales. While there is some work in the area of incorporating digital image analysis into FE modeling [32, 56], there is surprisingly little research in this area for void driven microstructure

inhomogeneity [57, 58]. Given that AM components are highly porous and include heterogeneities and defects at multiple length scales, modeling with periodic/homogeneous distributions, or with simplified geometries, cannot capture the coupling or unique response of these materials locally.

1.4 Research Proposed

1.4.1 Research Question

The proposed research will address the research question: “What are the critical defect characteristics (e.g., volume, gap, sphericity, compactness, orientation) that influence the damage accumulation and failure behavior of an AM component?”

1.4.2 Research Objectives

The goal of the research described herein is to shed light on that question. The proposed study will center on: (1) in-situ study of the evolving defect field in terms of morphological parameters and deformation variables (e.g. displacements and strains), (2) comprehensive analysis and description of the defect field in AM components, (3) development analytic and machine learning models for predicting the localization of strain as a function of the defect field characteristics, and (4) determination of the role of simulated AM defect changes on the localization of strain. This research will provide

robust tools for the analysis and qualification of defect criticality in AM components and uncover what characteristics of defects drive their failure. In addition, it will provide the foundation for the greater implementation of the proposed model.

1.5 Organization of Dissertation

The dissertation herein is organized into the following 4 sections. First the need for, the method of performing, and the results of the in-situ experiments are discussed in 0. Next, the segmentation, extraction, and quantification of defects is detailed in CHAPTER 3. Additionally, the results of the extracted features are presented therein, and the correlation of these features with the localization of strain is examined. CHAPTER 4 is devoted to the modeling and prediction of local strain from the data gathered in the previous 2 chapters. The conclusions of these efforts are summarized in CHAPTER 5. Lastly, supplementary figures are provided in Appendix A and supplementary tables are provided in Appendix B.

CHAPTER 2. DEFORMATION FIELDS IN TENSILE LOADING OF AM COMPONENTS

2.1 Introduction

Due to the fact that AM parts are subject to large amounts of internal defects, surface inspection techniques and most other non-destructive inspection techniques are generally insufficient [30, 31]. The exception being X-ray computed tomography (XCT). XCT has been used to measure defects such as cracks, inclusions, pores, and geometry variations in metal AM components [32, 33]. XCT has also been used to show the effects of defects and inhomogeneities on lattice struts [34], and to determine the damage evolution and morphological changes in stainless steel components [35, 47]. Kim et al. characterized the failure evolution for 17-4 stainless steel with engineered octahedral defects and LOF porosity. In-situ tensile testing with XCT measurements enabled FE based analysis of high stress concentrations associated with internal surfaces of the defects [47]. In-situ laminography has enabled several authors to study the mechanisms of failure in metal alloys. Artificial voids, approximated by machined holes, were used to study the strain in intervoid regions. In this study, Bulijac et al. made use of in-situ laminography scans obtained from a beamline at the European Synchrotron Radiation Facility (ESRF) in combination with digital volume correlation to investigate the effects of void arrangement

on damage in graphite cast iron [59]. In another study, Bulijac et al. investigated the damage mechanisms of a work hardened 2198 T3 aluminum alloy just ahead of its notch and noted that slanted strain bands with limited void nucleation around inclusions were to be found in the failure region [60]. In shear loading conditions, Roth et al. found evidence of damage nucleation and evolution using in-situ laminography at a synchrotron X-ray line [61]. In addition, there is a growing field of study using interrupted in-situ experiments to study the structural changes under load [62, 63] in both synchrotron and lab-based XCT systems. In-situ experiments have been used to compare the growth of defects to that predicted by void growth models [64]. Experiments by Croom et al. used in-situ XCT to study the mechanisms of ductile rupture in high-purity Cu [55]. They found that void growth and overall failure resulted from a collaborative process of damage mechanisms highly dependent on the local features and distribution of voids.

In the present study, interrupted in-situ tensile tests in a lab-based XCT machine were used to investigate the evolution of the strain field around internal defects and examine their role in the macroscopic deformation of AM tensile coupons. This research focuses on the defects generated from LPBF of 316L stainless steel and employs digital volume correlation (DVC) [65] of in-situ deformations of AM components using a custom-built loading frame to extract both deformation and strain fields of the components as they undergo uniaxial tensile loading. In the ensuing, the morphological evolution of AM

defects under mechanical loading are quantified and discussed in the context of effects on macroscopic tensile response.

2.2 X-Ray Computed Tomography

2.2.1 Physics of X-Ray Imaging

X-rays are a form of electromagnetic radiation with shorter wavelengths and higher energy than UV rays. A significant feature of x-ray radiation is its ability to penetrate materials as described by Beer's Law:

$$I = I_0 e^{-\int \mu(s) ds} \tag{1}$$

where I is the intensity after passing through the material, commonly referred to as the transmitted intensity, I_0 is the intensity of the x-ray beam, s is the path the ray follows, and $\mu(s)$ is the linear attenuation coefficient along the path [66]. The above equation explains how a ray passing through different materials or regions of varying absorption/attenuating properties will lose intensity. This attenuation of the rays allows for information about the material they passed through to be obtained via radiographs.

2.2.2 Three-Dimensional Reconstruction

As described by the path dependence of Equation (1), the 3-dimensional information about the object imaged with x-rays is lost in the 2-dimensional radiographic output. However, the breakthrough of 3-dimensional x-ray imaging came in 1973s in the introduction of computed tomography or computerized transverse axial tomography (CAT) [67, 68, 69]. The linear attenuation coefficient at each point in a radiograph is derived as shown below [70].

$$\ln\left(\frac{I}{I_0}\right) = -\int \mu(s)ds \tag{2}$$

The problem of the 3D reconstruction can be thought of as a problem of solving for the value of $\mu(s)$ at every point within the 3D object [66]. As it is not the focus of this work, the full details and complexity in the 3D reconstruction of data obtained in the form of 2D radiographs can be found in Ref. [70].

It is necessary to note that laboratory CT systems are not monochromatic or ideal in environment and artifacts commonly occur in the reconstructed volumes generated from XCT scans. Common reconstruction artifacts include: streaks, edge blurring or partial volume, rings, noise, and beam hardening. Common causes of these artifacts is having overly attenuating materials in the field of view, issues with resolvability and scale of the physical features, defective or varying detector elements, low signal-to-noise ratio, and the polychromatic beam of a laboratory source [71, 72, 73, 74]. Uncertainty in the data

provided by XCT is an ongoing area of research, but among the most common calibration techniques is to compare the part scanned to a calibrated part scanned [75]. One common approach is to simply measure the part with another nondestructive measurement system and compare the results, CMMs provide a source of external feature measurement.

2.3 Methodology

2.3.1 Samples

In this research, tensile tests were performed on additively manufactured 316L stainless steel samples. AM billets were manufactured on a 3D Systems ProX DMP 200 powder bed fusion machine equipped with a Yb-fiber laser (continuous wave – 1070 nm wavelength). Process settings were set to 100 W nominal power and 100 µm nominal spot size. The scan speed was set at 1400 mm/s with a 50 µm hatch spacing and a hexagonal scan pattern was used. The build chamber oxygen was kept at a nominal 1000 ppm. The layer height was kept at 30 µm. Virgin 316 stainless steel powder (3D systems) was used to build the samples, where the volume-based particle size distribution was Dv10 = 13.6 µm, Dv50 = 21.1 µm, and Dv90 = 32.7 µm, measured via laser diffraction with a Malvern Mastersizer. After the AM billets were built, the samples were wire electrical discharge machined (wire-EDM) to final high-throughput tensile (HTT) geometry from the AM billet. The HTT samples each have a square gage region 1 mm x 1 mm x 5 mm in cross-

section and length. The sample geometry allowed for pocketed tensile grips that would ensure no slipping of the specimens during testing, similar to the high throughput system in Ref. [76].

2.3.2 Experiments

2.3.2.1 In-Situ Testing Rig

For interrupted loading experiments, a Zeiss Metrotom 800 system was used along with a custom-built tensile loading stage, shown in Figure 1(a). The tensile loading system rested on the rotation stage of the XCT system and, as such, the system rotated with the sample during the scan. The system was designed with in-line grip assemblies that do not occlude the sample during the scanning process. Load was measured in-line using a Futek LCM300 load cell with a 4448.22 N (1000lbf) capacity and a 0.1779 N (0.04 lbf), converted from lbf, sensitivity located below the lower tensile grip assembly and above the linear displacement arm of the tensile stage motor. To obtain a high-quality tomographic reconstruction, the support frame for the tensile jaws was made to be radially symmetric and of clear acrylic so to have a low impact on attenuation of the x-ray beam. The motor has a 38.1 mm (1.5 in.) full stroke and can exert a linear load of up to ~2224.11 N (500 lbf) and a displacement resolution of 4.9609 x 10^{-5} mm per sub-step [77]. To aid in the alignment of the system, the tensile grips were designed to be self-aligning once the system

was under tension. Both grips were mounted on ball joints for angular adjustment and the upper grip floated in its assembly for translational alignment. This alignment process can be seen for all samples in Appendix A.1 as montages of a single angle's x-ray projection from the scanning process. The custom in-situ tensile system and the sequence projections for sample 1 and 4 are shown below in Figure 1.

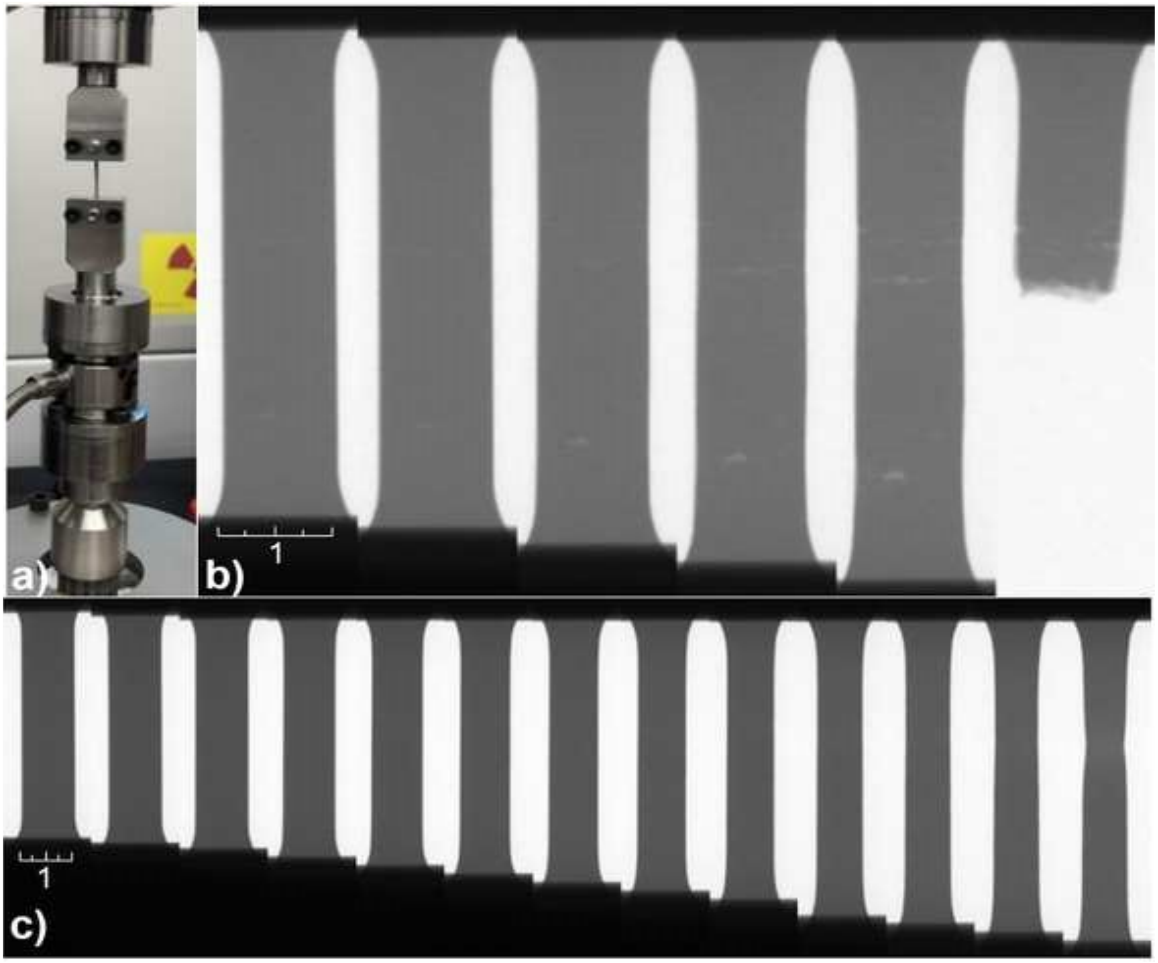

Figure 1. (a) Schematic of in-situ tensile loading frame and sequence of x-ray projections for the deformation of (b) Sample 1 and (c) Sample 4.

2.3.2.2 X-Ray Computed Tomography Cabinet and Scanning Parameters

XCT scans were run at the end of each deformation step to capture the internal and external changes in the sample geometry. These volumes were reconstructed from x-ray

projections taken over one complete rotation of the sample geometry. Each scan was carried out with the same settings: 130 kV and 30 μA of beam power, and 1 Hz frame rate. For clear sampling 1200 projections were taken per scan with 3 frames averaged per projection to improve the signal-to-noise ratio. To reduce the variation in the energy signature, a copper filter was placed in front of the x-ray source to absorb the low energy rays. Each scan required approximately 50 minutes to complete and had a resolution of 8 μm per voxel. Reconstruction volumes were 1167 x 1168 x 1474 voxels or approximately 9.336 x 9.344 x 11.792 mm in dimension. Reconstructed volumes were cropped before analysis to a size of 391 x 391 x 891 voxels.

2.3.2.3 Testing Parameters

The interrupted tensile tests were performed using displacement control and a step size of 0.18 mm. This step size was chosen to provide approximately 10 deformation steps to part failure, based on the percent elongation observed for early samples. The motor was driven at 0.01 mm/s with an acceleration and deceleration of 0.01 mm/s^2. Before each deformation step, the load cell was set to sample and record at 100 Hz. Recording of the load was not terminated until after the deformation step was completed. It was necessary to terminate the measurement of load, as the presence of the wired connection would prevent the closure of the x-ray cabinet. There were some signs of load relaxation, but they could not be recorded over the length of the scan.

2.3.3 Analysis

2.3.3.1 Correlation Techniques

Correlation techniques are used to track the displacement of regions of space. This is achieved by finding the pattern in the displaced data that best matches the pattern of the region in the undeformed data. These two data sets are sometimes referred to as the current (g) and reference (f) data sets, respectively. The quality of match between two regions of space is defined by a simple cost function: $F = g - f$. Unless the data moves with uniform rigid body motion, this correlation must be computed locally. This yields well to computational correlation, either digital image correlation (DIC) or digital volume correlation (DVC), for discrete representations of data with 2D pixels and 3D voxels, respectively. For correlation to be meaningful there must be an underlying pattern or texture that varies with that varies spatially.

2.3.3.2 Digital Volume Correlation

Digital volume correlation (DVC) was employed in the present work to measure the deformation between each XCT scan. This technique determines the 3D displacement and strain field measurements by maximizing the correlation between a gridded sub-volume of the reference volume and its associated interrogation sub-volume in the deformed volume. The DVC method described by Ref. [36] was implemented in the

present study. This implementation begins with an approximation of rigid body displacements (u, v, w) of the gridded sub-volumes from the reference volume (f) to integer locations in the deformed volume (g). This is obtained by finding the maximums of the cross-correlation of the sub-volumes in the frequency domain and yields displacements that are accurate to the voxel scale. Then sub-volumes registration is finalized with a non-rigid optimization of the sub-voxel displacements $(\delta u, \delta v, \delta w)$ and strains $(\varepsilon_{xx}, \varepsilon_{yy}, \varepsilon_{zz}, \varepsilon_{xy}, \dots)$ of the linear displacement model shown in Equation (3):

$$\begin{bmatrix} x_i' \\ y_i' \\ z_i' \end{bmatrix} = \left(\begin{bmatrix} x_0 \\ y_0 \\ z_0 \end{bmatrix} + \begin{bmatrix} \Delta x_i \\ \Delta y_i \\ \Delta z_i \end{bmatrix} \right) + \left(\begin{bmatrix} u \\ v \\ w \end{bmatrix} + \begin{bmatrix} \delta u \\ \delta v \\ \delta w \end{bmatrix} \right) + \begin{bmatrix} \varepsilon_{xx} & \varepsilon_{xy} & \varepsilon_{xz} \\ \varepsilon_{yx} & \varepsilon_{yy} & \varepsilon_{yz} \\ \varepsilon_{zx} & \varepsilon_{zy} & \varepsilon_{zz} \end{bmatrix} \begin{bmatrix} \Delta x_i \\ \Delta y_i \\ \Delta z_i \end{bmatrix} \tag{3}$$

where x_o, y_o, z_o and $\Delta x_i, \Delta y_i, \Delta z_i$ are the center of the sub-volume and the distance to each voxel, i, within the sub-volume, respectively. This process uses an iterative least-squares framework, shown in Equation (4), to solve a non-linear least-squares formulation of the objective function (F), to update a parameter vector (p) [36].

$$p^{k+1} = p^k - \frac{\nabla F(p^k)^T F(p^k)}{\nabla F(p^k)^T \nabla F(p^k)} \tag{4}$$

Also known as the residual field [65], F is a scalar metric of how well the reference sub-volume and the registered deformed sub-volume match for each voxel (i). The objective function is shown below in Equation (5):

$$F(p^k) = g\left(x_i'^k, y_i'^k, z_i'^k\right) - \alpha^k f\left(x_i^k, y_i^k, z_i^k\right) - \beta^k \tag{5}$$

where α and β are intensity correction factors used to adjust for any intensity variations between scans and $p^k = \left\{\delta u^k, \varepsilon_{xx}^k, \varepsilon_{xy}^k, \varepsilon_{xz}^k, \delta v^k, \varepsilon_{yx}^k, \varepsilon_{yy}^k, \varepsilon_{yz}^k, \delta w^k, \varepsilon_{zx}^k, \varepsilon_{zy}^k, \varepsilon_{zz}^k, \alpha^k, \beta^k\right\}^T$ is the parameter vector representing the values of the unknowns at iteration k. At each voxel, i, the displacement and strain values of parameter vector (p_i) are updated with the quotient term of Equation (4). $\nabla F_i(p^k)$ is given as:

$$\begin{aligned}
&\nabla F_i(p^k) \\
&= \{g_{xi}^k \ \Delta x_i g_{xi}^k \ \Delta y_i g_{xi}^k \ \Delta z_i g_{xi}^k \ g_{yi}^k \ \Delta x_i g_{yi}^k \ \Delta y_i g_{yi}^k \ \Delta z_i g_{yi}^k \ g_{zi}^k \ \Delta x_i g_{zi}^k \ \Delta y_i g_{zi}^k \\
&\quad \Delta z_i g_{zi}^k \ - f_i \ - 1\}
\end{aligned} \tag{6}$$

$$g_{xi}^k = \partial g(x_i'^k, y_i'^k, z_i'^k)/\partial x$$

$$g_{yi}^k = \partial g(x_i'^k, y_i'^k, z_i'^k)/\partial y$$

$$g_{zi}^k = \partial g(x_i'^k, y_i'^k, z_i'^k)/\partial z$$

To assign a singular value to the registration of each deformed sub-volume, the zero-mean normalized cross-correlation (ZNCC) coefficient is used [78]:

$$ZNCC = \frac{\sum_{i=1}^{n}\left[f_{(x_i,y_i,z_i)} - \overline{f}\right]\left[g_{(x_i',y_i',z_i')} - \overline{g}\right]}{\sqrt{\sum_{i=1}^{n}\left[f_{(x_i,y_i,z_i)} - \overline{f}\right]^2}\sqrt{\sum_{i=1}^{n}\left[g_{(x_i',y_i',z_i')} - \overline{g}\right]^2}} \quad (7)$$

where $\bar{f}$ and $\bar{g}$ are the mean intensity values of the sub-volumes f and g, respectively. The method of DVC used in this paper has been validated by B. Pan et al. [36] and the implementation of the algorithm by H. Qiao et al. [79].

2.3.3.3 Pre-processing of Data

As calculations at voxels located outside of the component body lack textural information for correlation, a mask of the component region was used to identify and remove subsets that had less than 60% of their volume within the mask. The high degree of subset overlap reduces loss of data near the mask boundary. During the process of pruning subsets based on registration quality, subsets were divided into those completely within the mask and those intersecting the mask boundary. The latter group was held to a higher threshold standard as the steep gradient between the component body and the background voxels may bias update of displacements.

2.3.3.4 Analysis Parameters

The DVC method described above was implemented in an incremental fashion where the deformed volume from the previous step is used as the reference volume for the current step. This allowed the analysis to account for the large deformations of the material system and continuity was maintained with point tracing. The implementation used herein had cubic subsets spaced every 7 voxels with subset full width defined as 35 voxels. The high overlap allows for smoother results less susceptible to noise and high grid point frequency ensures that the technique captures even small changes between voids. The porosity and natural textural variations in the samples provided the inherent texture field for the DVC correlation.

2.3.3.5 Post-processing and Upscaling

Figure 2 shows the defect structure for Sample 1. Displacement was calculated using the iterative least-squares approach, followed by the strain calculated with the pointwise least-squares approach, as in Ref. [36]. The strain calculation window was set to span 5 displacement field points in width and to be calculated at every displacement field point. For strain windows near the boundary of the mask, only points within the mask were used to calculate the strain field.

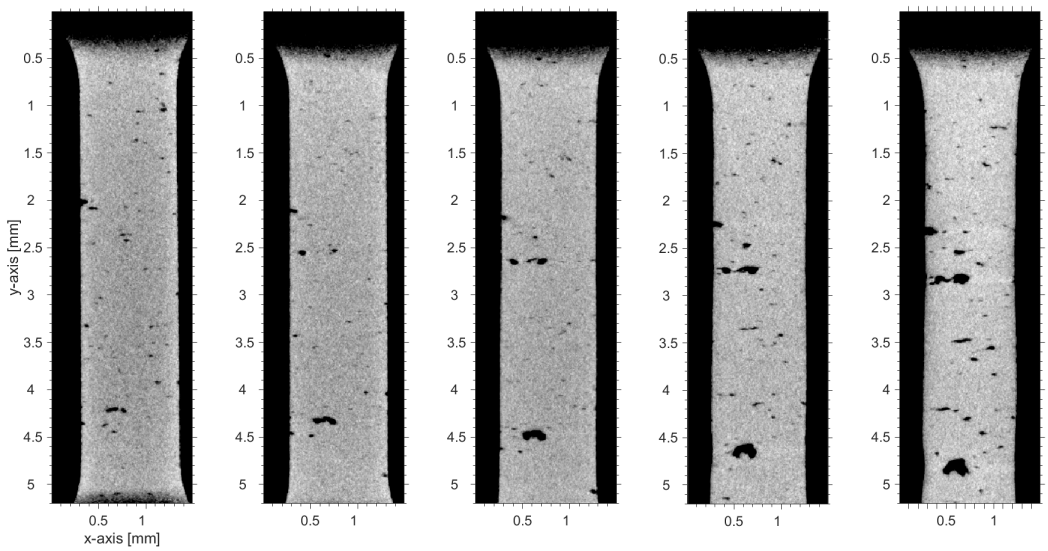

Figure 2. Inherent texture field and microstructure of Sample 1 at each interrupting measurement of the deformation process.

Displacement and strain field results were mapped to both the deformed and the reference frames of the analysis, such that final strain near failure can be attributed to a region of the undeformed sample geometry.

2.4 Results

2.4.1 Testing Results

In total 34 scans were taken for in the loaded states of the samples. The break down was 5 for sample 1, 7 for sample 2, 9 for sample 3, and 13 for sample 4. The reference or undeformed state for each sample was defined as the first scan obtained after the load cell

reads positive loading, implying the system had crossed into tension and the weight of the bottom platen was no longer causing minute compression on the load cell. And by the settling of the sample into a stable position within the jointed tensile grip system. Since the motor and load cell systems were decoupled capturing stopping the motion just after the transition to positive load was a manual operation. User error resulted in a slightly higher initial load for the undeformed state of sample 1 than what was typically seen for samples 2-4, but there was technically variation in the initial load of all 4 samples. These initial load differences are reflected in the initial stress at the minimum cross-section as shown by Figure 3 below, however due to the nature of the measurement being with respect to the reference scan this is not reflected in the reported global strains of Figure 3.

2.4.2 Analysis Results

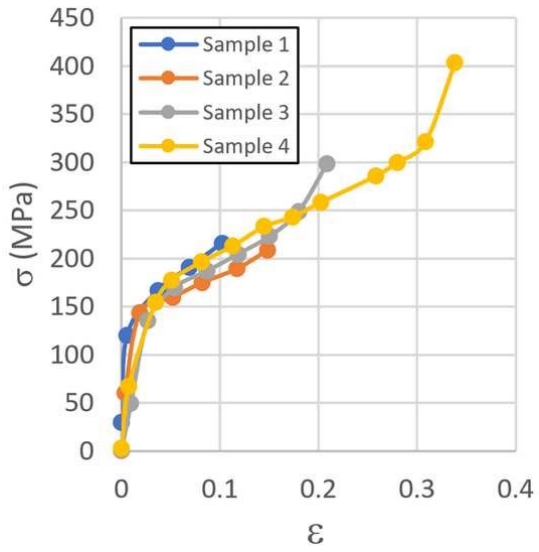

Figure 3. Stress Response versus global axial strain.

Figure 3 shows stress-strain response for each specimen until fracture. In this data, the global strain was evaluated through gage length measurement on x-ray projections taken orthogonal to the sample front face. From the data, little variation was present in terms of yield strength across these specimens. However, Sample 4 exhibited higher elongation to failure of $\varepsilon_f = 0.3363$ compared to that of Samples 1, 2 and 3 which had elongation to failure results of $\varepsilon_f = \{0.1037, 0.1800, 0.2114\}$, respectively.

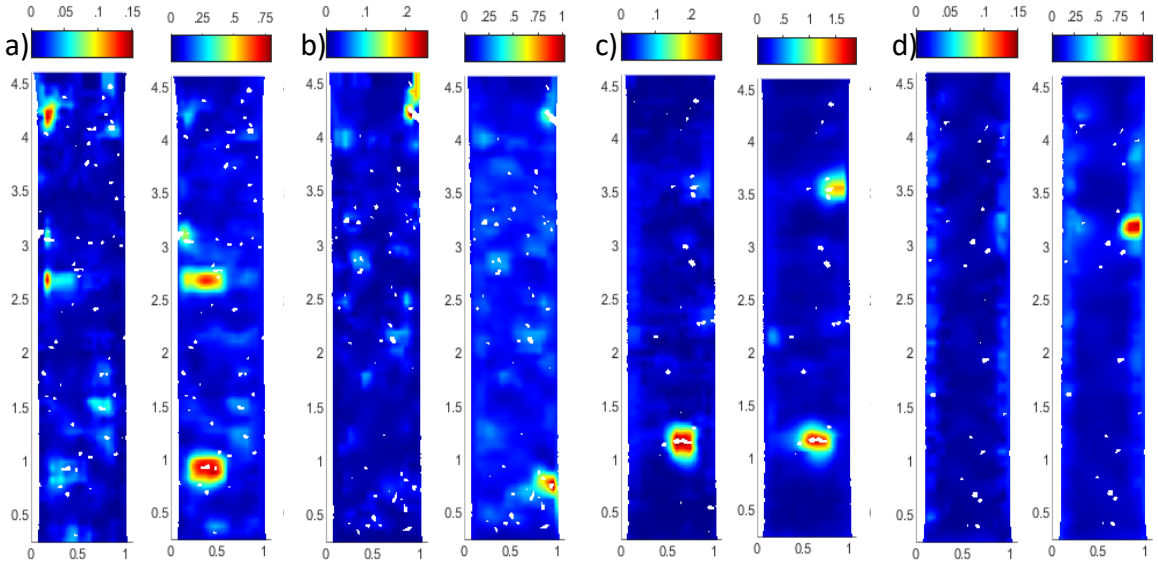

Figure 4. Initial (left) and final (right) local axial strain in the reference frame as calculated by DVC. a) Sample 1, b) Sample 2, c) Sample 3, d) Sample 4.

The results in Figure 4 above show the distribution of strain for the first measurement and last measurement before failure, all results are shown mapped to the reference or undeformed configuration. It was typical for strain to group around large (volume-wise) porosity especially porosity that is connected to the outer surface are apparent. Results are shown relative to the undeformed configuration to provide insight into the role of unique initial porosity in the localization of strain that ultimately leads to failure. As other works have shown, the elongation to failure in the samples is inversely proportional to their total void volume fraction [80].

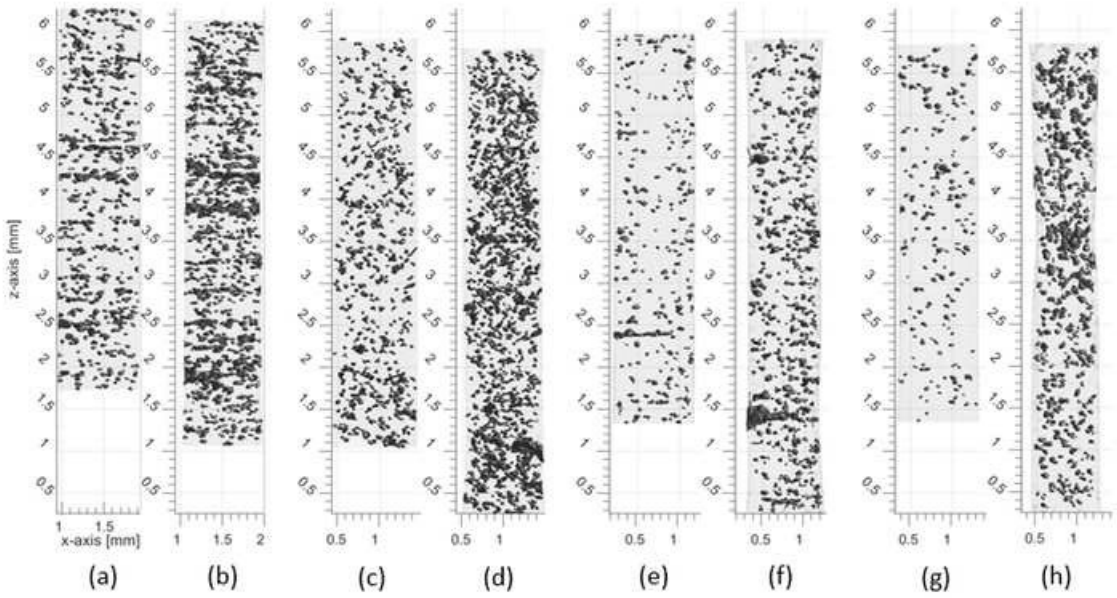

Figure 5. Initial and final defect fields for (a, b) Sample 1, (c, d) Sample 2, (e, f) Sample 3, and (g, h) Sample 4.

Figure 5 shows the distribution of porosity prior to deformation and just prior to mechanical failure for each of the samples under study and Table 1 summarizes the evolution of porosity before (φ_i) and after (φ_f) deformation. From the figure, there are clear differences in the size, grouping, location, and amount of porosity in each sample. In terms of overall distribution, Sample 1 had two major groupings: (1) an upper site located at approximately z = 4.20 mm contained two large pores 0.2650 mm and 0.5151 mm in maximum length with no connection to the surface of the component and (2) a lower site at z = 2.50 mm that consisted of a single large pore 0.3811 mm in maximum length with

surface connectivity. Sample 2 had one major pore 0.2335 mm in maximum length located at z = 5.25 mm, and a grouping of smaller elongated pores 0.0525-0.2799 mm in maximum length range near the base of the component at z = 1.50 mm. Samples 3 and 4 had singular major regions of porosity, with a large surface pore 0.3709 mm in maximum length at z = 2.35 mm in Sample 3 and 0.2278 mm in maximum length at z = 4.30 mm in Sample 4.

Table 1. Summary of the porosity evolution in deformed samples.

Sample	Porosity, φ		Pore volume, $V_{pore,\ max}$ (mm^3)	Axial position of major porosity groupings, z (mm)
	φ_i	φ_f		
1	1.32%	2.65%	0.0030	[4.20, 2.50]
2	0.82%	1.93%	0.0009	[1.50, 5.25]
3	0.49%	1.65%	0.0029	2.35
4	0.38%	1.91%	0.0007	4.30

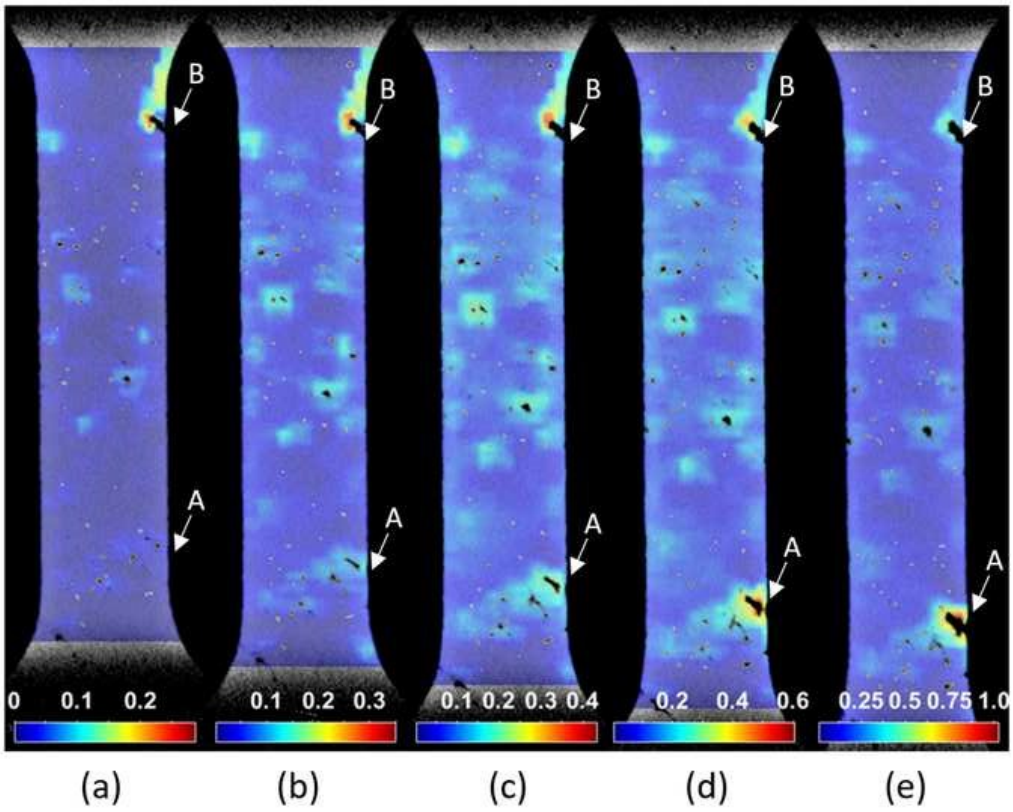

Figure 6. Local strain ε_{zz} overlaid on the gray-scale cross sections of Sample 2 for global axial strains of (a) $\varepsilon = 0.0187$, (b) $\varepsilon = 0.05252$, (c) $\varepsilon = 0.08772$, (d) $\varepsilon = 0.1190$, and (e) $\varepsilon = 0.1503$.

The strain distribution within each sample can be directly compared with the internal defect fields obtained from the tomographic imaging scans. Figure 6 shows a montage of y-z grayscale slices during tensile loading of Sample 2. In the figure, each grayscale slice is overlaid with a color mapping of the corresponding axial strain ε_{zz} at that section. From the cross-sectional images, the size of individual pores clearly increased

during the loading process and coalescence/growth was observed, particularly in the lower half of the sample. In one case, the pore, marked as A in Figure 6, eventually increased in extent such that it broke through to the free surface of the sample. It can be seen that local strain intensity was directly affected by porous defects in the sample. The strain field makes it clear that local strain intensity in the vicinity of pores was greater than that of the global axial strain and that this disparity only grew more pronounced as the parts approached failure. This corresponds well with similar findings for cast materials under tensile load [44, 81]. Clearly, pore size and surface connectivity affected local strain intensity to the point of failure as can be seen by additional strain-mapped cross-sections similar to Figure 6 above found in Appendix A.2. Additionally, secondary accumulation of strain between locations of adjacent porosity (inter-void strain) can be clearly seen in the deformation occurring in Sample 2. Similar observations have been made in the literature, sometimes referred to as inter-void necking or inter-void plasticity [82]. From the present data, the evolution of the failure in the sample appeared more affected by pore-pore interaction rather than the relative size of the pores. For example, an initially large pore with connectivity to the exterior surface, marked as B in Figure 6, was initially the location of the greatest axial strain at $\varepsilon_{zz} = 0.25$. Despite this initially high localization, as the deformation process progressed, the grouping of pores in the vicinity of pore A grew to exhibit the highest total $\varepsilon_{zz} = 1.0$.

The impact of pore-pore interaction in the vicinity of near-surface porosity was also evident in the progression of failure for Sample 4, as is shown in Figure 7 below. As strain localizations were shown above to be concentrated in the vicinity of pores, a clearer identification of all the pores contributing to overall failure was made by visualizing the local strain field in the vicinity of a pore by strain mapping on to the pore surface. A surface pore at approximately z = 4.25 mm, marked as C in Figure 7, had an initially high strain of ε_{zz} = 0.054. Compared to the evolution of pore A in Sample 2, growth of pore C was significantly slower. One plausible reason for stagnated growth in this case is the lack of adjacent porosity in the immediate vicinity of the pore. It should be noted that there was an observable difference in the necking behavior between Sample 2 and Sample 4. It can be seen in Figure 6 that there were minimal signs of necking for Sample 2 and this is further corroborated by the minimal necking observed for this sample in the supplementary videos provided. In comparison, for Sample 4 in Figure 7(e), after a global axial strain of ε = 0.3363, necking of the gage region was observed in the vicinity of pore C. After necking, the localization of strain between this pore and the adjacent porosity increased, and the pore grew more rapidly. Figure 7(e) shows the orientation of the growth to be on the top side of this pore, which is the direction towards its closest neighboring porosity.

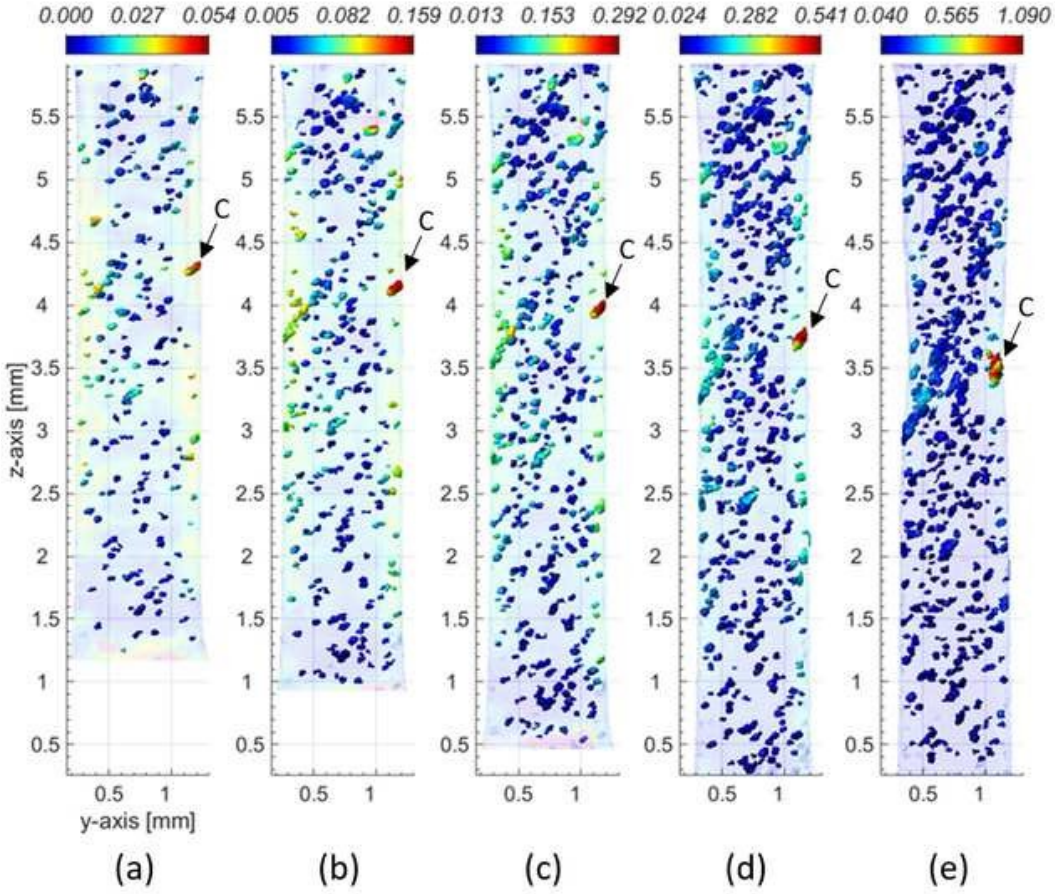

Figure 7. Local strain ε_{zz} mapped to pore surfaces of Sample 4 for global axial strains of (a) $\varepsilon = 0.0187$, (b) $\varepsilon = 0.05252$, (c) $\varepsilon = 0.08772$, (d) $\varepsilon = 0.1190$, and (e) $\varepsilon = 0.1503$.

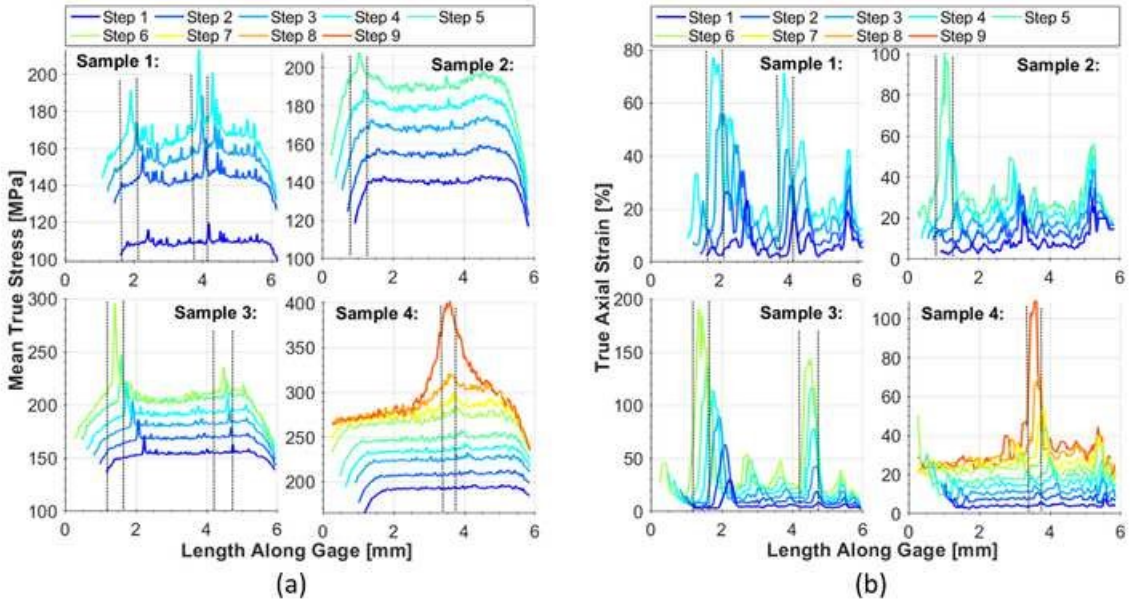

Figure 8. (a) Mean true stress in each cross-section of the deformed volumes as calculated by the measured load over the actual cross-sectional area and (b) Maximum local strain ε_{zz} in each cross-section.

Further investigation into the localization of strain in the material volume of each specimen was conducted by examining the distribution of stress and strain along the gage length of each sample. Figure 8(a) shows the mean stress for a given cross section of each sample at specific locations along the gage length of the sample. Stress was calculated as the measured load over the real cross-sectional area orthogonal to the loading direction, where the cross-sectional area was defined as that attributable to non-pore (e.g., solid) areas. From the figure, each sample exhibited localizations of stress along the gage length that increased with strain. Sample 1 and Sample 2 failed at relatively lower global strain

and exhibited maximum stress values of 200-210 MPa in the cross-section. Sample 3 failed with a maximum cross-section stress approaching 300 MPa. In contrast to these samples, Sample 4 reached stress approaching 400 MPa. Premature failure of Samples 1-3 can be explained by localizations in strain which occurred at earlier stages of the deformation, as is shown in Figure 8(b). In Figure 8(b), regions corresponding to high local stress conditions also corresponded to regions of high localized strains, this establishing the criticality of pore defects in those regions. It should be noted that this estimation of stress cannot account for the natural stress concentrations around the defects, as such, the actual local stress could be higher.

2.5 Discussion

2.5.1 DVC Measurement Accuracy

The measurement accuracy of the present study's DVC technique, with the parameters described above, was validated using artificial deformations of the reference scan texture fields. Rigid body deformations of -11, -22, and -33 voxels along the z-axis were applied first. The range of these displacements approximated the range of displacements seen in actual experiments. Single precision floating point numbers were used for all parts of the analyses. It was found that the errors for all three of these voxel increment displacements was 0 with standard deviations of 0. The measurement accuracy

of intervoxel displacements and strains was tested by applying uniform tensile strains of 1%, 2%, and 4% along the z-axis of the reference texture field. These strains approximate the global strains seen in the experiments. Since there was no displacement in the x and y directions, it is to be expected that their errors were on the order of 10^{-4} voxels (~10^{-4} μm). The average displacement error along the z-axis varied between 0.0579 voxels (~0.4 μm), 0.1742 voxels (~1.4 μm), and 0.6697 voxels (~5.358 μm) for each case of tensile strain, respectively. Average standard deviations were 0.0412 voxels (~0.33 μm), 0.0663 voxels (~0.53 μm), and 0.2249 voxels (~1.8 μm), respectively. The average strain error along the z-direction was 0.0018, 0.0023, and 0.0012, with standard deviations of 0.0010, 0.0013, and 0.012, respectively. All other average strain errors and standard deviations were on the order of at least 10^{-4}. These errors are slightly higher than those reported in Ref. [36]. It is presumed that this is due to lower contrast of the 316L SS texture field than the texture field employed in Ref. [36], but may also be due to the nature of real versus simulated patterns for correlation.

2.5.2 Strain Localization

The intrinsic porosity caused localizations in stress as is evident in Figure 9 which shows the maximum local strain measured by DVC as a function of the corresponding global strain measured for each sample. From the figure, most of the samples immediately exhibited greater local strains than their global counterpart, indicating that strain was highly

localized in certain regions and low in other regions. These localized strains were approximately 5-10 times greater than that of the respective global strain value. As an outlier to this behavior, the local strains of Sample 4 were initially in line with the samples global strain. However, as the test continued this eventually isotropic behavior vanished and the local strain exceeded the global by a factor of approximately 3 at the point of failure. These measurements are important for the selection of modeling parameters in terms of bridging the gap between macro- and micro-scale observations as shown by the work in Ref. [83].

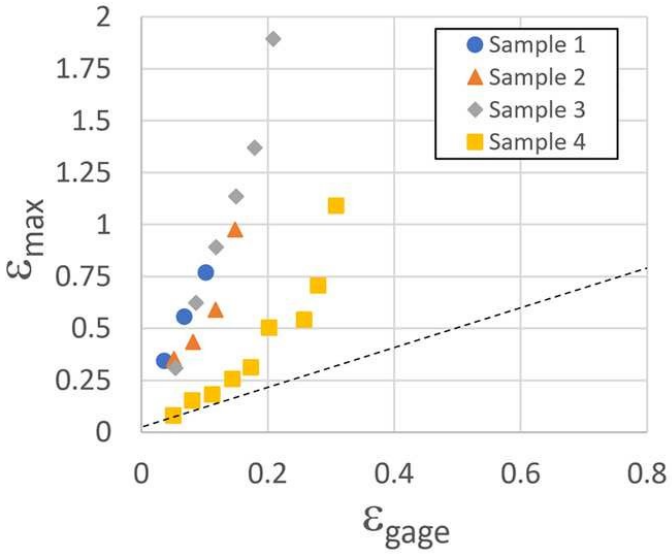

Figure 9. Maximum local strain ε_{zz} measured from DVC compared with the global axial strain.

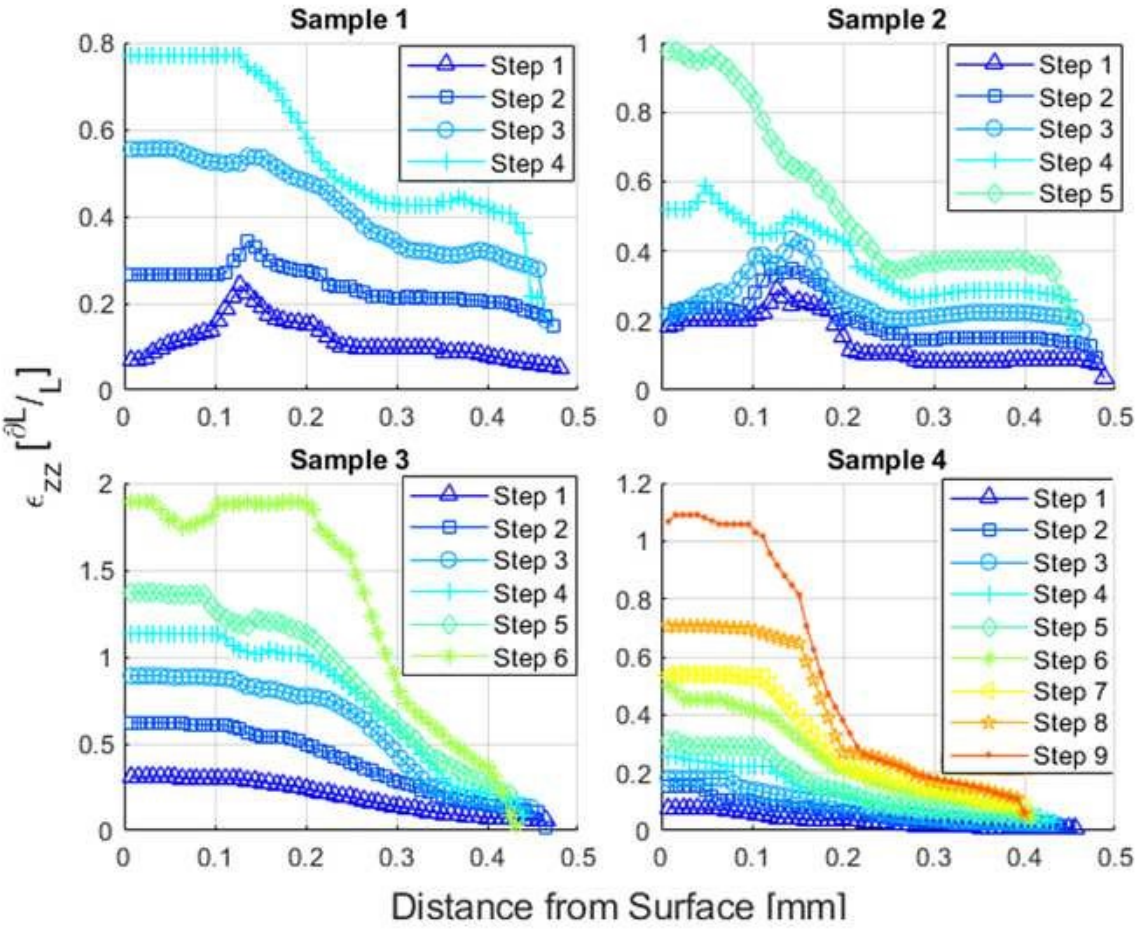

Figure 10. Maximum local strain ε_{zz} versus distance from free surface of each sample.

Figure 10 shows the maximum local strain for each loading step as a function of distance from the surface of each sample. From the figure, higher strains were observed near the edges of each sample, and this increased at higher applied loads. Also evident in Figure 10 is the fact that, at higher applied loads, increased levels of strain were observed

to spread inward to the center of each sample. The presence of high strain near the specimen center is an indication that the porosity grew inward. The growth of these defects acts to reduce the load carrying capacity of the tensile samples due to the reduction of the local cross-sectional area. Reduction in area causes increased local stress and, consequently, also increases the rate of pore growth. As is observed in Figure 6, growth and coalescence of subsurface pores to the free surface was attributed as the cause of failure for Sample 2. Similar behavior was also observed in Sample 1, shown in Figure 11, where subsurface pore D exhibited growth to the free surface under load. The effects of these surface pores are critical as porosity at the surface is less stable than internal porosity, in a similar manner to surface cracks having a greater stress concentration shape factor than internal cracks [84].

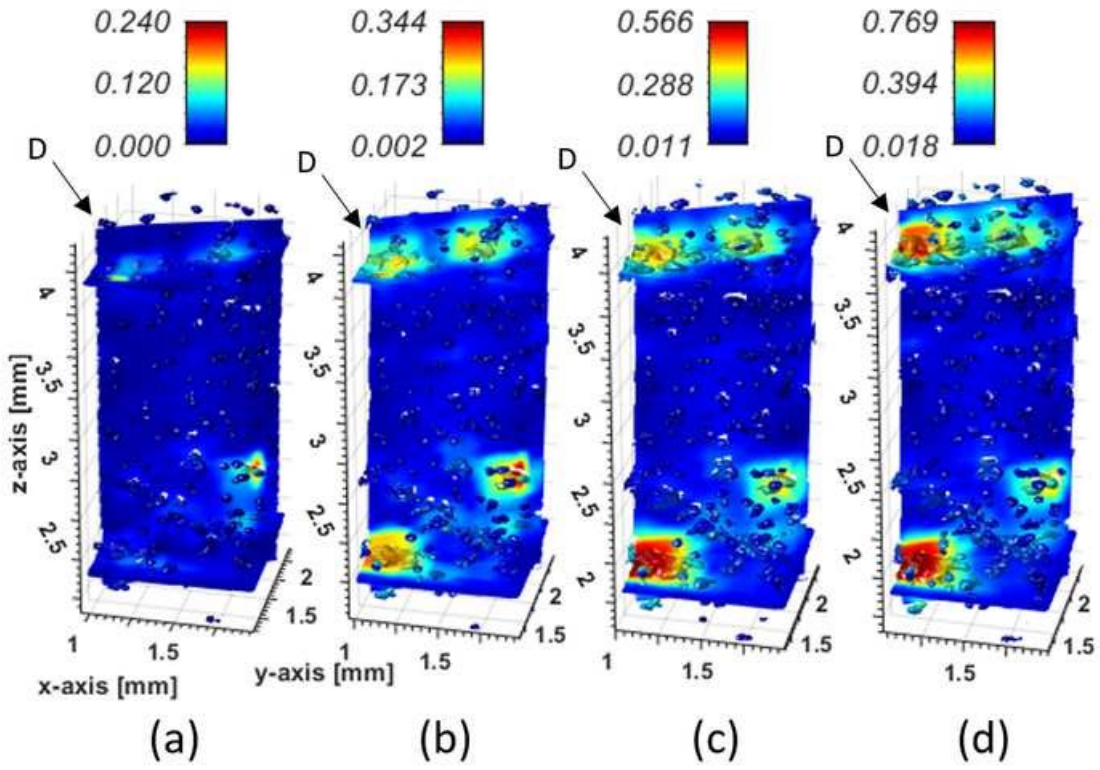

Figure 11. Porosity mapped with the ε_{zz} of Sample 1 for global axial strains of (a) ε = 0.0056, (b) ε = 0.0373, (c) ε = 0.0697 and (d) ε = 0.1037.

2.5.3 Morphological Evolution of Defects

The relative growth and coalescence of subsurface pores can be understood in terms of local material softening due to inter-void necking. In bulk metals with low initial porosity [82], voids generally grow with increasing stress and, at some threshold density of porosity, exhibit interactions with other voids/pores that eventually lead to overall fracture. Figure 6 shows the evolution of the deformation during tensile loading for Sample

2. In this case, a surface pore located at the top of the sample initially exhibited relatively high strain localization. As loading increased, subsurface porosity toward the bottom of the sample at z = 1 mm eventually bridged to the free surface and caused the overall failure of the sample. The high inter-void strain in this region was responsible for the sharpening of initially blunt surfaces of neighboring porosity, as shown in Ref. [85]. These factors accelerated the rate of pore growth. A similar observation can be made during the tensile loading of Sample 1 shown in Figure 11. In this case, the material had two regions of initial strain localization at z = 2.5 mm and z = 4.0 mm. Both of these regions had pores that grew and coalesced to become surface porosity. Even though the grouping of porosity at z = 2.5 mm had the higher strain and larger surface pore, failure ultimately occurred at z = 4.0 mm. It should be noted from Figure 8 that the pores located at z = 4.0 mm in Figure 11 were associated with higher local stress levels.

The relative stability of surface pores under mechanical load despite high strain localization in these regions, as was seen for pore B in Figure 6, was also observed in the case of Sample 4 shown in Figure 7. Stagnation of pore growth can be understood in terms of effects of adjacent porosity. It has been observed in Ref. [82] that plastic flow localization between voids and non-uniform rate of deformation are functions of neighborhood influence. In the present work, pores increased in size steadily, but with minimal growth into the sample, likely due to the relatively lower amounts of porosity immediately adjacent to these pores. For Sample 4 in Figure 7, relative isolation of the

large surface pore from the effects of inter-void strain until later stages of deformation limited tendency for the initial pore to grow. Although, the propagation of the surface pore was stunted in this case, it does appear that other porosity in this region exhibited growth at a higher rate, this indicating that the large surface pore may have caused elevated local strains in the region for other porosity.

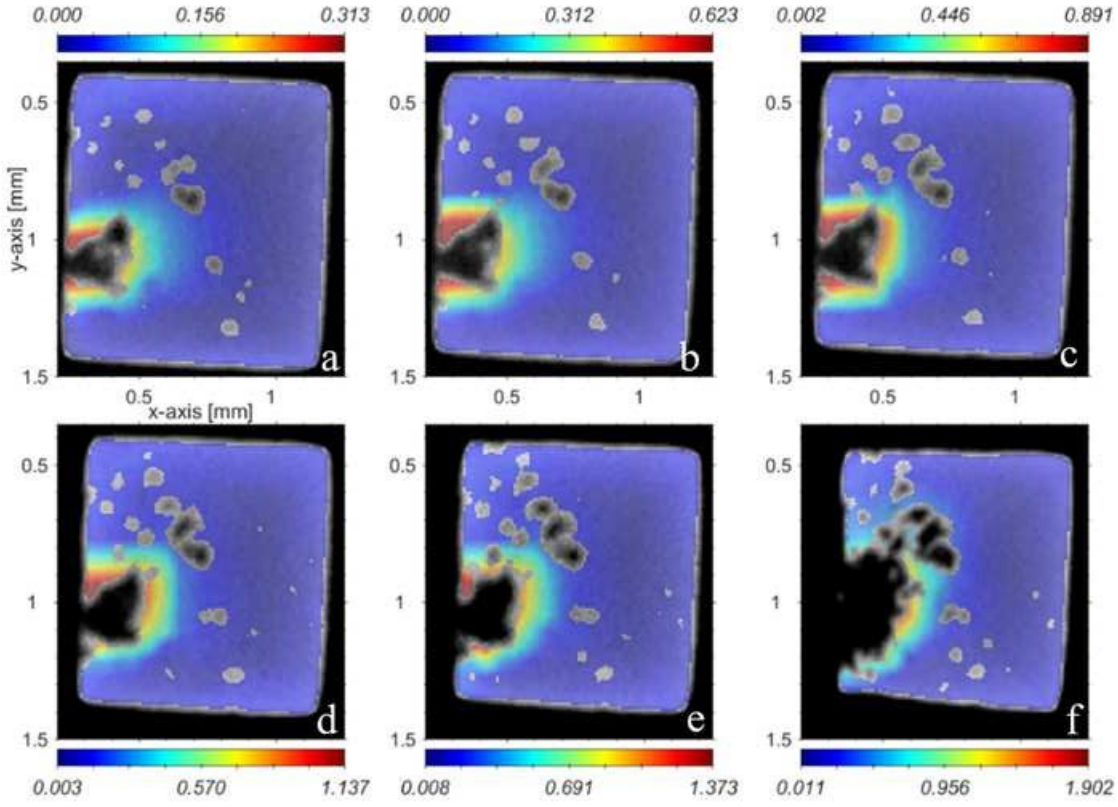

Figure 12. Progression of failure for Sample 3 mapped with ε_{zz} for global axial strains of (a) $\varepsilon = 0.0546$, (b) $\varepsilon = 0.0877$, (c) $\varepsilon = 0.1197$, (d) $\varepsilon = 0.1521$, (e) $\varepsilon = 0.1822$ and (f) $\varepsilon = 0.2114$.

Evolution of pre-existing surface porosity during failure was also observed in the case of Sample 3, where continuous growth of a surface pore was the cause of overall failure of the sample. Figure 12 shows cross-sections of Sample 3 overlaid with the strain distribution at the location of overall sample failure. The mapping shows how local strain concentrated around surface porosity and bridged toward neighboring defects. Despite roughly equally distributed strain levels across the pore boundary, pore growth was observed to be primarily towards the neighboring defects across the image frames. This indicates that the blunting and sharpening of local pore growth behavior controlled the defect evolution. The growth of this surface porosity is also directly observable in Figure 13, which tracks the evolution of the defect field for Sample 3, with the pore evolution in Figure 13 highlighted in red at an initial position of z = 1.75 mm. The evolution of pore size is quantitatively shown in Figure 14. Also observed in this figure is the fact that Sample 4 showed markedly different behavior compared to the other samples in that its pores were relatively stable in size, this attributed to lack of surrounding porosity.

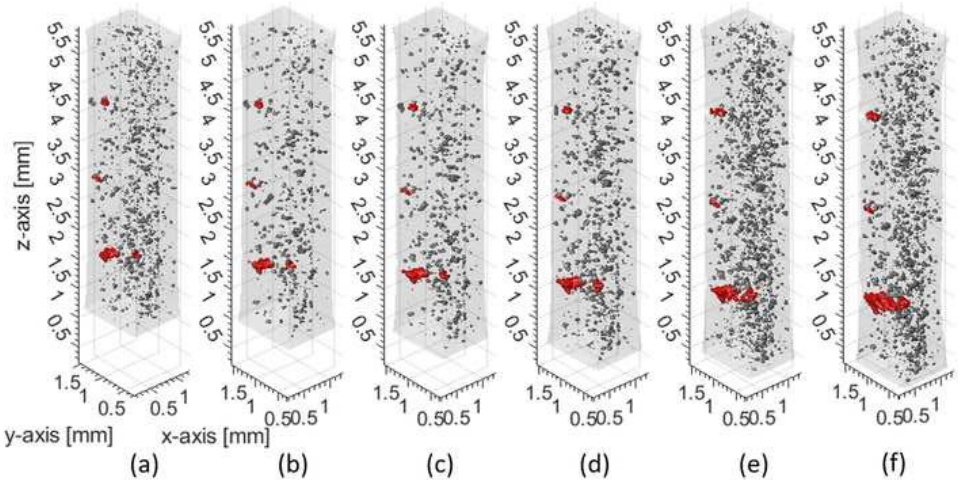

Figure 13. Tracking the progression of critical porosity in Sample 3 for global axial strains of (a) ε = 0.0546, (b) ε = 0.0877, (c) ε = 0.1197, (d) ε = 0.1521, (e) ε = 0.1822 and (f) ε = 0.2114. Evolving pore morphology for select defects is highlighted across frames for clarity.

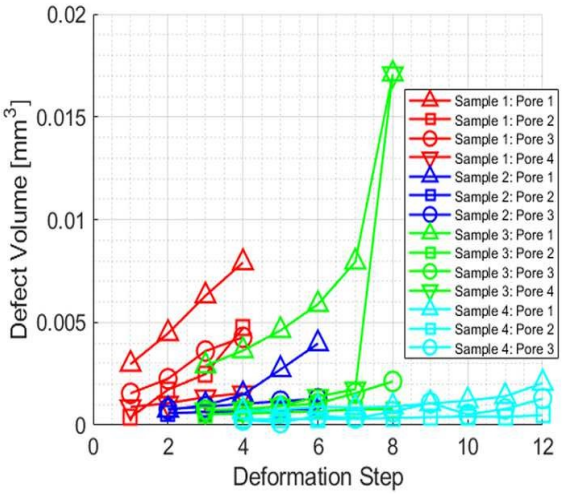

Figure 14. Growth of defects in the failure region(s) of each sample vs deformation step.

Failure of the additively manufactured components in the present study can be understood in terms of ductile failure in bulk metals. In such cases, ductile failure is thought to occur from the onset of void nucleation, with negligible damage in the majority of the specimen until an effective strain is reached, beyond which the mode of strain proceeds in a uniaxial fashion [86]. From that point on, the material between the nucleated voids open (elastic unloading top and bottom) and, as a result, coalescence occurs [82]. In contrast, for initially porous solids, as in the case of the present additively manufactured components, there will be significant damage, in this case void growth, throughout the loading process, and localization of the plastic flow to the internal void (pore) ligaments will occur in a more frequent and dispersed fashion. Such observations are important to modeling efforts and can help with the definition of elastoplastic parameters in simulations [87]. This is due to the existence of significant stress concentrations adjacent to the porous defects already present in the material, as is clear from the above results. Hosokawa et al. [88] showed that this effect can been seen in the acceleration of void growth along the direction of notches being significantly faster. Moreover, it was found that void growth rate and subsequently the onset of void coalescence had a strong positive correlation to the initial pore volume fraction.

2.5.4 Generalization and Limitations of the Technique

In-situ experiments have allowed this research to examine the deformation of the AM samples, and through DVC this deformation has been quantified. However, the measurement of this deformation has only been possible due to the density of defects in the microstructure of these components. In truth, DVC subset windows were set to be large enough to capture this defect texture-field, which results in a virtual strain gauge at a scale or resolution greater than the length scale of the defects. This came at the expense of being able to measure truly local strains around the pores. In the present work, subset centers were place only 7 voxels apart while the full width of each subset was 35 voxels. This high degree of overlap allowed for a multiple measurement points to be located within the length scale of the defects. While this does not remedy the magnitude of the measured strain it does allow for an understanding of its distribution. In reality, measuring deformation with respect to the location on or around the average internal pore is not feasible at this time due to the lack of variation in the gray-scale texture-field in the solid metal matrix. It is feasible that future advances in x-ray phase contrast imaging (XPCI) may remedy this lack of texture, by providing additional information about the local refraction shift or scatter. However, following the same logic, it can be seen that there is no method for measuring true local strain as the scale of locality can always be further reduced.

The lack of precipitates in 316L does not leave this analysis too dissimilar from steels that have precipitates. While the dislocation propagation is the primary damage in traditional 316L deformation it was shown that the dominant mechanism here is intervoid necking. Even the nucleation of voids at the precipitates in other steels and ductile metals would not pose a problem, as in this work it was shown that voids emerge as they grow to a resolvable size for the resolution of the XCT scan without major changes in the intervoid necking observed. Effectively as long as the lack-of-fusion defects are significantly larger than those nucleating or emerging, this style of analysis is valid even at steps where the microporosity cannot be resolved. However, the lack of sufficient pore/defect density, and therefore texture-field, results in weaker correlation. Even ductile metals with less initial porosity prove difficult to measure. This can be observed in the weaker measurements of strain for Sample 4, see Figure 7 and supplementary cross-sections in Appendix A. In fact, the strain measured orthogonal to the loading direction was similarly limited. While the subset windows were large enough to observe the strain in the loading direction, deformation orthogonal to this direction also required similarly large chunks of the texture-field to observe. Thus, the problem arises from the high aspect ratio of the samples. In short portions of the interrogation window in the directions orthogonal to loading would more often than not rest outside the gage region. This in effect reduces the width of the window in these dimensions, resulting in measurements more susceptible to noise. As such, the metric of damage was effectively limited to axial strain. Even with the smoothing behavior

of the polynomial least-squares fitting of strain fields from the displacement fields, the orthogonal displacement fields, especially near the edge of the gage, were subject to significant noise error. This prevented the quantification of ductile damage with more preferable strain metrics such as equivalent strain. It is highly likely that other strains including shear strains were contributing to the failure of these components, however for the reasons stated they could not be accurately measured.

It should also be mentioned, that while this method worked well for the AM 316L SS used herein, there are other AM materials even metals that would not result yield well to this technique. Specifically, more brittle AM metals like AlMgSi would deform far less before rupture. Further, any AM ceramics would not be feasible to measure this way. e damage in terms of the more preferred equivalent strain. There is also the limitation of the XCT resolution to consider. Since, AM porosity does not scale with component size, larger components would be difficult to scan at sufficient resolutions to resolve the small porosity within. Further, since ductile failure is a scale dependent process this technique may become less needed or poorly suited with increasing part size and due to the scope of this work the tipping point of this transition has not been identified.

CHAPTER 3. IMPACT OF INTERNAL DEFECTS ON STRAIN LOCALIZATION

3.1 Introduction

The raw data generated by an XCT system takes the form of a three-dimensional integer array that represent how intense the gray-scale field is at a point in space. Each voxel of this grid has a representative size and is standardly isotropic in measurement, such that a single number can be used to describe its width, length, and height. Reconstructed volumes must be segmented to differentiate between what is background and material. Once the component volume has been accurately segmented, defect detection can be carried out entirely on the digital twin of the physical component; however, it has been shown that identification of porosity and defects by simple thresholding can yield great variation depending on the threshold [89, 90]. By far the most common type of image segmentation is that of global thresholding; a good review of global thresholding techniques was performed by Sezgin and Sankur in 2004 [91]. While ISO50 segmentation is the most commonly applied, advanced methods such as applying a deformable surface (active contour or snake algorithm) can be applied as necessary to improve the segmentation results [92]. Locally adaptive techniques tend to give better and more robust

segmentation accuracy but are more complicated to implement and require significantly greater computation. Other local techniques include fuzzy c-means, kriging, supervised Bayesian segmentation, and a number of active contour algorithms [93]. Growth in the field of machine learning algorithms has seen some application of AI to defect detection in both 2D images and in 3D volumes for AM [94]. Visualization of XCT data sets can be broken down into 2D and 3D representations. Image stacks can be used to provide a single cross-sectional view of the reconstructed gray-scale field. Generate surfaces from the segmentation of the image into specific classes that are useful to visualize in 3D, such as porosity or complex geometry.

3.2 Methodology

3.2.1 Segmentation

Segmentation of the solid, pore, and background regions of each scan of each sample was necessary for both the DVC performed in herein and the feature extraction of the present work. For uniform segmentation analysis the grayscale range of each scan was normalized between 0 and 1. Segmentation was performed using the *Trainable WEKA Segmentation 3D* plugin [95] for ImageJ-FIJI. This plugin, based on the Waikato Environment for Knowledge Analysis (WEKA), allows for the classification of voxels in a 3D data set using machine learning. Built-in drawing tools and a simple guided user

interface allow the user to directly mark the training volume with examples of the correct class labels. The plugin creates feature volumes for each feature selected to complement and expand the grayscale training data provided. Features include Gaussian Blur, Difference of Gaussians, Hessian, Laplacian, Derivatives, Structure, Edges, Minimum, Mean, Median, Maximum, and Variance. Edges, Minimum, and Maximum features were not used in the present study as they were found to skew the analysis between the pore and background classes. Gaussian Blurring, Difference of Gaussians, Mean, and Median feature volumes were used to reduce the influence of noise and improve the segmentation of pores occurring at or near the surface of the gage region [96]. The Hessian feature volumes allowed for the discrimination between thin and bulbous regions reducing the false positive identification of pores [95]. The Laplacian and Structure features allowed for the identification of subtle porous regions by highlighting the textural differences between regions [97]. Sigma, σ, defines the radius of the kernel used in the computation of all features. Separate feature volumes are generated for each variation of σ which for this work were 1, 2, 4, and 8 voxels. This resulted in a total of 83 volumes, including the original grayscale volume, used in each segmentation task. More information about these features can be found in Ref. [95]. For the present study the default classifier algorithm, a parallel random forest algorithm called FastRandomForest consisting of 200 decision trees and 2 random features per node, was used. Decision trees are a structure of conditional statements, beginning with data input at a single node and branching out to additional nodes

with further branching until leaf nodes are reached. Each node operates as a conditional test on the incoming data to divide the data into 'branches' where additional conditions can be applied. The 'leaf' nodes at the end of the tree each represent a class label, numerical or categorical. A random forest is an expansion of this concept where multiple trees of unique structure each predict a target value for the input data. The output is the class selected by the majority of the trees [98]. The application herein utilizes the calculated features at each voxel or point in space to predict its appropriate classification.

To create unbiased results the classifier needed to perform the same on the reference scans of all 4 samples. Since the plugin did not allow for updating the training of an imported classifier, another approach was defined that would train the classifier on all the reference volumes simultaneously. This was achieved by vertically stacking the reference volumes off all 4 samples into a large combined volume. Fortunately, feature volumes are created only in the first round of training and exist unchanged for all additional training iterations. At the end of each training run the model's predictions were examined to locate errors in the segmentation. Errors were corrected by applying additional manual demarcation of the labels in the troubled regions, followed by another iteration of training with the complete labeled training data set. This process was repeated until the segmentation results appeared to perfectly match the distinguishable classes in the gage regions. Large pores that were connected to the surface of the gage regions proved

especially difficult to train the model to distinguish from the background class, and thus required a manual demarcation of every instance across all stacked reconstructions. Examples of each sample's segmentation can be seen below in Figure 15. Additional examples of the classified volumes can be found in Appendix A.3, these results are shown for the deformation history of the components to exhibit the growth of the pores and the elongation of the components.

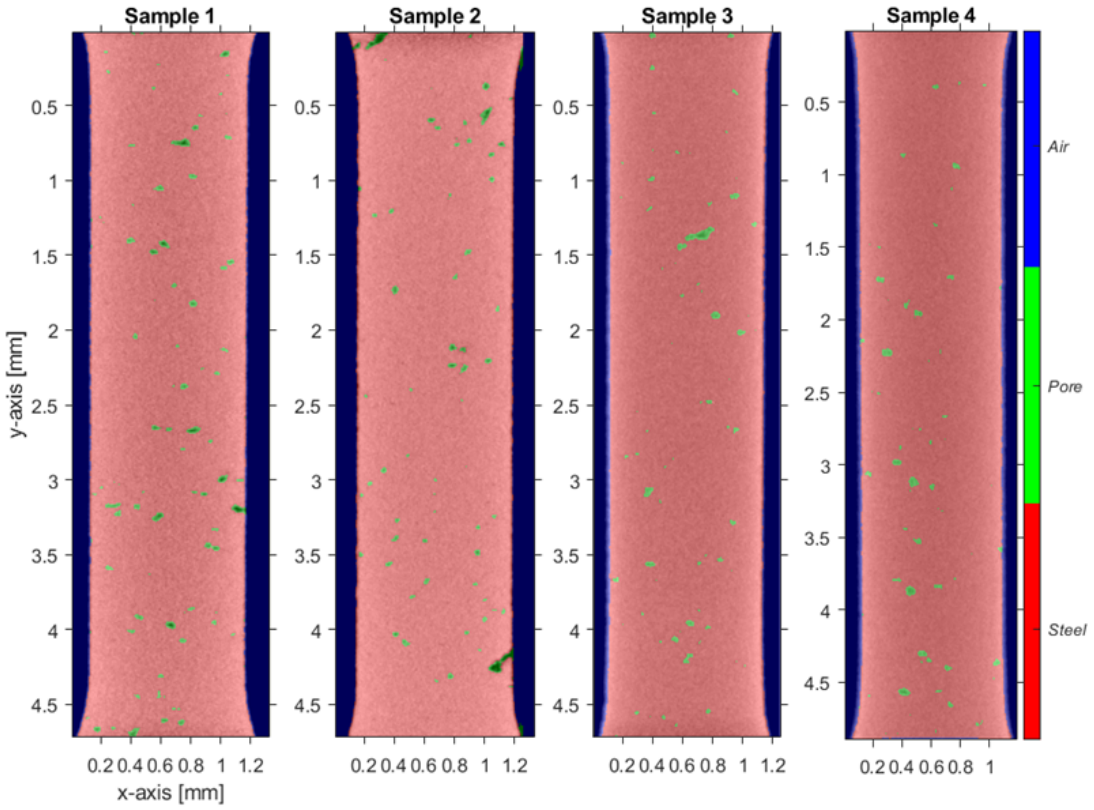

Figure 15. Segmentation results for cross-sections of all 4 samples. a) Sample 1, b) Sample 2, c) Sample 3, d) Sample 4.

The resulting classified volume contained the solid, pore, and background classes of each sample's reference scan. The data was loaded into Matlab and the unique classified volume of each sample was separated from the super volume and saved separately. Features of the pores and body of each gage region were then calculated and stored in a separate structure for each sample. For each sample the porosity label was broken up into unique pores by examining the 26-point connectivity of all voxels labeled pore, where each group of connected voxels identifies a unique pore.

3.2.2 Pore Features

It has been shown that properties of defects like volume and shape play an important role in the behavior of the material regions around them [99]. In the present work, defect volume, diameter, gap, sphericity, compactness, and tortuosity were quantified. Descriptions of the microstructure outside of the defect morphology such as distance from the outer surface and from the defect surfaces to interior points, as well as true wall thickness, and cross-section area orthogonal to the loading direction are also useful.

3.2.2.1 Volume

Pore volume was calculated from the count of pore voxels in each group multiplied by the voxel width cubed.

3.2.2.2 Circumscribed Sphere

Several metrics of defect morphology compared against the ideal shape of a sphere. While some comparisons use a sphere of equivalent volume to the volume of the defect measured, the work herein has opted to use a circumscribed sphere as it maintains important spatial representation of its encapsulated defect. A circumscribed sphere is defined for each pore by first finding the two points on the pore's surface with the greatest distance between them. For a given pore of N surface points, the distance between each surface point of this pore and all other surface points of this pore is calculated. In the present work this was done by constructing an NxN array for each location component (x, y, z) where each column represents the location-component of a single surface point repeated N times. The component distances are found by subtracting each of the 3 arrays by the transpose of itself. The Euclidian distance from these components is then calculated. Retaining only the upper triangle allows for a unique maximal distance to be found where the two indices of the maximal distance in the upper triangle point to the two points that are furthest apart. These two surface points then become two points on the surface of the circumscribed sphere while the midpoint between them represents the center of this sphere. A circumscribed sphere for a large pore in sample 1 is shown below in Figure 16.

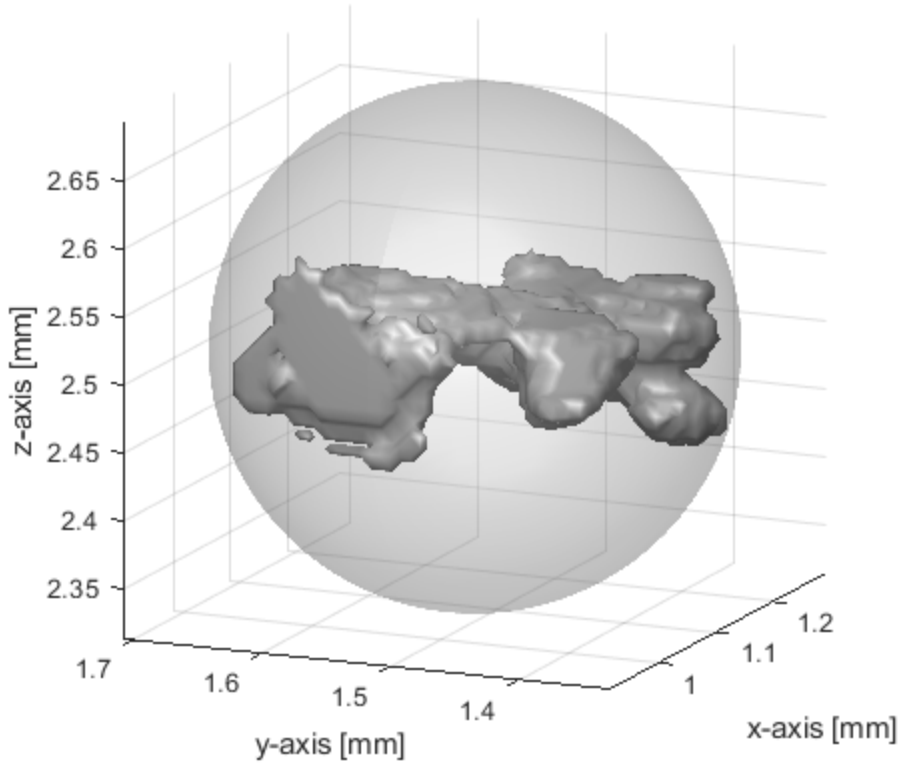

Figure 16. Visualization of a circumscribed sphere encapsulating a large pore in sample 1.

3.2.2.3 Diameter

The diameter of the circumscribed sphere is the diameter of the defect.

3.2.2.4 Gap

For the purposes of this work, the gap between pores is defined as the distance between the surfaces of the circumscribed sphere of each pore. As such, gap can take on a

negative value when circumscribed spheres overlap. Gap was calculated as the distance between sphere centers minus the radius of each respective sphere. Gap is often negative for large pores. For data completeness, the gap between a given pore and all other pores, both in terms of vector and magnitude, was actually stored; however, only the magnitude of the minimum gap of each pore was used in remainder of this work.

3.2.2.5 Sphericity

In this work, the sphericity of a given pore was calculated as the ratio of the defect's surface area divided by the surface area of its circumscribed sphere. To calculate defect surface area a tessellated isosurface of the defect is first generated. The area of this surface was calculated as one half the summation of the squared root of the cross product of each triangular face's tangent vectors. These vectors are taken from 2 of the 3 edges of each triangular face. Surface area of the defect with n tessellated faces was calculated by Equation (8):

$$A_{defect} = \frac{1}{2}\sum_{i=1}^{n}\sqrt{\left(\underline{a}_i \times \underline{b}_i\right)} \tag{8}$$

where a and b are vectors (not normalized) of two sides of each triangular face (iso-surface) of the defect geometry. The surface area of the sphere was then calculated:

$$A_{sphere} = 4\pi\left(\frac{D}{2}\right)^2 \tag{9}$$

3.2.2.6 Compactness

In the present study, pore compactness is defined as the ratio of pore volume over the volume its circumscribed sphere. Pore volume was simply calculated as the number of voxels multiplied by the cube of the voxel size. Sphere volume was of course:

$$V_{sphere} = \frac{4}{3}\pi\left(\frac{D}{2}\right)^3 \tag{10}$$

3.2.2.7 Tortuosity

Pore tortuosity was defined in this work as the ratio of the pore sphericity over its compactness. While both other features are calculated the ratio between the two provides an additional description of the defect.

3.2.3 Component/Gage Features

3.2.3.1 Cross-Sectional Area – show at least one vertical visualization

The cross-section area of each xy-slice of the gage body is defined as the number of voxels in that slice labeled solid multiplied by the voxel width squared. This cross-

section area defines the load carrying area of the given slice. Figure 17 shows an example of mapping this cross-section area in a vertical slice of sample 2 just before failure.

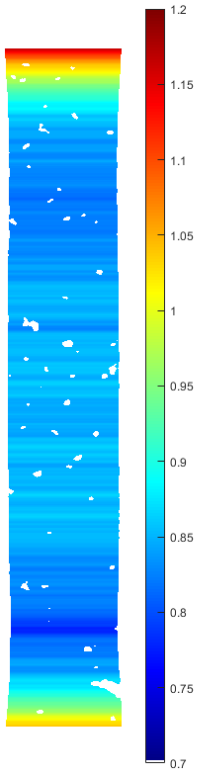

Figure 17. Visualization of the change in cross-sectional area along a vertical slice of sample 2.

3.2.3.2 Distance from External Surface

Distance from the external surface was calculated using a Euclidian distance transform from on a binary volume. The volume was masked to separate the interior and

exterior of the component. The algorithm was implemented via a built-in Matlab function, *bwdist*, and based on the work in Ref. [100].

3.2.3.3 Distance from Internal Surfaces

Similarly, distance from internal surfaces was calculated using a mask that separates the defects from all other voxel classes.

3.2.3.4 Wall Thickness

Wall thickness provides a physical description of how thin the material system is at all points. With all else held constant the likelihood of a voxel experiencing greater strain is inversely proportional to its wall thickness. As such wall thickness becomes an important descriptor of the likelihood for strain localization in an area. Wall thickness in the present analysis was calculated with a modified shrinking spheres algorithm as presented [101]. The algorithm uses a concept of the minimum-inscribed sphere (MIS) between any two walls in space.

The algorithm initializes at each surface point by casting a ray internal to the wall and normal to the surface. The surface voxel this ray intersects with was defined as the opposite side of the initial sphere and defines the wall thickness normal to that point. Next all surface voxels within the given sphere are collected. Spheres between every enclosed

surface voxel and the origin surface voxel are generated simultaneously such that each new sphere has its center on the line between the origin surface voxel and the ray pierced surface voxel. This process can be visualized below in Figure 18. The MIS was then defined to be the sphere with the minimum distance between its center and the origin surface voxel. The wall thickness was then defined as the magnitude for the vector between the two points this MIS intersects. The original algorithm as stated in Ref. [101] called for an iterative process of refining the points of intersection of the MIS and the surface polygons it touches. The modification used herein, opted for surface voxels rather than surface polygons. Treating each voxel as a discreet point of space about its center removes the need to iteratively refine the model along the polygonal surfaces. Instead the model converges in a single step to the MIS. An example of the wall thickness for an ideal geometry is shown below in Figure 19.

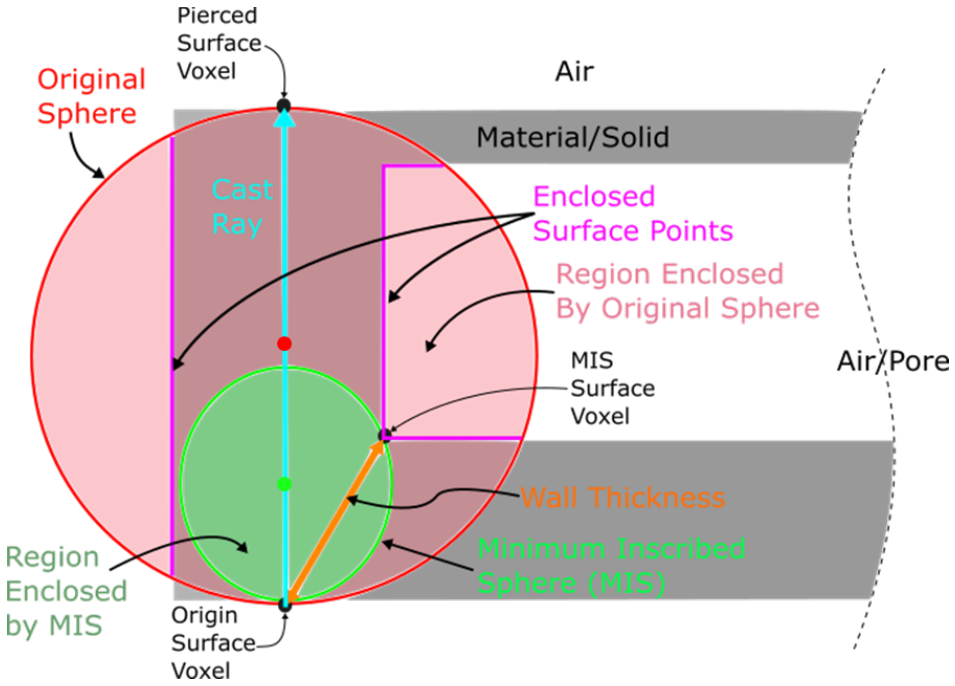

Figure 18. Illustration of the shrinking sphere algorithm.

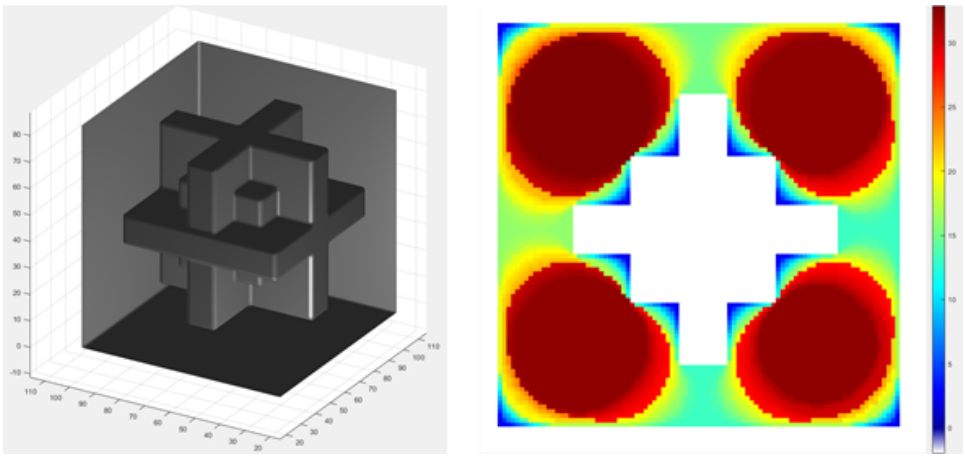

Figure 19. Test geometry for modified shrinking sphere algorithm in a voxelized framework.

The wall thickness model herein was calculated in parallel over the set of all surface voxels such that each worker of the CPU(s) calculates the wall thickness for a unique surface voxel, while other workers simultaneously calculate the wall thickness from their surface voxel. The algorithm used herein was designed to collect the indices of all voxels inside of each final MIS and stores them for a non-parallel computed consolidation process. The final wall thickness feature volume is made up of the maximum wall thickness value for each voxel of space. The indices stored for each MIS will overlap, but the largest wall thickness at each voxel is the final value of the wall thickness at that voxel. An example of the wall thickness calculated for sample 1 is shown in Figure 20 below. For data completeness, the information about the final vector between the origin voxel and the MIS surface point was retained in the data structure, although it was not used in the present work.

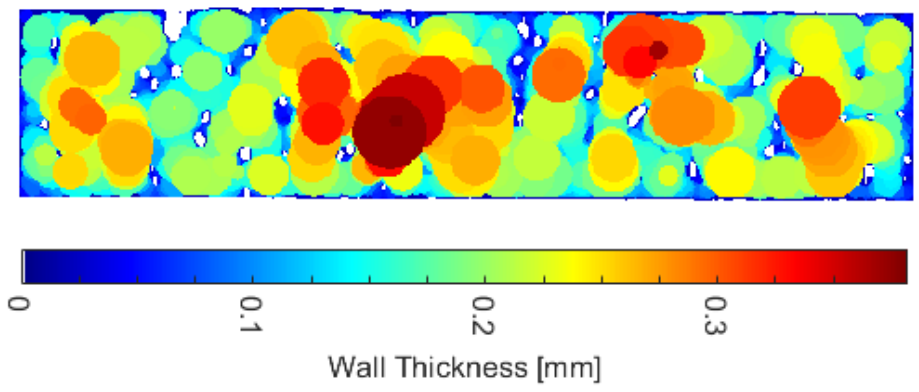

Figure 20. Example of how wall thickness is distributed in sample 1.

3.2.4 Feature Expansion

Spatially locating features to their associated object enriches the local data of the digital twin model and provides a means for the direct comparison of spatial features with local mechanical behavior. As such, defect descriptors were used to naturally classify the region of their associated defects, and component descriptors provided information about the material between defects. Accounting for the influence of defects on the region around them requires some approximation of regional influence of each defect. In the present work, balanced defect regions were generated using a watershed segmentation based on the distance from each defect surface. The features within each watershed region were expanded to fill the regions.

3.2.5 Down Sampling

Between the 4 samples there was a total of 24 deformation steps measured. This results in over 2.34 billion voxels of data for the resulting strain fields alone. Further, including the number of features computed for each data point sets this number over 2.1 trillion. Therefore, it was necessary to crop the feature volumes down to a manageable size. For continuity the cropping used in the calculation of the strain via DVC was also chosen to reduce the size of the feature volumes. Further, due to the uncertainty in the exact

distribution and potency of specific features from specific defects, this approximation will require some degree of blind smoothing of features between defect regions.

A down sampling kernel was defined at the center of each DVC subset, such that minimum, mean, and maximum feature values were extracted for each subset. The span of the kernel window provided an effective blurring of region boundaries. In addition, the down sampling process made it easy to define the local defect density within each subset. This presents another component body feature, but unlike other feature volumes it has a singular value for each subset and not a minimum, mean, and maximum. Finally, the nonlocal field generated with the model proposed herein was also sampled and used to enrich the feature data sets as a means of quantifying spatial interaction. Down sampling provided additional advantages in that using the points of measurement from the DVC analysis removes the need to consider the effects of upscaling interpolation. Ultimately each measurement of every sample provided between 16,640 and 17,920 observations.

3.2.6 Correlation Coefficient

While some studies have considered correlating defect metrics to global or bulk mechanical properties, no study has yet attempted to correlate local strain and local defect and component features. In this work, the linear dependence of the local strain field on local features was measured using a correlation coefficient described by the following:

$$\rho(A,B) = \frac{1}{N-1}\sum_{I=1}^{N}\left(\overline{\frac{A-\mu_A}{\sigma_A}}\right)\left(\frac{B-\mu_B}{\sigma_B}\right) \tag{11}$$

where μ and σ are the mean and standard deviations, respectively, and $\rho(A,B)$ is the correlation coefficient between A and B [102].

3.3 Results

3.3.1 Distribution of Features

The distribution of a few select features are shown in the histograms shown below in Figure 21. It is clear that the high amount of porosity in sample 1 was larger than the data in samples 2-4, but it can still be seen that the defect volume, gap, sphericity, and compactness trends of all 4 samples are similar. This implies that in general there was no fundamental morphological differences between the porosity in any of the 4 samples.

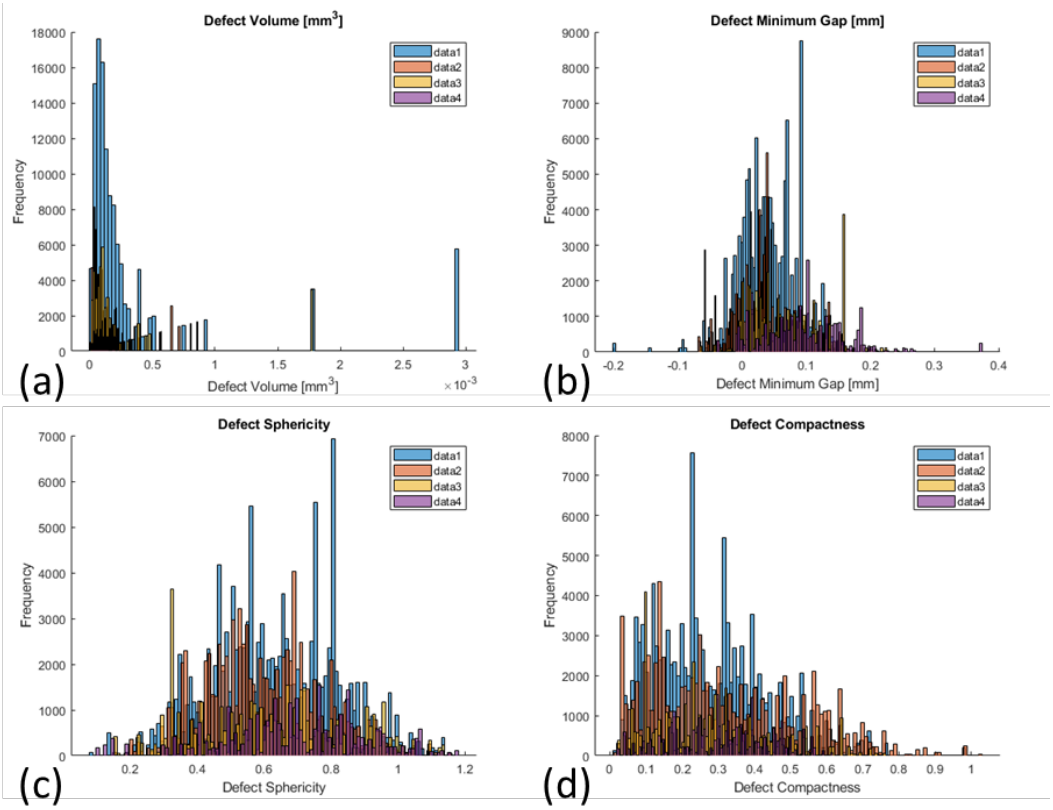

Figure 21. Histograms of defect features. (a) Defect Volume, (b) Defect Minimum Gap, (c) Defect Sphericity, (d) Defect Compactness.

3.3.2 Correlations

Table 2 below shows the values of the correlation coefficients calculated between the feature volumes and the strain volume in the down sampled resolution of each sample. The integrated nonlocal mapping provided the best feature in terms of correlation, however this predictor showed poor correlation with the strain measured for sample 4. Conversely,

the distance from the external surface, inverted, showed provided the best correlation with sample 4, but poor correlation with the other three samples, particularly sample 1. The full set of feature correlations with the measured strain can be found in the supplementary material in Appendix B.1.

3.4 Discussion

As shown by Table 2, the localization fields generated by the proposed nonlocal analysis provide the best correlation with the measured strain fields. Pore volume showed the next best correlation especially for sample 3 but had limited correlations with both sample 2 and 4. Inverted distance measurements showed fairly consistent positive correlation albeit anemic, in almost all cases. However, the inverted distance from the outer surface proved to be negatively correlated with the strain in sample 1. Conversely, it provided a fairly strong correlation with the early strain development in sample 4. Pore volume fraction only showed a weak correlation with strain for all 4 samples. This is in contrast with the conventional practice of using volume fraction to approximate where strain will localize for numerical modeling, however this may be due to the relatively small window in which pore volume fraction was taken such that it would be consistent with the sampling of other features. In fact, most features were found to be very weakly correlated (<10%) with the measured strain. While these results are true for the axial strain measured from the uniaxial tension tests, defects have profound impacts on other material properties

and behaviors as well. Porosity plays a role in the reducing the elastic modulus of materials, and in general increasing their shock tolerance. Defects especially porosity, in components that will be subject to high cycling are particularly deleterious. These defects will serve as the sites of microcrack initiation and the propagation thereof. Additional defect characteristics could be applied to quantify metrics of defect directionality, from principal component axes, or curvature from the local defect surfaces, but these characteristics were not quantified herein.

Table 2. Correlation Coefficients of a select few features.

Sample	Global Strain	Minimum Inverse External Distance	Mean Inverse External Distance	Maximum Inverse External Distance	Minimum Pore Volume	Mean Pore Volume	Maximum Pore Volume	Minimum Inverse Cross-Section Area	Mean Inverse Cross-Section Area	Maximum Inverse Cross-Section Area	Minimum Inverse Wall Thickness	Mean Inverse Wall Thickness	Maximum Inverse Wall Thickness	Minimum Nonlocal Mapping	Mean Nonlocal Mapping	Maximum Nonlocal Mapping	Pore Volume Fraction
1	0.56	-0.155	-0.157	-0.157	0.305	0.391	0.381	0.292	0.240	0.125	0.258	0.266	0.207	0.461	0.462	0.452	0.189
	3.74	-0.145	-0.146	-0.145	0.437	0.607	0.599	0.457	0.385	0.234	0.324	0.359	0.284	0.623	0.618	0.603	0.269
	6.97	-0.164	-0.164	-0.162	0.451	0.650	0.657	0.492	0.419	0.265	0.318	0.356	0.280	0.648	0.639	0.623	0.259
	10.37	-0.157	-0.156	-0.153	0.445	0.637	0.640	0.530	0.453	0.290	0.314	0.356	0.278	0.652	0.643	0.628	0.254
2	1.87	0.027	0.017	0.021	0.256	0.326	0.319	0.150	0.151	0.148	0.244	0.243	0.173	0.353	0.364	0.359	0.147
	5.25	0.050	0.040	0.039	0.268	0.352	0.335	0.264	0.279	0.289	0.329	0.358	0.293	0.439	0.451	0.445	0.181
	8.30	0.072	0.062	0.060	0.283	0.376	0.354	0.319	0.335	0.345	0.356	0.392	0.327	0.481	0.490	0.482	0.188
	11.90	0.069	0.058	0.055	0.298	0.401	0.376	0.342	0.353	0.358	0.371	0.409	0.343	0.520	0.527	0.517	0.195
	15.03	0.092	0.082	0.080	0.321	0.432	0.406	0.338	0.341	0.338	0.375	0.419	0.359	0.549	0.548	0.535	0.197
3	5.46	0.191	0.187	0.183	0.652	0.738	0.708	0.236	0.143	0.037	0.216	0.246	0.194	0.698	0.649	0.604	0.192
	8.77	0.205	0.201	0.198	0.666	0.748	0.714	0.262	0.162	0.045	0.237	0.273	0.216	0.713	0.666	0.622	0.226
	11.97	0.226	0.222	0.219	0.656	0.739	0.706	0.280	0.176	0.051	0.256	0.301	0.242	0.714	0.670	0.627	0.236
	15.22	0.226	0.221	0.218	0.633	0.718	0.689	0.302	0.192	0.057	0.269	0.320	0.259	0.709	0.669	0.628	0.243
	18.22	0.227	0.222	0.219	0.614	0.702	0.675	0.307	0.194	0.055	0.276	0.334	0.273	0.698	0.662	0.625	0.243
	21.14	0.168	0.162	0.160	0.587	0.691	0.687	0.317	0.185	0.020	0.282	0.346	0.289	0.747	0.715	0.679	0.245
4	7.50	0.272	0.481	0.529	0.240	0.238	0.215	0.041	0.041	0.039	0.191	0.193	0.180	0.126	0.101	0.071	0.036
	10.70	0.262	0.488	0.543	0.251	0.244	0.213	0.063	0.063	0.060	0.190	0.192	0.180	0.138	0.115	0.087	0.044
	13.91	0.243	0.481	0.542	0.257	0.257	0.230	0.098	0.098	0.095	0.177	0.186	0.182	0.158	0.136	0.108	0.049
	16.84	0.224	0.463	0.526	0.275	0.276	0.249	0.125	0.124	0.119	0.161	0.180	0.183	0.190	0.168	0.139	0.058
	19.79	0.203	0.443	0.507	0.292	0.297	0.273	0.163	0.160	0.154	0.145	0.167	0.177	0.208	0.187	0.159	0.063
	25.50	0.284	0.493	0.543	0.302	0.310	0.285	0.020	0.013	0.003	0.224	0.252	0.241	0.222	0.195	0.161	0.069
	27.71	0.252	0.460	0.512	0.325	0.339	0.316	0.073	0.065	0.054	0.199	0.234	0.229	0.249	0.223	0.190	0.075
	30.59	0.207	0.407	0.460	0.343	0.366	0.348	0.139	0.130	0.118	0.163	0.205	0.210	0.265	0.242	0.211	0.079
	33.63	0.162	0.338	0.386	0.398	0.436	0.426	0.176	0.167	0.153	0.130	0.173	0.186	0.293	0.267	0.235	0.085

CHAPTER 4. MODELING STRAIN LOCALIZATION

4.1 Introduction

4.1.1 Mechanics of Ductile Failure

In a fully dense material, ductile failure is thought to occur from the onset of void nucleation, with little damage in the majority of the specimen until an effective strain is reached beyond which the mode of strain proceeds in a uniaxial fashion. This means that E_{11} & E_{22} cease to exist and are replaced with elastic unloading above and below the pore [86]. Instead, from that point on rapid void growth occurs. As the material between the nucleated voids begins to open up (elastic unloading top and bottom), void coalescence occurs [82].

4.1.2 Mechanics of Strain Localization

The mechanical behavior of porous solids differs from that of monolithic polycrystalline materials such as traditional wrought metals. It is a commonly held belief that ‘inferior’ or ‘variable’ mechanical properties that are likely to result from AM builds [103]. Part of the reason for this notion is that it is common for AM components to have higher yield strengths and ultimate tensile strengths than wrought specimens of the same material, they also have lower ductility and typically a strong anisotropy associated with their build direction [35, 46]. The reduced ductility of AM specimens is concerning,

because it is indicative of the underlying damage phenomena that AM components experience. Several works have attempted to model the mechanical behavior of AM components using both standard finite element methods [104, 105] and stochastic finite analyses [106, 107, 108, 109]. A major gap in the extant work on this subject is that these methods do not specifically account for locality and characteristics of internal defects of the AM materials. Instead, they homogenize these effects to allow for application at a macroscale. There have been a few works that attempt to combine the stochastic FEM analysis with localization of damage, but due to the infeasibility of modeling the real defects, damage is accrued with an internal state variable [110]. The more significant gap is that these methods effectively predict the average response of AM materials and components and do not provide information about how a given individual component may locally fail.

4.1.3 Modelling Efforts

In 1976, J.R. Rice developed a theoretical framework for the localization of strain before component failure [111]. Following efforts, including those by Asaro and Rice, looked at the role of strain hardening, positive or negative, in localization. They found that localization can occur with positive strain hardening given some deviations from the Schmid rule [112]. It has been found that actual computational modeling with finite elements suffers from mesh sensitivity as the element(s) refine towards zero length as noted

by Pijaudier-Cabot and Bažant [113]. Tvergaard used micro mechanical calculations to show that microporosity can introduce highly localized strain banding between larger voids [114]. Horstemeyer and Revelli investigated the effects of microporosity on the growth of voids and the localization of strain [115]. Considere's Seminole work in 1985 showed that materials will inherently become plastically unstable in tension and even small defects can promote localization [116]. Further work by Tvergaard investigated the role of void coalescence in ductile failure [117]. Similar studies have been done in Ref. [118]. A review of continuum modelling efforts can be found in Ref. [119].

A.L. Gurson developed the foundations of void growth models (VGM) with his work on voids and yield criteria 1977 [120]. Modelling efforts for void growth and strain localization are primarily focused around finite element (FE) analyses with major simplifications of the pore geometry and distributions to axisymmetric formulations such as cylinders, spheroids, and ellipsoids with more or less regular distributions [50, 52, 120, 121, 122]. Gologanu et al. developed a Gurson-like constitutive model with the added ability to account for more complex void shapes with ellipsoidal prolate and oblate voids [123, 124]. Their efforts have shown that both initial porosity distribution and pore shape play a significant role in the localization of plastic flow before coalescence and failure in low and high stress triaxialities, respectively [53, 125]. Macroscopic modeling of both void growth and localization commonly makes use of pore (void) volume fraction as a metric

of material behavior. More recent works have focus on incorporating these models into complete constitutive frameworks with notable works by Benzerga [53, 82, 126], and Morin [127, 128]. More recently, Muhammad et al. developed a machine learning model for the prediction of local strain for additively manufactured parts in Ref. [129], however, this model was only developed for small local strains up to 10% and only applied in 2D.

4.2 Methodology

4.2.1 Non-local Influence Model

Past studies have shown that strain localization is influenced by microstructural parameters beyond void volume fraction; microporosity and geometric parameters such as void shape, size, and distribution also exert significant influence. Unit cell models have been used to show that it is common for strain to band between large voids and lead to local necking behavior in intervoid-ligaments. However, the computational expense of these FE models is prohibitive in scaling to full 3D components with preexisting porosity. Further, these methods rely on simplifications of the shape and distribution of these voids, but LOF porosity in AM is often of tortuous shape and arbitrarily distributed. Consequently, these micromechanics-based models are not yet capable of tackling localization of strain in highly porous material systems. As such, an alternative method for predicting the localization of strain in porous media is the focus of this study.

The method proposed herein attempts to account for the influence of preexisting porosity on strain localization by treating each instance of porosity as a nonlocal source of influence. The approach is to extend a nonlocal material model of the integral type to include the directionality of each nonlocal source. Shown below in Equation (12) is the basic formulation of the integral nonlocal approach for a point, ω, and nonlocal contributions from sources, φ.

$$\overline{f}(\omega) = \int_{\Omega} a(\omega, \varphi) f(\varphi) d\varphi \tag{12}$$

The nonlocal field at the local point, $\overline{f}(\omega)$, is effectively a weighted average of the nonlocal contributions in the domain, Ω [54]. The nonnegative weight function, $a(\omega, \varphi)$, decreases with distance from the source.

The integral nonlocal approach provides a method of modeling the overlap of influence between defects. Given the link between porosity distribution and shape with void growth and strain localization [115], modification of the model to include shape and relative location of the nonlocal sources (defects) was necessary. Vectors between nonlocal sources and a given point are used to describe their relative location. Further, the breakdown of these vectors into their components parallel and orthogonal to the loading direction frames their influence in terms of both the prolate and oblate growth of the voids in the surrounding space, this formulation can be seen in the first and second terms of the

first set of brackets in Equation (14), respectively. Additional weights can be applied for greater malleability. The influence of the nonlocal source's shape was similarly described by expanding the single nonlocal vector prescribed to each source to be a set of nonlocal vectors from the surface points of the source to the given local point. Each set of vectors, hereafter referred to as nonlocal vectors, further accounts for the shape of their source by swapping the componentization orthogonal to the loading direction with one relative to each surface point's surface normal. In this way the crack tip like behavior at the one end of a nonlocal source is projected only in the direction of its potential propagation. At the same time, the side of a void opposite to an intervoid-ligament is effectively non-influential on the ligaments behavior as is expected. As with the traditional nonlocal model, the value at a given point is obtained from the weighted summation of the spatially augmented field and a function of its distance to the given point. Consider the representative volume element (RVE) shown in Figure 22.

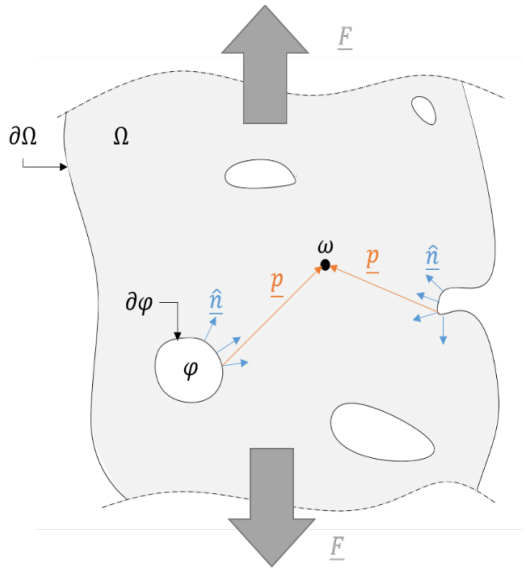

Figure 22. Representative volume element of the vectorized nonlocal field integration.

ω	Local point of interest
φ	A pore as a nonlocal source
$\partial\varphi$	Surface of a nonlocal source pore
$\underline{\hat{n}}_{\partial\varphi}$	Surface normal unit vector of a nonlocal source pore
$\underline{\hat{p}}$	Unit vector between the nonlocal source or its surface and the point ω
Ω	The material domain
$\partial\Omega$	Surface of the material domain as a nonlocal source
$\underline{\hat{n}}_{\partial\Omega}$	Surface normal unit vector of a nonlocal source that is the material domain surface
$\underline{\hat{F}}$	Unit vector of the loading direction

The projection of vector $\underline{\hat{p}}$ against the unit loading direction and also orthogonal to the unit loading direction provides the fields parallel and orthogonal, respectively, to the loading direction. These are sources for nonlocal weighted averaging at each point, ω. The monotonically decreasing weight function, $a(x, \varphi)$, provides the necessary dissipation of field intensity with distance from each source. This function is formulated below in Equation (13):

$$a(\omega, \varphi) = \begin{cases} \left(1 - \left(\frac{r}{R}\right)^m\right)^n & for\ 0 \leq r\ \leq R \\ 0 & for\ r\ \geq R \end{cases} \tag{13}$$

where $r = ||\omega - \xi||$ is the distance between the source and the local point and R is the interaction radius of a given source. In the present work R was determined as a function of the radius of a sphere of equivalent volume with its associated defect. Specifically, the quantity of 5 times this equivalent sphere radius was used. However, it has been suggested that the more rigorous determination of R would be derived from St. Venant's Principle. The powers m and n control the shape of the decreasing function. A value of 1 for both m and n produces a linear decay, $m = 1$ and $n = 2$ produces a quadratic decay, and $m, n = 2$ produces a bell-shaped decay. The full formulation of the localization predicting model is:

$$\overline{f}(\omega) = \int_{\Omega} a(\omega,\varphi)\left[q_1\left(\underline{\hat{p}}\cdot\underline{\hat{Q}}\right)+(1-q_1)\left(\underline{\hat{p}}\cdot\underline{\hat{F}}\right)\right]\left[1-q_2\left(\underline{\hat{Q}}\cdot\underline{\hat{F}}\right)\right]d\varphi$$

$$\underline{\hat{Q}} = \begin{cases} \underline{\hat{n}}_{\partial\varphi}\ (\varphi\ \rightarrow \partial\varphi) \\ vectors \perp \underline{\hat{F}} \end{cases} \tag{14}$$

where q_1, q_2 are weights that allow for additional shaping of the nonlocal contributions. The second bracketed term allows control of the field distribution relative the shape of the pore and the loading direction, such that the field can be pushed to the brim of the shape and allow for an unloading zone above and below each pore. This equation can be further extended to account for the effects of surface roughness by adding the section below:

$$\int_{\Omega} a(\omega,\partial\Omega)\left[q_3\left(\underline{\hat{p}}\cdot\underline{\hat{n}}_{\partial\Omega}\right)+\left(1-q_3\right)\left(\underline{\hat{p}}\cdot\underline{\hat{F}}\right)\right]\left[1-q_4\left(\underline{\hat{n}}_{\partial\Omega}\cdot\underline{\hat{F}}\right)\right]d\partial\Omega \tag{15}$$

4.2.2 Artificial Neural Networks

Both defect characteristics and the non-local field data were down sampled at the DVC analysis measurement points using the subsets from the analysis to obtain the minimum, mean, and maximum of these characteristics and non-local field at each measurement point. Prior to down sampling all data was stored as characteristic volumes of the same size and shape as their associated reconstruction volumes. After down sampling there were a total of 36 descriptive values associated with the center point of each subset

of the DVC analysis. These points were then linearized into a list of observations where each center point defined a unique observation with 36 features. The observation lists across samples and deformation steps were then concatenated into one unified list of observations. This final list was 418,560 x 37, where the 37^{th} feature was the load measured for the given deformation state. The measured axial strain field was similarly linearized into a single column list.

Initially, attempts were made to employ a 3D convolutional neural network (CNN), a form of deep learning, approach to predict strain from 3D arrays of the descriptive data. However, training of these models proved slow, and a more efficient approach was needed. Therefore, efforts were pivoted to developing shallow networks that could predict the strain at each point without inherent spatial coupling of the observations. Shallow network machine learning models in the vein of artificial neural networks (ANNs) were developed using Matlab 2020a [130]. ANNs are made up of hidden-layer(s) each with a given number of nodes or 'neurons' that will independently weight and offset the incoming data. These networks are designed such that each feature is handled as a channel of data. At each neuron the incoming channels of data are separately weighted and offset before being summed and scaled via a transfer function to the following layer. As such the total number of input channels, m, is multiplied by the given number of neurons, n, in the layer for a total of m x n weights and offsets to be tuned for said layer. In following layers, the number of data

channels is defined by the number of neurons of the previous layer. For the present work each hidden layer employed a symmetric hyperbolic tangent as the transfer function. As a continuous function with a high gradient, this function is ideal for general network training. In the present work the models had a single output layer with a single neuron and a pure linear transfer function that simply scaled and summed the incoming data channels to predict the strain for the given observation.

4.3 Results

4.3.1 Non-local Influence Fields

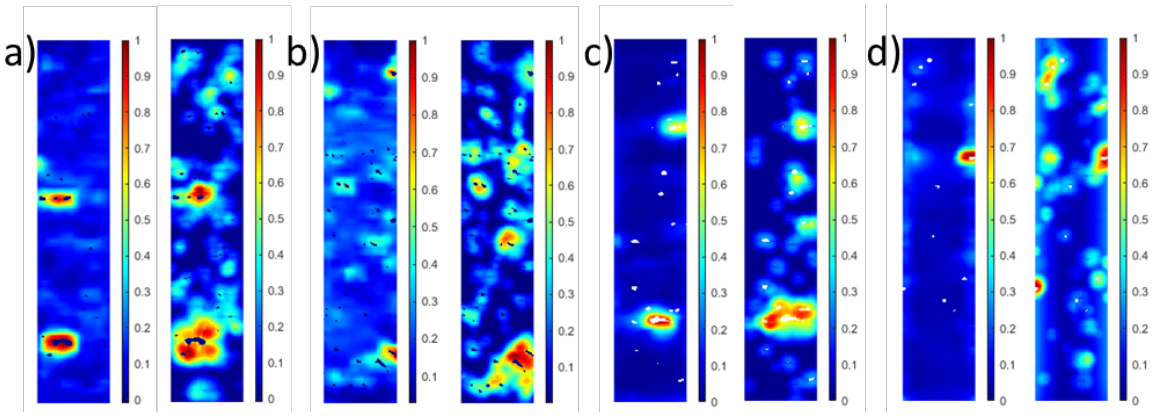

Figure 23. Comparison of the normalized local axial strain measured (left) and the localization predicted by the nonlocal mapping analysis (right). a) Sample 1 @10.37% global strain, b) Sample 2 @15.03% global strain, c) Sample 3 @21.14% global strain, d) Sample 4 @33.63% global strain.

Results of the non-local mapping analysis (right) as compared to the last strain measurement before failure (left) for each sample are shown in Figure 23 above. It should be noted that since the nonlocal influence model does not include terms that relate to the load or deformation progress, there is only one predicted localization field for each sample. Since failure rapidly follows strain localization, this prediction was designed to be most in line with the strain measured just before failure. The local axial strain fields were normalized at each measurement level to redistribute their range between 0 and 1 to represent no localization and high localization, respectively. The results show that the analysis was capable of identifying the areas of major localization, but also provided an overprediction of the localization elsewhere. In particular, Figure 23(d) shows that the model predicted medium-high localization between several intervoid locations and at one surface pore location, however these predictions did not match with the field measured for the sample. The correlation coefficients between the localization mapping and the measured strain are shown in Figure 24. As expected, the correlation improved as each sample approaches failure, mimicking the increase in strain localization within the components. It can be seen that sample 4 proved the worst in terms of predictability with this model.

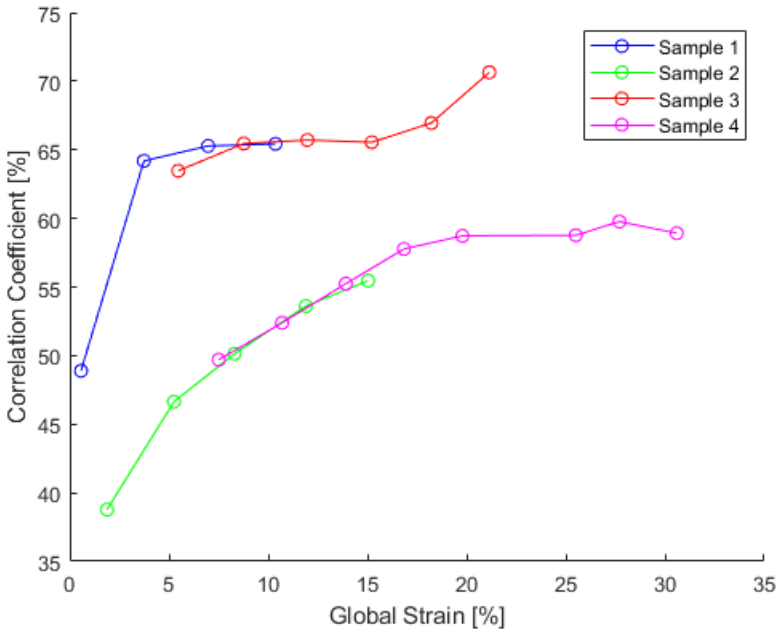

Figure 24.Correlation coefficient of the nonlocal field with strain localization vs global axial strain.

4.3.2 Optimal Network Architecture

With the proposed shallow network, it was still necessary to optimize the network hyperparameters, which are number of hidden layers and the number of neurons per layer. To maintain model simplicity, the number of hidden layers was capped at 4 and the number of neurons was capped at 72, twice the number of sample features fed into the network. Each following layer was restricted to have half the number of neurons as the previous. This kept the total number of network permutations to 10. For each architecture, 10 models

of that architecture were generated. Each model was given a different random set of the training, validation, and test data, but the ratios of each were maintained across all 10. The combined prediction of 10 models in parallel allowed for the total prediction of each configuration to be far more robust to overfitting and variations in the training data.

Table 3 shows the combined predications of the 10 models trained with each network architecture. Values shown are the average of the 10 models generated with the same architecture but a slightly different set of training and validation data. This provided a more robust prediction that is less likely to be overfit to the training data. As expected, the results showed that single hidden layer networks performed poorly, but that increasing the number of neurons in a layer boosted the training performance. This was also seen in the 2, 3, and 4 hidden layer networks. Acceptable mean squared errors (MSE) had a 10^{-4} order of magnitude as this resulted in regression accuracy of 91+%. Ultimately, a 2 hidden-layer 72 and 36 neuron network architecture, performed the best on the unseen data.

Table 3. Performance of the artificial neural network (ANN) architectures broken down by complexity. Values shown are the average of the 10 models generated with each architecture but a slightly different set of training and validation data.

			Number of Hidden Layers			
			1	2	3	4
Number of Neurons in First Layer	9	MSE	0.00193			
		r	0.80719			
		m	0.61968			
		b	0.03528			
	18	MSE	0.0017	0.00124		
		r	0.83333	0.88146		
		m	0.66063	0.74119		
		b	0.03144	0.02373		
	36	MSE	0.00157	0.00108	0.00104	
		r	0.84621	0.8982	0.90233	
		m	0.68927	0.76798	0.77656	
		b	0.02875	0.02136	0.02073	
	72	MSE	0.00148	0.00077	0.00088	0.0009
		r	0.85618	0.92822	0.91724	0.91608
		m	0.71291	0.83774	0.80687	0.7991
		b	0.02646	0.01486	0.01775	0.01855

As shallow networks of simple architecture, model training time was not significant with the longest training taking only 2.78 hours and the shortest only 22 seconds to reach convergence. Convergence was defined as six iterations of training without improvement in the prediction of strain on the validation data set. Convergence of the optimal architecture models took longer than others. On average it took the optimal architecture 1.4 hours to converge vs. 0.81 for the 3 hidden-layer architecture at 72-36-18 neuron. Model

accuracy normalized by convergence time shows that 2 hidden-layer 18-9 neuron architecture proved the most efficient. If model efficiency is the goal, then this architecture may be a good trade of in terms of accuracy vs. training time.

4.4 Discussion

4.4.1 Quality of the Non-local Influence Predictions

The modified nonlocal field generation proved adept at predicting strain localization with the minimum correlation found being ~38% for the early stages of deformation in sample 2 and a maximum correlation of ~73% just before failure in sample 3. Accuracy of the strain localization prediction improved with increasing strain in each sample. This is to be expected as localization of strain about defects is thought to accelerate as components strain to failure [53]. The cross-sectional comparisons show that the nonlocal integration was adept at predicting regions of high strain localization but suffered from the overestimation of strain in quieter regions. This suggests that either the model needs to have accelerated degeneration with distance or that the DVC analysis is more capable around the hot-spots due to the mechanism of correlating based on high contrast patterns. Further, measured axial strain in these low magnitude areas did trend with the nonlocal model predictions, but the form of the measured field was significantly more disperse and continuous. This suggests that the smoothing effects of the DVC analysis

windows likely underestimated these strains. Additionally, the growth of porosity in these regions and the emergence of previously unseen pores with increasing deformation further supports this assessment. Therefore, the disparity in the localization of strain in non-critical regions is likely due to both the simplified model implementation of the model and the limitations of the DVC analysis in terms of measuring areas of less unique texture and low deformation. Since the rate of field deterioration was tied to the characteristic length of the source, a function of the equivalent sphere radius; bringing associated characteristic lengths more in line will simultaneously coarsen and smooth the field for large and small porosity, respectively. Further, weighting of the model to penalize low volume defect sources and low volume fraction areas of porosity would significantly dampen this spotting. One possible solution would be to associate the characteristic length with some estimate of the region of influence as extracted from the DVC analysis. However, the difficulty of this would lie in estimating these measured regions of influence as some function of local defect characteristic. Moreover, separating the influence of one defect from that of another in regions where intervoiod necking is apparent has no clear solution at this time.

In some samples, the prediction of additional elevated strain localization at porosity adjacent to the site of primary localization was seen. Figure 23(a, b) shows this behavior occurring in samples 1 and 2, respectively. The analysis for sample 1 predicted an elevated localization with porosity to the top left of the lower site of high strain localization, and in

sample 2 similar predictions were made for pores just below the primary strain localization site. These small nodal localizations between the adjacent porosity are not seen in the experimental results. This can be solved by tuning the ratio of strain contribution parallel and orthogonal to the loading direction with q_1 and the accumulation of above and below the defects with q2. In the present work q_2 was set to 0 to enhance the sense that the model was operating blindly or without preconceived notions of what the strain should look like. By setting q_1 to 0.75, as such the vector components along the surface normal direction were set to be 3x stronger than those along the loading direction. This effectively assumes that the influence of defect shape will outweigh that of loading direction. The values of q1 and q2 were chosen to demonstrate how the model performs with only a generalized formulation. Greater values of q_1 and q_2 would reduce the proclivity for the model to predict small localization nodes in adjacent sources above and below the primary localization site.

Additionally, the measured fields showed greater trends of strain localization near the gage surfaces. This can be resolved with the inclusion of the outer surface integral shown in the model formulation. Inclusion of this term is a computationally expensive process that is several orders of magnitude slower than the limited integration from solely internal sources. Instead, an approximation of the contributions of the outer surface can be generated with a linear weighting scheme divided by the distance from the outer surface and added to the integrated solution from the internal sources.

It should be noted that the predictive capacity of the nonlocal model is inherently tied to the quality of the defect identification and demarcation and as such is dependent on the effective voxel size of the reconstruction. At the same time, increasing the resolution of the system will inevitably increase the computational time and load of the analysis. For a uniformly discretized space the computational cost scales at a rate greater than n^3, where n is the ratio change in resolution relative to the previous resolution. Other difficulties arise in the determination of appropriate weights. In recognition, future work is suggested to apply the nonlocal model to nonuniform or even dynamic spatial resolutions and to tie the weight determination to secondary characteristics of the contributing defects. Finally, the model falls short of predicting the actual strain magnitude at a location, and as such can currently only function as a pointer to areas where critical strain can be expected or as a metric of how much strain is expected to localize in a component.

4.4.2 Quality of the Shallow Network Predictions

The performance distribution of the 10 network models generated for each network architecture is summarized in Figure 25. The mean squared error in Figure 25(a) is optimal at the lowest value, thus the least error. Similarly, the offset of the regression fit is optimal at 0 and for each architecture the distribution of the offset for each model can be seen in Figure 25(d). The regression value or each model represents the correlation of the predicted strains with those measured. Figure 25(b) shows the distribution of the regression values,

where a value of 1 indicates a perfect correlation and a value of -1 indicates anti-correlation. As, can be seen, even architectures that performed poorly relative to the optimal architecture found over 75% correlation. This implies that models of only 9 neurons and a single hyperbolic tangent transformation were able to capture over 75% of the variance in the measured results. Figure 25(c) is the slope of the regression line, where a slope of 1 indicates that changes in feature values perfectly map to the changes in the strain. The variation in model architectures is provided by the data series in a nomenclature that describes the number of neurons in each hidden layer separated by underscores, such that 0_0_0_18 and 0_36_18_9 are a single-hidden-layer network with 18 neurons and a 3-hidden-layer network with 36, 18, and 9 neurons in each respective layer, respectively. It can be seen that the most complex architecture consisting of 4 hidden layers with 72, 36, 18, and 9 neurons, respectively, had one model out of the 10 trained that converged at a local minimum instead of the apparent more accurate minima that the remaining 9 converged towards.

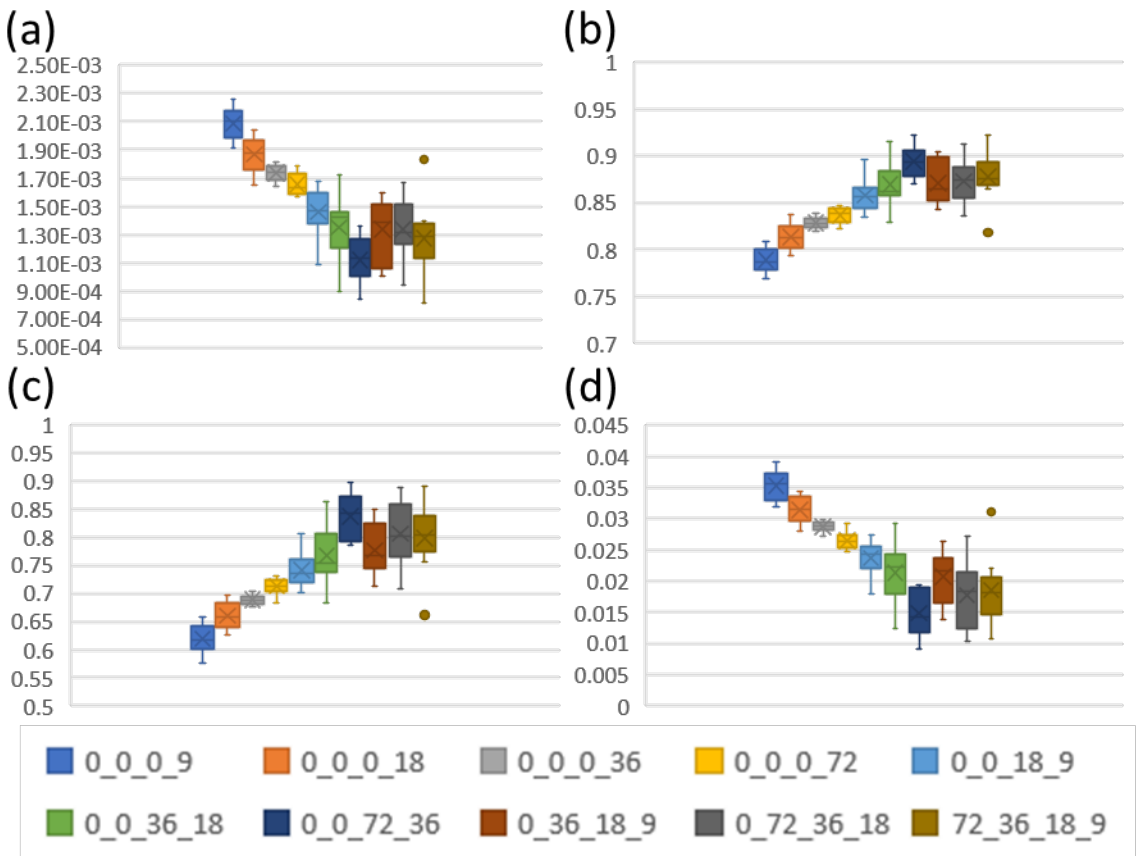

Figure 25. Box and whisker plots of the sub-model performances on the fresh unseen data. (a) MSE, (b) regression value, (c) slope of the regression fit, and (d) offset of the regression fit.

The results of the shallow network modeling revealed that even networks of 9 nodes in a single layer were able to obtain registration values of greater than 80% and fit line slopes of over 60% for fresh data not seen in training, validation, or testing. As such, the model was able to predict the localization and magnitude of strain from the unchanging set of features measured in its undeformed state and a knowledge of its expected load at that

stage of deformation. The optimal shallow network architecture of 2 hidden layers with 72 and 36 neurons, respectively, had a combined mean squared error of $7.7x10^{-4}$. Thus, the implementation in the present work was more accurate per hidden layer and more accurate per number of neurons per layer when compared to Ref. [129]. All 10 component models with this architecture had regression values, $r \geq 90\%$ and linear regression slopes of just under 90% accuracy. Averaging the predictions of all ten sub-models produced a regression value of 92+%, which is greater than any of its sub-model's regression value. This performance boost proves the robustness of the combined prediction approach employed herein. The combined prediction, averaged prediction from the 10 sub-models, produced an MSE of 0.00077, and a slope of the regression fit was 0.8377. This particular architecture outperformed the less and more complex model architectures in all categories when the models were used to predict the results of fresh unseen data. The more complex models only outperformed the optimal model on the training data. These performance metrics are shown in box and whisker charts for the 10 models or each architecture in Appendix A.5 where the results of the training, validation, and individual testing are shown. In addition, the performance on the fresh data set is shown.

It was observed that model accuracy improved with increasing deformation in all samples. Since the localization of strain and subsequent failure of components occurs rapidly before failure, predictions discussed herein will be limited to the frames of strain

captured near failure. The combined prediction of this architecture's models is visualized below in Figure 26. No interpolation was used to plot the data as values are shown at the center point of each DVC subset. The actual vs predicted local strain for sample 1, shown in Figure 26 (a, b), exhibits a visually compelling match between the measured axial strains and those predicted by the model. Similar compelling arguments can be made for samples 2 and 3 in (c, d) and (e, f), respectively. Similar to the nonlocal influence model this model showed poorer performance for sample 4 relative to the other 3. Sample 4 was also the least like the other 4 samples in terms of morphological evolution and initial porosity, so it is possible that its prediction suffered from a lack of additional specimens with similar behavior. The model performed well at capturing even small local fluctuations in strain data as exhibited by (a, b) and (c, d) in Figure 26 below.

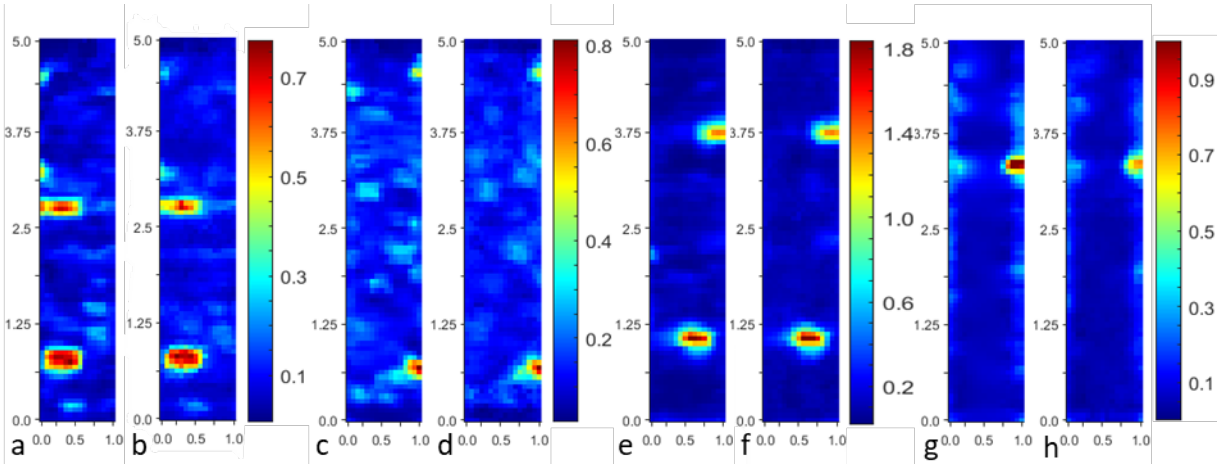

Figure 26. Visual comparison of the actual and predicted strain at the last measurement before failure mapped over the DVC grid points. Measured strain for samples 1, 2, 3, and 4, is shown in a, c, e, g, respectively, and the predicted strain for samples 1, 2, 3, and 4, is in b, d, f, h, respectively.

4.4.3 Synthetic Alterations

Regardless of the model performance on the given data, the introduction of data with different material or geometric systems would result in poor predictive performance. This is a known issue with machine learning techniques that limits their applicability to real world solutions. Moreover, extracting useful information from even simple model architectures is extremely difficult, however there is still use in such models. These models can function as interpolants for the given data sets.

Experiments produce very specific results over the range of the samples tested. Given the time and expense of experiments in this domain, there is a need to effectively

translate data between the experimental realm and the modeling one. Machine learning provides a simple path for this transition. To extend the amount of information obtained from experiments, the present work involved creation of artificial data via synthetic alterations of the experimental data. This artificial data can be used to see the effects of specific changes on the microstructure in terms of the strain predicted for the system. Further, these changes can be used to build a wealth of engineering knowledge about the behavior of AM microstructures and their strain localization. Synthetic alteration of only a small portion of the experimental data will not cause the model to need to extrapolate its results, provided that the changes made fall within the range of data collected for training. For reference the unaltered porosity configurations in the reference state of the sample are given below in Figure 27.

In this section a single pore within each sample's ultimate failure region, and adjacent to the critical porosity, was chosen to be altered. These pores are identified and shown in Figure 28 below, the critical pores are shown in magenta and the pores to be altered are shown in purple. Two views, one perspective and one straight on down the sample gage, are given for each sample, top and bottom, respectively. Alterations included morphologically changing the volume of the pore, moving the pore along a vector defined between itself and the critical pore, and moving the pore along a vector defined between itself and the closest point on the external surface of the component. These relatively small

changes to each data set allow the wealth of predictive power of the model to be probed. Further, the pores to be altered were chosen specifically for their apparent role in the strain localization that lead to failure originating at the critical surface pore of each sample.

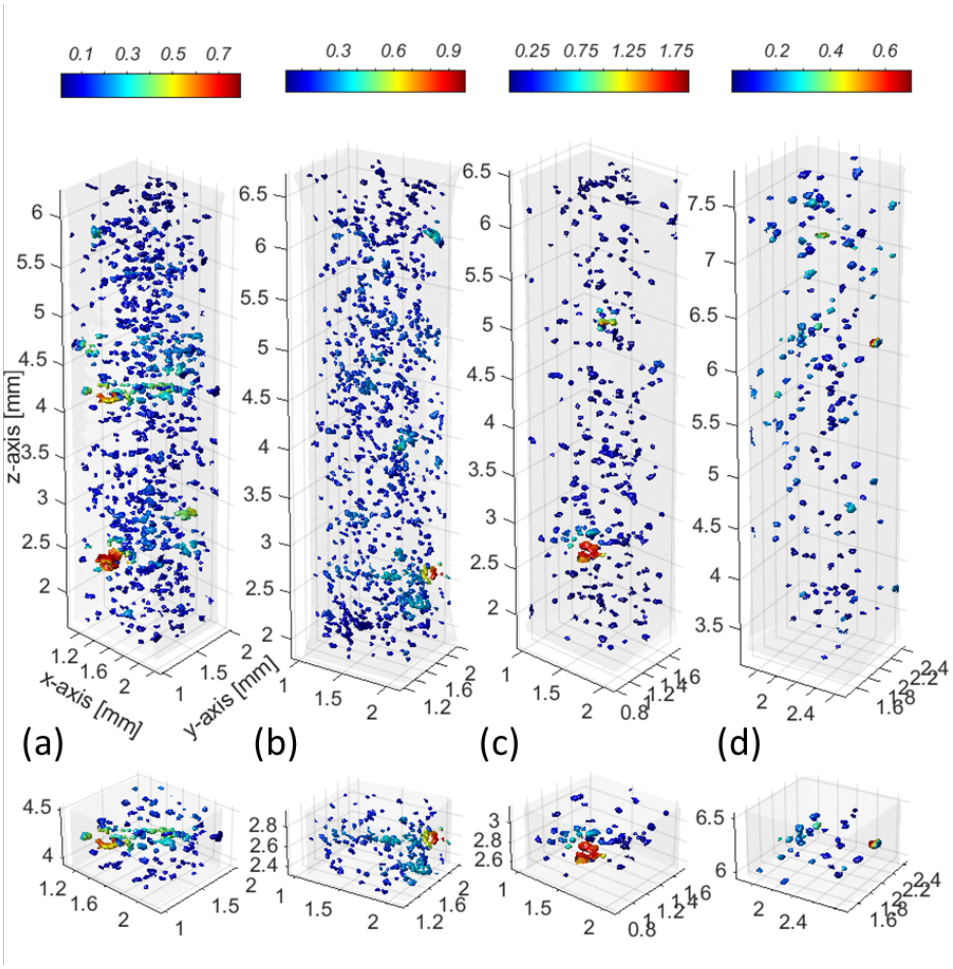

Figure 27. Visualization of the defect fields color mapped to represent the strains at the surface of each defect. Focused views of each sample's failure region porosity are shown below their given sample. a) Sample 1, b) Sample 2, c) Sample 3, d) Sample 4.

Alterations were performed on the chosen pore for the reference configuration of each classified volume. The alterations focused on the pore volume, distance between pores, and distance from the pore to the surface of the component. Each metric was changed independently and incremented to increase twice and decrease twice relative to each independent parameter a summary is provided in Table 4. Since the system of features are inherently linked, changes to the defect volume will change features around this pore.

Table 4. Pore alteration applied to each sample for each sample's given global strain.

	Alterations
Pore Volume	$\Delta r = -2$ vx
	$\Delta r = -1$ vx
	$\Delta r = +1$ vx
	$\Delta r = +2$ vx
Pore Gap	$\Delta d_{crit} = -26$ vx
	$\Delta d_{crit} = -13$ vx
	$\Delta d_{crit} = +13$ vx
	$\Delta d_{crit} = +26$ vx
Surface Distance	$\Delta d_{ext} = -26$ vx
	$\Delta d_{ext} = -13$ vx
	$\Delta d_{ext} = +13$ vx
	$\Delta d_{ext} = +26$ vx

Alterations were applied to the last two measured states of each sample. So, with the total of 4 samples, 2 states per sample, and 12 alterations per state, there are 96 synthetic defect volumes generated. Each generated volume required the features of that volume to be recalculated, for the new defect configuration. This whole process generates over 1.72

million new observations to be fed to the trained model, greatly increasing the amount of data obtained from a single set of experiments.

Pore volume changes made use of morphological erosion and dilation with a spherical structural element with radius equal to 1-2 voxels depending on if it was a minor or major alteration, respectively, see Table 4. The gap between the pores identified in Figure 28 was altered by calculating the vector between the centroids of the altered and critical defect and moving one of the altered along the direction this vector provides. Finally, the movement of the altered defect relative to the exterior surface was carried out by finding the closest surface voxel of the exterior surface to the altered defect's surface and moving this defect along the vector between this point and the defect center. Each alteration would have ripple effects that facilitate the need to recalculate all the defect features and nonlocal integral field. The purpose of these changes in the experimental data is that the unintended consequences are actually witnessed. Fully artificial data allows the user to isolate specific testing questions, but at the expense of ignoring the combined (effects from all the ripple changes and from all the other nonlocal defects) effects of real data changes.

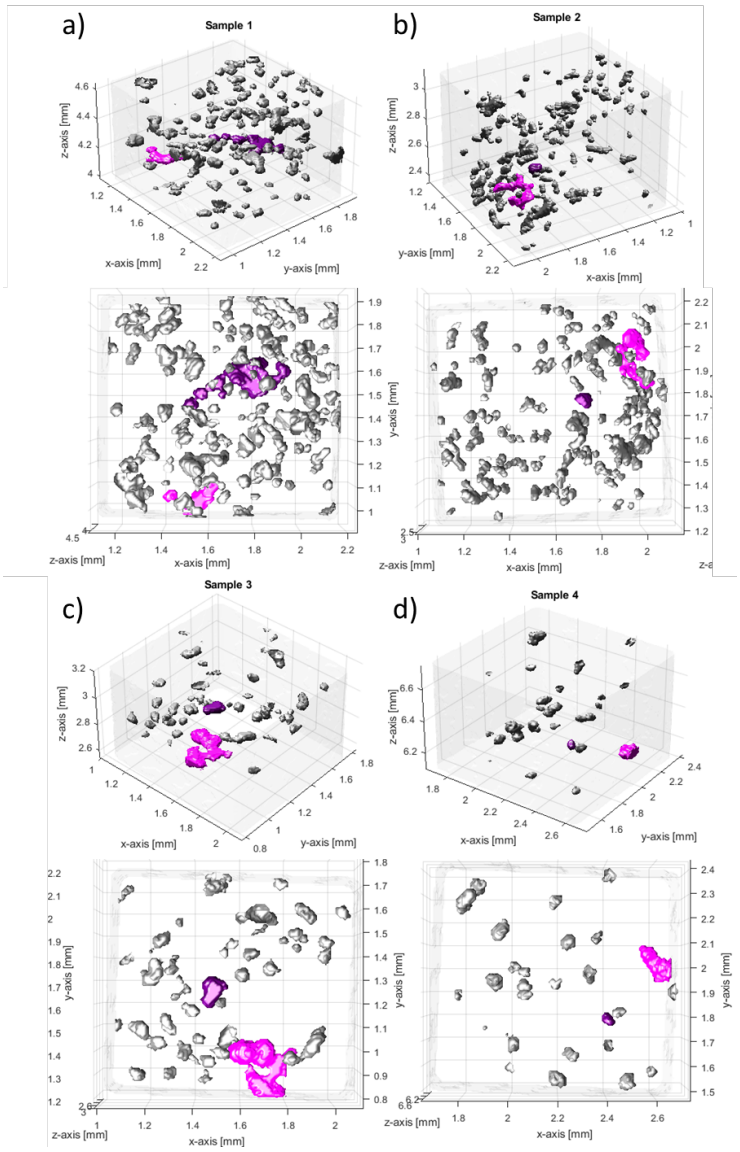

Figure 28. Visualization of the critical pore (magenta) and pore to be altered (purple) for each sample. a) Sample 1 in perspective (top) and straight on (bottom) views, b) Sample 2 in perspective (top) and straight on (bottom) views, c) Sample 3 in perspective (top) and straight on (bottom) views, d) Sample 4 in perspective (top) and straight on (bottom) views.

4.4.3.1 Effect of Pore Volume Changes

Results of the predictions on synthetic data varied from sample to sample. Samples 1 and 3 were more sensitive to the synthetic alterations than samples 2 and 4. This is in part due to the nature of the failure in samples 1 and 3. Both samples 1 and 3 had oblate surface pore growth that lead to rapid coalescence with horizontally adjacent porosity and failure. While samples 2 and 4 also failed due to surface pore growth, their mode of failure was dissimilar. The failure in sample 2 was due to growth of a surface pore diagonally and then the rapid propagation along shear bands towards other adjacent large pores as described in Tvergaard as a void-sheet mechanism in Ref. [117] and or more specifically as Barsoum and Faleskog described it as intervoid shear in Ref. [131]. The conditions for shear localization are given in Ref. [132]. On the other hand, sample 4 exhibited primarily prolate growth of a surface pore. Necking occurred in this same region likely due to the softening effects of the porosity and the reduced cross-section. As noted by Noell et al. there are often multiple competing and collaborating failure mechanisms in ductile fracture, especially with preexisting voids [133]. In general, alterations in samples 1 and 3 resulted in changes in strain that were an order of magnitude greater than the same alterations caused in samples 2 and 4. Another consideration is the original size of the pore being altered. In samples 1 and 3 the pore being altered is of significant size even before dilation; whereas, in samples 2 and 4 the pore is of a size that is only slightly above average

for that sample. Nonetheless all pores were chosen for their proximity and observed interaction with the critical porosity in their sample.

Increasing pore volume via dilation with a spherical element of a 2-voxel radius ($\Delta r = +2$ vx) resulted in local strain rises around the altered pore of samples 1 and 3 of up to 0.87 and 0.6, respectively. Samples 2 and 4 exhibited rises of only 0.12 and 0.17, respectively. On average the rise in strain around the altered pore was approximately 0.5, 0.08, 0.3, and 0.07 for samples 1 through 4, respectively. Erosion of the pore volume ($\Delta r = -2$ vx) similarly resulted in drops up to -0.29, -0.08, -0.4, and -0.2 with averages around -0.14, -0.03, -0.15, and -0.09 for samples 1-4, respectively. The minor dilations and erosions ($\Delta r = +1$ vx and $\Delta r = -1$ vx) were effectively linearly proportional to these major changes. The effects of changing pore volume in sample 2 can be seen below in Figure 29. Here the strain predicted for the experiment was subtracted from the strain predicted for each volume alteration case to highlight the changes to the strain field caused by the change of pore volume. The grey end caps of the displayed porosity are regions that would fall outside of the given prediction region and as such no predicted strain was mapped to their surface.

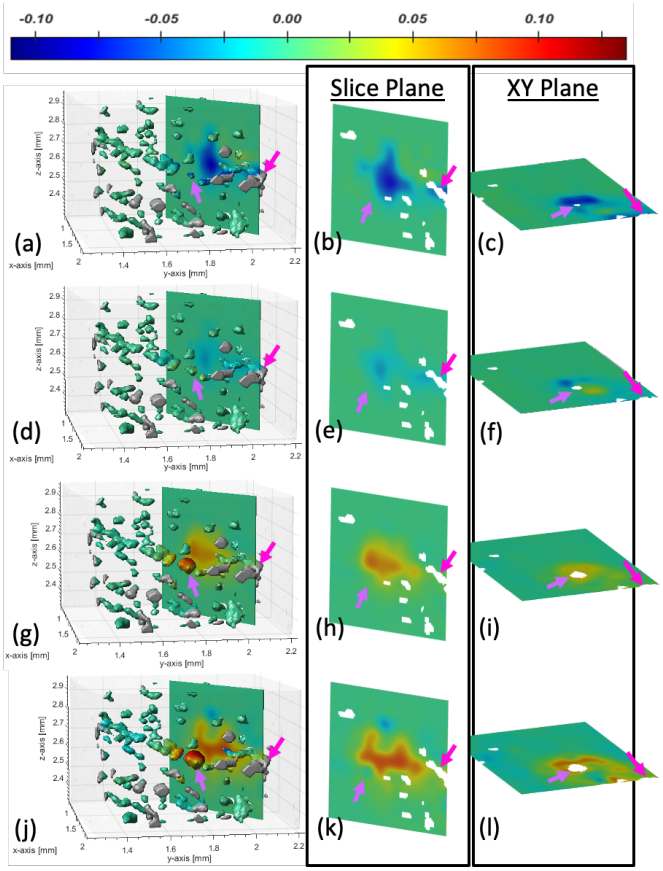

Figure 29. Pore volume changes in sample 2. Visualization of the difference between the prediction on synthetic and the prediction on the experimental defect fields. First column displays the difference in strains in 3D with strain mapped pore surfaces and a vertical slice plane between the critical and altered pores. The second and third columns show the isolated slice plane and a horizontal slice plane, respectively. (a)-(c) Δr = -2 vx, (d)-(f) Δr = -1 vx, (g)-(i) Δr = +1 vx, (j)-(l) Δr = +2 vx.

4.4.3.2 Effect of Distance Between Internal and External Surfaces

Changes in distance between surfaces, both pore-to-pore and pore-to-external, resulted in comparable changes in the predicted results. Since these are highly porous

samples, the retreat from one surface often incorporates the approach of an entirely different surface and vice versa. As such, this discussion will be broken down into considerations of the strain changes in terms of approaching a surface and in terms of retreating from a surface. Samples 1 and 3 experienced greater changes in strain than samples 2 and 4 with respect to these alterations. In general, the approach of a pore towards a new surface will cause a sharp local rise in strain, and these changes in strain magnitude and distribution will affect the pore growth path and thus the path dependence of the sample failure [134, 135]. The original locations of the altered pores had fairly consistent decrease in strain regardless of where the pore was moved. Sample 4 was unique in that moving the altered pore did not cause any major strain changes at its original location. This is largely due to the low amount of intervoid interactions that were observed in sample 4. The greatest increase in local strain due to synthetic pore displacements was found in sample 1 with an increase of around 0.6. Most changes in pore location failed to significantly change the strain at the critical pore of each sample, the one exception being the movement of the altered pore in sample 2 into the region of high local strain of the critical surface defect in sample 2. This resulted in the local strain magnitude increase ~ 1.5 times its predicted value for the experiment configuration. Similar placement of the altered pore into the zones of localization around critical pores in sample 3 and 4 did not produce the same results. For sample 3, this scenario increased the size highly strained region. In sample 4, this motion simply established the first intervoid ligament in this sample. The new intervoid ligament

in sample 4 was accompanied by a drop in strain on the opposing side of the ligament, due to the increase in strain in ligaments often to the exclusion of strain in neighboring regions [115].

Figure 30 below shows the strain at a horizontal cross-section through the altered pore of sample 1 predicted by the model. Alterations shown are the movement of the altered pore 26 voxels up (Δd_{ext} = +26 vx) in Figure 30(a) and 26 voxels down (Δd_{ext} = -26 vx) in Figure 30(c), where up and down are relative to the image frame. Figure 30(b) shows the prediction for the actual configuration of the pores in the experiment, and Figure 30(d) and Figure 30(e) show the difference between the predictions in the synthetic configurations and the experiment configuration. The intensity of the strain drop in the original location of the pore was more or less constant across the two opposing motions, as were the rises in magnitude. One particularly interesting prediction was the strain drop above and to the left of the altered pore in Figure 30(a) and below and to the right of the pore in Figure 30(c). This behavior is in line with the theories of ductile strain between voids, where intervoid strain localization is to the exclusion of strain outside this region [54, 115]. Similar behavior was seen in pore displacement alterations of samples 1 through 3 and in one case in sample 4.

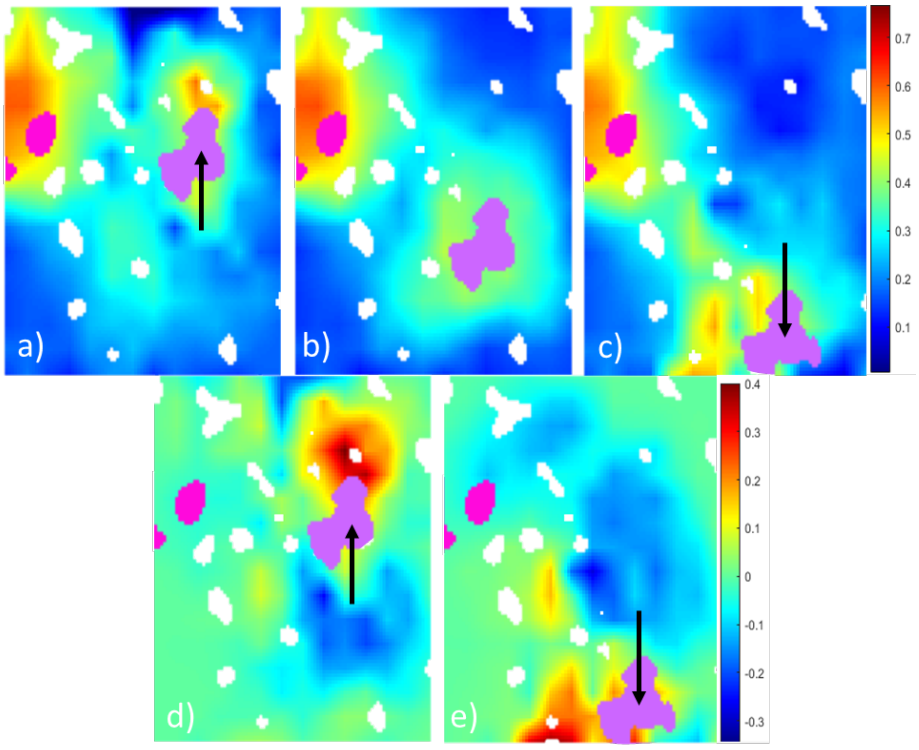

Figure 30. Strain in horizontal cross sections of the sample 1. a) Strain predicted for the vertical movement of the altered pore up towards the top of the image, Δd_{ext} = +26 vx. b) Predicted strain for the true or experimental configuration of pores. c) Predicted strain for the vertical movement of the altered pore down towards the bottom of the image, Δd_{ext} = -26 vx. d) The difference in predicted strain between a) and b). e) The difference in predicted strain between b) and c).

In sample 3, the altered pore will actually coalesce with the critical surface pore at its closest point. In this scenario the strain field was predicted to be carried further into the body of the component, but there were practically no changes in the strain intensity of this now larger pore. As this pore was moved away from the critical surface pore it approached the opposite exterior surface and began to have increased strain towards that surface. The

maximum rise in strain between the experiment and this prediction was 0.29, while the decrease strain at its original location was around -0.25. As seen in Figure 31, the movement away from the critical surface pore was also a movement away from the small porosity that acted as a bridge for coalescence between the critical surface pore and this altered pore. Movement of this pore away from these small coalescence bridge pores causes an overall drop in strain in this region. Accordingly, as the altered pore moved closer to the small coalescence bridge pores, there was a rise in strain of up to 0.34 and a decrease strain near the initial location of up to -0.24. The large rise in strain seen as the altered pore moves into, and actually coalesces/connects with, the critical surface porosity in Figure 31(e), was due to this the fact that the newly enlarged critical surface pore now reached further into the component body with its heightened strain field as seen in Figure 31(a).

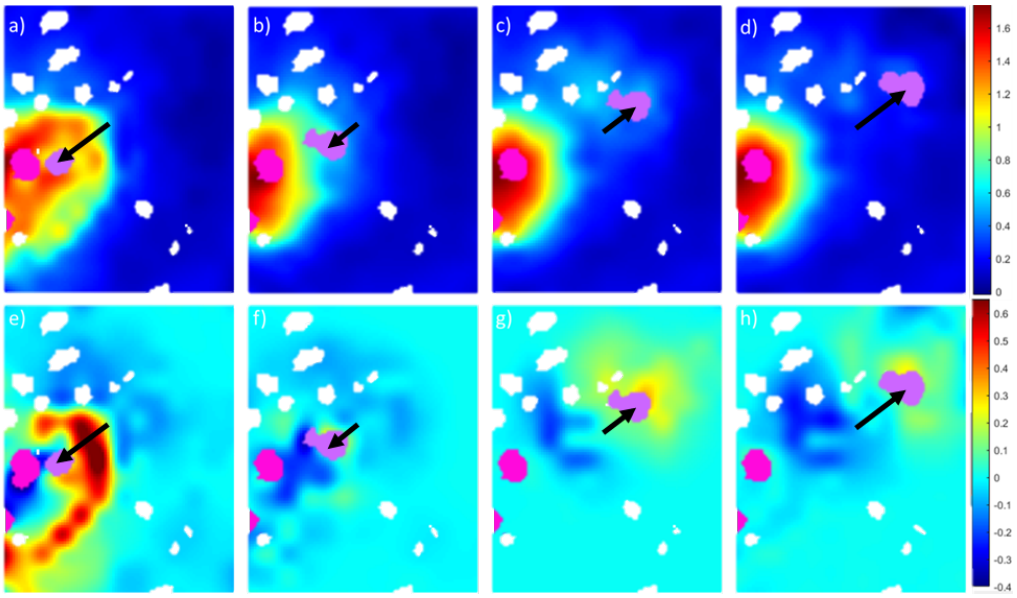

Figure 31. XY cross-sections showing the movement relative to the critical surface pore of the altered pore in sample 3. a) Δd_{crit} = -26 vx, b) Δd_{crit} = -13 vx, c) Δd_{crit} = +13 vx, d) Δd_{crit} = +26 vx. e-h) exhibit the difference between the experiment measurement for this cross-section and the predictions of the altered configurations in a-d), respectively.

Interestingly, it is evident that movement of the pore close to the zone of critical strain produced significantly different results than actually connecting the altered pore to the critical surface pore in this zone. For all other cases, the overall strain at the critical site was relatively unaffected, but the coalescence path was altered. For the case of joining the two pores, the local strain in the zone was morphologically altered to distribute itself more towards the small coalescence bridge pores, but the ultimate magnitude of the strain in this zone does not change significantly. The decrease in strain as the altered pore approached

the critical surface pore seems paradoxical at first glance, however this drop in strain was actually accompanied by a rise in strain to a point on the surface of the critical pore that was actually closer to the altered pore. The reason for this is that the motion of the altered pore does not lie perfectly within the cross-section shown, as was evident by the change in pore shape between frames. In general, the drop in strain at the old location of the altered pore remains around -0.25 for all scenarios. The difference in the predicted strains and the experiment for an even steeper diagonal movement through the component body is shown in Figure 32.

This extension of the ML model with small synthetic alterations is limited by the size of the alterations and the need to keep changes within the range of data used to train the models. As with the ML model itself, these extensions are limited to one material system and similar component geometries. Additionally, the predictions of the model are tied to the uniaxial loading of the experiments and cannot be used to predict the strain in other loading scenarios. As such, future work lies in expanding the range of the porosity conditions performing additional in-situ loading test to be used for model training. Other model expansions, such as including material properties or build parameters in the list of features are possible. Ultimately, the goal of this research has been to show how models developed directly from measured data can be used to further the understanding of deformation in highly porous systems.

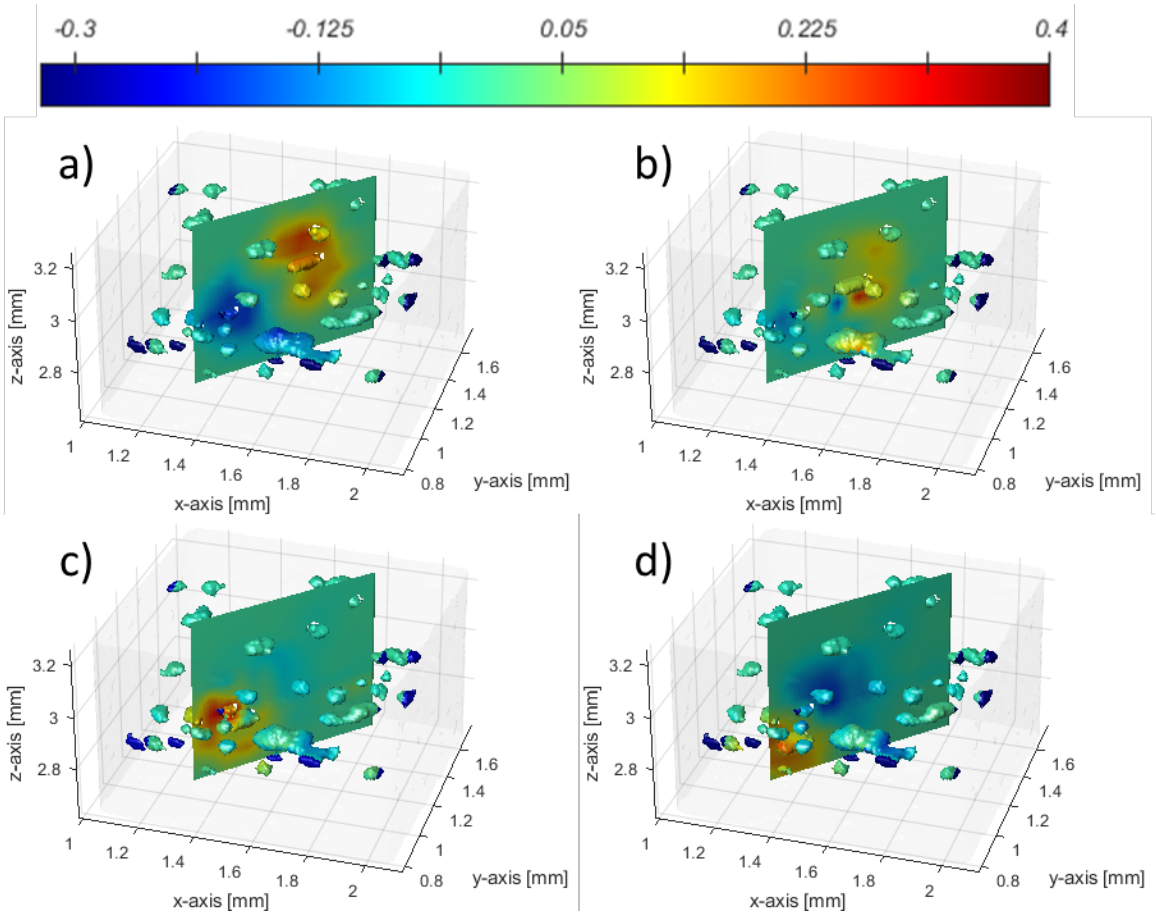

Figure 32. Difference maps of the strain changes for moving the altered pore in sample 3. a) Δd_{ext} = +26 vx, b) Δd_{ext} = +13 vx, c) Δd_{ext} = -13 vx, and d) Δd_{ext} = -26 vx.

4.4.4 Generalization and Limitations of the Models

The models developed in the present work serve as an alternative to more traditional fracture mechanics analysis. There are complex states of stress occurring within the microstructures shown. Since yield criteria require some knowledge of principal loading

directions and thus the state of the stress, fracture mechanics becomes impractical with complex microstructures. Within these microstructures, especially within regions where failure is likely to occur, measurements or assumptions of yield stress cannot be applied, because the magnitude and directionality of the loading are not clear. As noted by Noell et al. in Ref. [133], there are a possible 7 mechanisms of ductile rupture and they can exist simultaneously. This work has stressed the intervoid necking mechanism, but as seen for sample 2 in Appendix A the void sheeting mechanism and thus shear mechanisms are also at play. However, in less porous samples traditional fracture mechanics will play an important role in predicting yield. Given that models developed herein are inherently dependent on the initial porosity of the specimens, there will be a soft transition in initial porosity volume fraction that will yield the models less effective and traditional fracture mechanics more effective. It would appear that the tipping point for the defect driven models developed herein to be valid requires that the initial ratio be greater than 0.48%. This is based on the weaker performance of the machine learning model in predicting the axial strain in sample 4 vs its robust predictions for samples 1-3. Even with an approximation of minimum porosity needed, consideration should be taken for both defect size and density as shown by Table 1. Ultimately, the models' efficacy increases with initial porosity, pore size, and the resolvability of the porosity.

Expansion of the present models to other material systems will require some alteration as discussed below. Traditionally manufactured 316L SS has no precipitates and therefore almost no void nucleation, it is unlikely that AM 316L will have much in terms of precipitates either. The in-situ experiments performed did not have sufficient resolution to observe any void nucleation, but the morphological evolution of the components does give rise to emergent porosity, that since originally unknown and unaccounted for serves a similar function in this work. These microvoids will affect the localization behavior as shown by Ref [114], but as seen by the accuracy of the non-local and ML models they are not dominating the behavior and the localization of strain can still be predicted without knowledge of their existence. As long as lack of fusion (LOF) porosity defects are significantly larger, the model assumptions and the formulation of the model itself are likely still valid. Assuming that other material systems are sufficiently porous and ductile the model behavior will only change relative to the specifics of the non-local weighting and the data provided to the machine learning model, as new data with the new material system will need to be provided for accurate ANN predictions. There should be no reasons for the reformulation of the model formulations or architectures. This does of course exclude brittle materials as discussed in the Chapter 1 discussion.

The loading of components in uniaxial tension provided a solid foundation upon which to build formulations of strain localization and models to predict it. However, these

formulations are not necessarily valid for other stress-states, such as pure-shear or bending. The framework of the machine learning model will likely require less change than the non-local formulation. The machine learning model will likely pick up a few additional loading parameters as inputs for more complex loading scenarios but could also easily be altered to have multiple outputs for each component of strain desired. Additional loading direction terms could be applied to the non-local formulation to account for complex loading. But if the ductile behavior varies significantly from that in the uniaxial tension, as may be the case for loading in pure-shear, a ground up reformulation of the non-local model would be needed. The role of the non-local formulation would remain the same, but some alterations should be considered in terms of actual field shape. This could take the form of changing the nature of the field dot product with vectors of the defects surfaces to better represent the state of the shear stress at or near the surface.

Finally, while the ANN model can be extended to look at the effects of things like, defect shape, density and spatial uniformity; variation of the data outside of the training envelope would not provide accurate predictions. Further, detailed control of these parameters requires more purposeful planning and understanding of how it will affect the regions around the alteration. It is technically possible to design completely artificial scenarios of porosity, however, doing so would be far more difficult to stay within this envelope.

CHAPTER 5. CONCLUSIONS

5.1 Summary

In the present study, the tensile failure of AM components with porosity defects was evaluated using in situ XCT. These data were useful for direct observations of initial defect structure, pore growth and coalescence, as well as quantitative mapping of strain localizations made using DVC-based measurements. From the present results, it was found that tensile performance in terms of elongation to failure of these AM components was directly tied to their unique defect structures. As can be seen from Figure 16, there is a significant difference between the topology of a sphere and a large pore in these components. This further emphasizes the need for realistic porosity modelling to understand the mechanics of real porous systems. Characteristics of the porosity distribution, including presence of porosity at the surface or near-surface of components, as well as the proximity of pores to each other were found to influence the evolution of failure in these components. Early onset of failure was found to be associated with the availability of neighboring porosity that can allow for rapid progression of the fracture path. Analysis of the strain distributions within the components found that strain associated with surface porosity was higher than that of the porosity distributed within the sample interior. Further, higher intervoid strains were observed to be associated with promoted

growth and coalescence of porosity. Under conditions wherein critical pores did not neighbor other pores, samples behaved in a manner more typical of wrought materials, including exhibiting necking instability. As such, it is revealed that early failure of AM components with porosity defects will depend not only on characteristics like distance from the surface or size of the defects, but also on the adjacency of the defects in the component.

Defect features were calculated for each defect of each sample and component features were calculated for each sample. Features were expanded uniformly to the bounds of each defect's watershed segment and then down sampled as their minimum, mean, and maximum at calculation points of the DVC analysis. This both blindly approximated spatial regions of interest and smoothed the data across regions of interest to allow for a more organic approximation of the feature space. Correlations were drawn between the down sampled features and the calculated axial strains at each DVC analysis point. This is the first work to show a comprehensive list of local feature characteristics correlated with local strain.

The nonlocal influence analysis proposed in this work performed well at predicting how the strain would localize just before failure with voxel-for-voxel correlations of up to 73% and at the lowest just above 55%. This work has also considered at the correlations between local defect and component features with local axial strain. The correlation coefficients showed that both the nonlocal influence analysis and pore volume were highly

correlated with this strain. Sample 4 showed dissimilar correlations with the other 3 in terms of nonlocal influence, pore volume, and the distance from the gage surface. Sample 4 also presented different morphological evolution behavior. Interestingly, the local pore volume fraction did not correlate well with the development of local strain. This stands at odds with the common practice of using void volume fraction as the sole defect parameter in FE analyses [115, 136]. However, in the present case the poor correlation may have more to do with the relatively smaller sampling window than those used for FE void volume fraction.

Machine learning models were tested to predict the magnitude and localization of strain based on all features, and it was found that a two hidden layer, 72 and 36 neuron model outperformed both the more and less complex model architectures at predicting strain in portions of the data that were withheld from the training and validation. Regression values were greater than 0.92 for the robust combined prediction. The models were then used to show the effects of simple defect morphology changes on the localization of strain in the critical regions of each component. It was found that the distance between defect surfaces was the most influential factor for strain localization with decreases between surfaces generally resulting in rises in strain and increases in this distance resulting in drops in local strain. The strength of the response varied from sample to sample, but in general several samples exhibited far greater sensitivity to the morphological change. This is in

part due to the large size of surface pores in specific samples that were being supported by the altered porosity. This study finds that large exterior-surface tangent and or exterior-surface adjacent porosity is the most critical, followed closely by surface-to-surface distance of interior pores adjacent to these critical regions.

5.2 Contributions

The following contributions have been made in this work:

- Comprehensive understanding of failure in AM components from in situ observations.
    - Determined the evolution of internal defects and their role in overall failure of the component.
    - Provided a description of how damage accrues from morphological changes in defects and association of those changes with the region's strain.
    - Provided full field 3-dimensional displacement and local axial strain measurements for 316L stainless steel samples produced by LPBF.
- A comprehensive description of AM defects, including locally-varying character of these defects and quantification of critical morphological parameters of these defects.

- A correlation-based understanding of how specific defect and component features changed the mechanical response for AM components.
- A weighted analytical formulation for predicting where strain will localize in porous solids.
- A robust model for the mechanical behavior of porous solids that is capable of predicting where damage will occur and how the defects will lead to failure.
    - Demonstrated that very simple ANN networks of 9 neurons and a single hyperbolic tangent transfer function layer are capable of explaining >75% of the variation in local measured strain.
    - Provided a framework for the direct integration of DVC strain measurements into machine learning models for the prediction of local strain.
- A model-based understanding of how changes in specific defect parameters cause changes in the mechanical response for AM components.

5.3 Future Work

This research represents an early point in the employment of XCT and in-situ testing to measure ductile deformation and failure, and as such, further experimental work

is needed to test other geometries and material systems. Additional, expansions to other modes of loading will also follow.

Further work is also needed in the analysis via full-field 3D displacements and strains. Improvements to correlation techniques to account for the unique convolution geometric information as described by Beer's Law are necessary. Where ostensibly advances in laboratory XCT systems and reconstruction algorithms will undoubtably allow for greater reconstruction coherence and detail resolvability. This is especially true for x-ray scatter sensitive techniques that are capably of further patterning the voxelized digital twin's with information about the unique refraction properties of different materials and different material phases. There is even potential to extend the voxel format to an RGB style of data profundity that stacks this additional pattern information in higher dimensions.

There is always room to define and quantify additional characteristics and features of each digital twin and its defects. Consequently, any truly unique metric would naturally enrichen the development of shallow network models to predict local strain. One example of this would be the development of robust techniques to both distinguish and measure local surface curvature, and then to determine how it affects the surrounding area. There is also additional work to be done in tying feature and material metrics to the weighting of the non-local model. Ultimately, the goal of future work will be to improve the robustness and range of the ML modeling efforts; however, there is additional potential incorporating

this data into more traditional finite-element techniques in terms of boundary conditions, classifying the gradient of material properties with greater local accuracy, or even developing better constitutive laws based on the observed morphological and strain evolutions.

APPENDIX A. SUPPLEMENTARY FIGURES

A.1 Radiograph Timeline of Sample Deformation

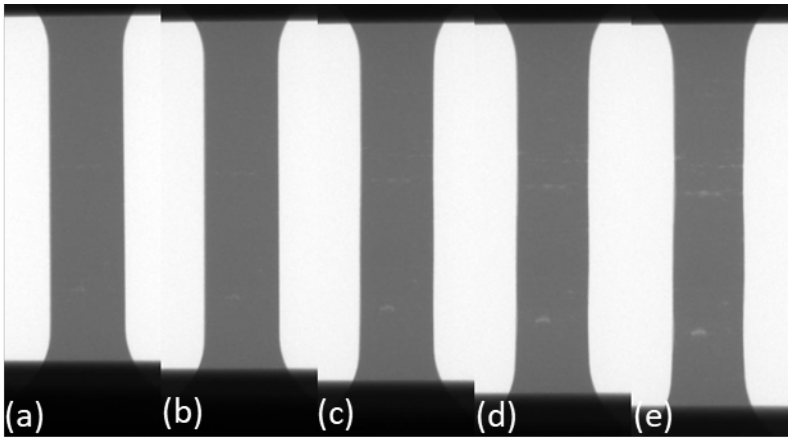

Supplementary Figure 1. Radiograph projections of sample 1. Front view at global strains: (a) 0.0000%, (b) 0.5643%, (c) 3.7354%, (d) 6.9734, (e) 10.3672.

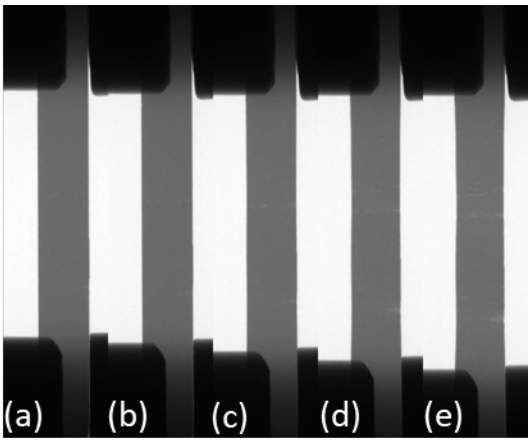

Supplementary Figure 2. Radiograph projections of sample 1. Side view at global strains: (a) 0.0000%, (b) 0.5643%, (c) 3.7354%, (d) 6.9734, (e) 10.3672.

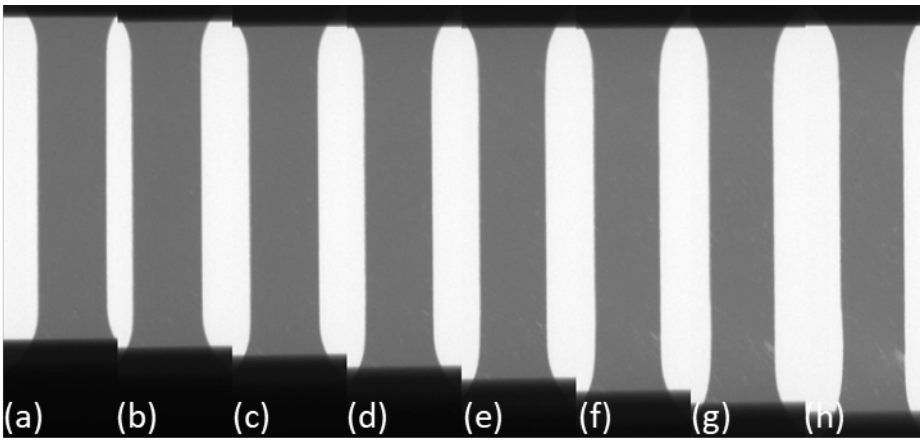

Supplementary Figure 3. Radiograph projections of Sample 2. Front view at global strains: (a) 0.0000%, (b) 0.3912%, (c) 1.8721%, (d) 5.2516%, (e) 8.2976%, (f) 11.9025%, (g) 15.0341%, (h) 18.00301.

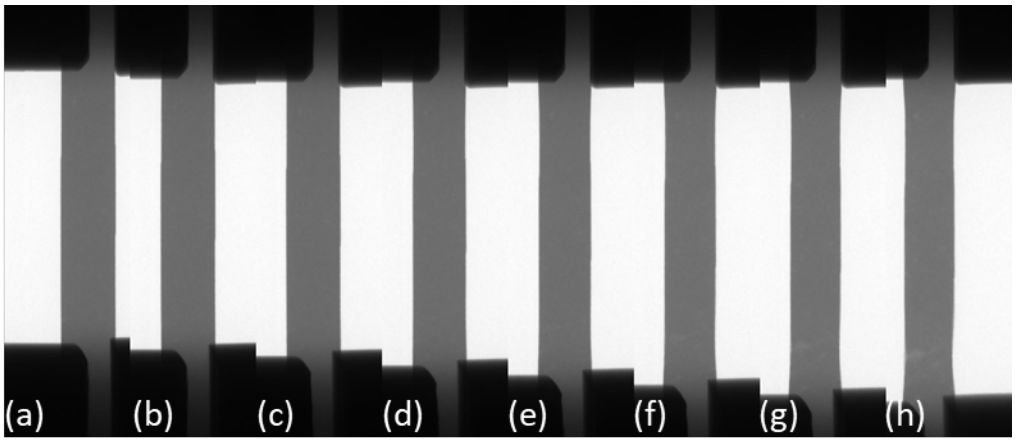

Supplementary Figure 4. Radiograph projections of Sample 2. Side view at global strains: (a) 0.0000%, (b) 0.3912%, (c) 1.8721%, (d) 5.2516%, (e) 8.2976%, (f) 11.9025%, (g) 15.0341%, (h) 18.00301.

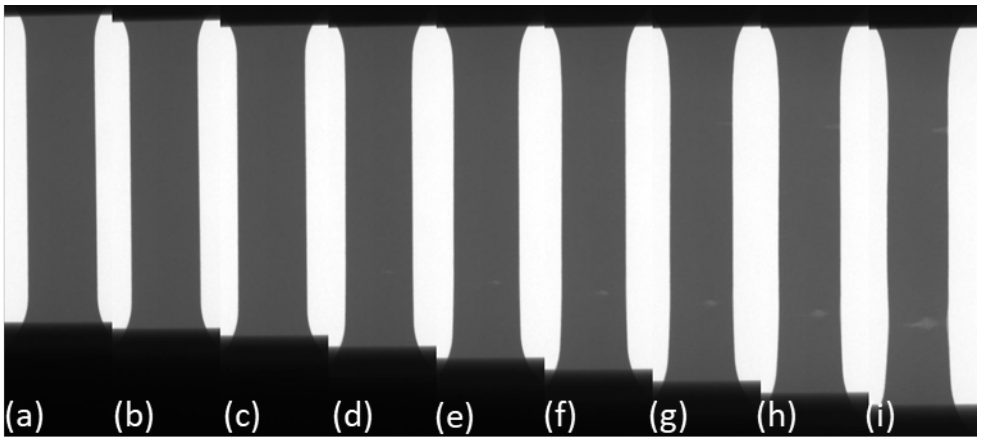

Supplementary Figure 5. Radiograph projections of Sample 3. Front view at global strains: (a) 0.000%, (b) 0.9524%, (c) 2.6819%, (d) 5.4640%, (e) 8.2976%, (f) 11.9746%, (g) 15.2186%, (h) 18.2241%, and (i) 21.1419%.

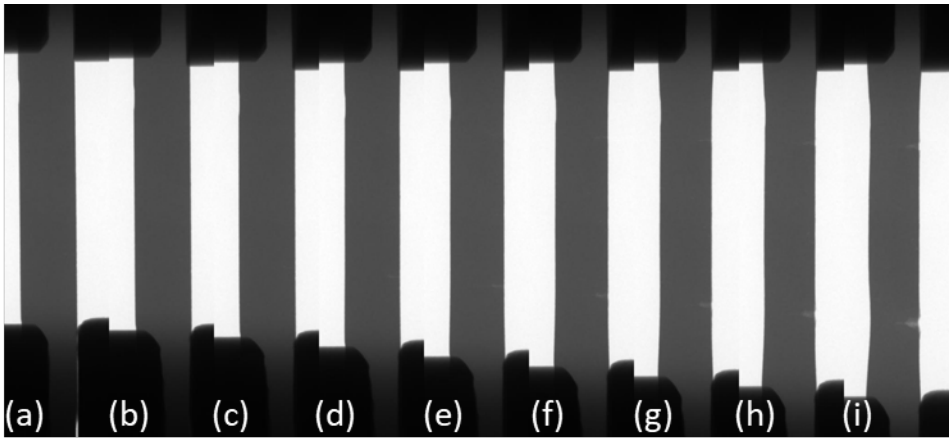

Supplementary Figure 6. Radiograph projections of Sample 3. Side view at global strains: (a) 0.000%, (b) 0.9524%, (c) 2.6819%, (d) 5.4640%, (e) 8.2976%, (f) 11.9746%, (g) 15.2186%, (h) 18.2241%, and (i) 21.1419%.

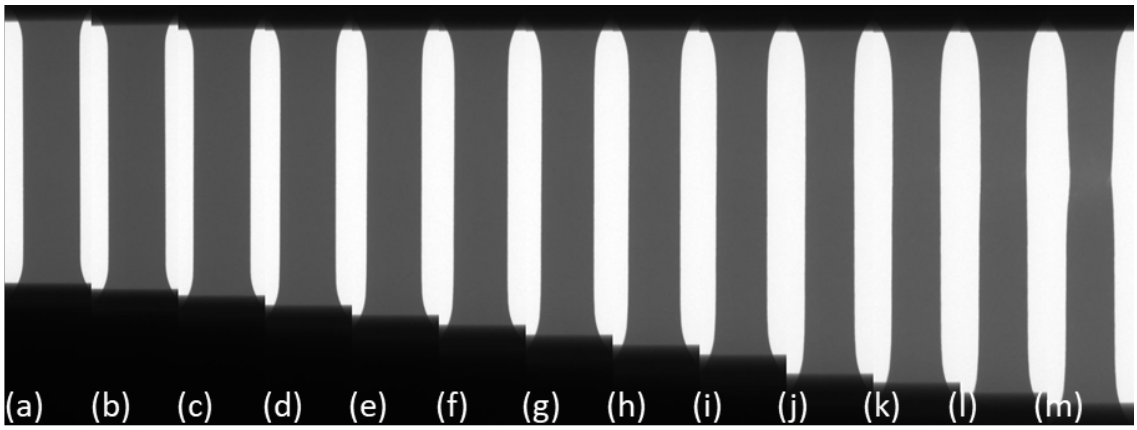

Supplementary Figure 7. Radiograph projections of Sample 4. Front view at global strains: (a) 0.0000%, (b) 0.7351%, (c) 2.736513, (d) 4.410781, (e) 7.5046%, (f) 10.6992%, (g) 13.9121%, (h) 16.8433%, (i) 19.7903%, (j) 25.5049%, (k) 27.7057%, (l) 30.5934%, and (m) 33.6317%.

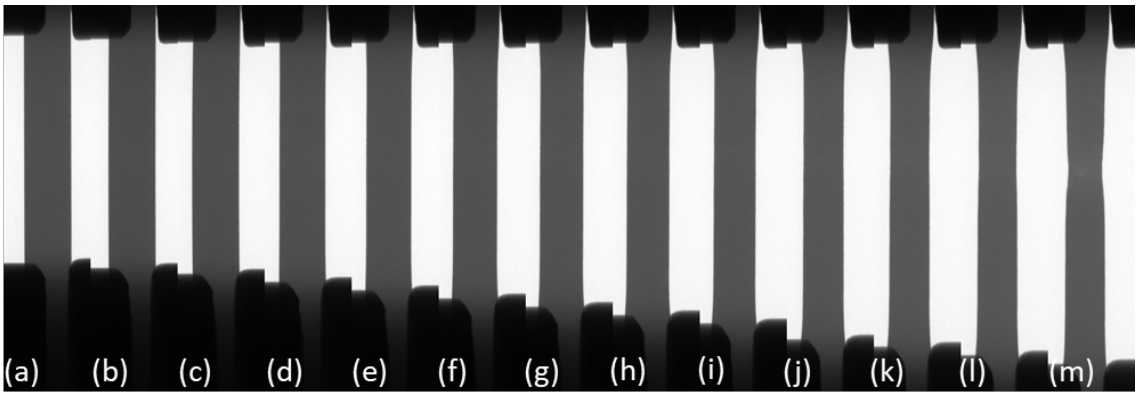

Supplementary Figure 8. Radiograph projections of Sample 4. Side view at global strains: (a) 0.0000%, (b) 0.7351%, (c) 2.736513, (d) 4.410781, (e) 7.5046%, (f) 10.6992%, (g) 13.9121%, (h) 16.8433%, (i) 19.7903%, (j) 25.5049%, (k) 27.7057%, (l) 30.5934%, and (m) 33.6317%.

A.2 Strain Field Cross-sections

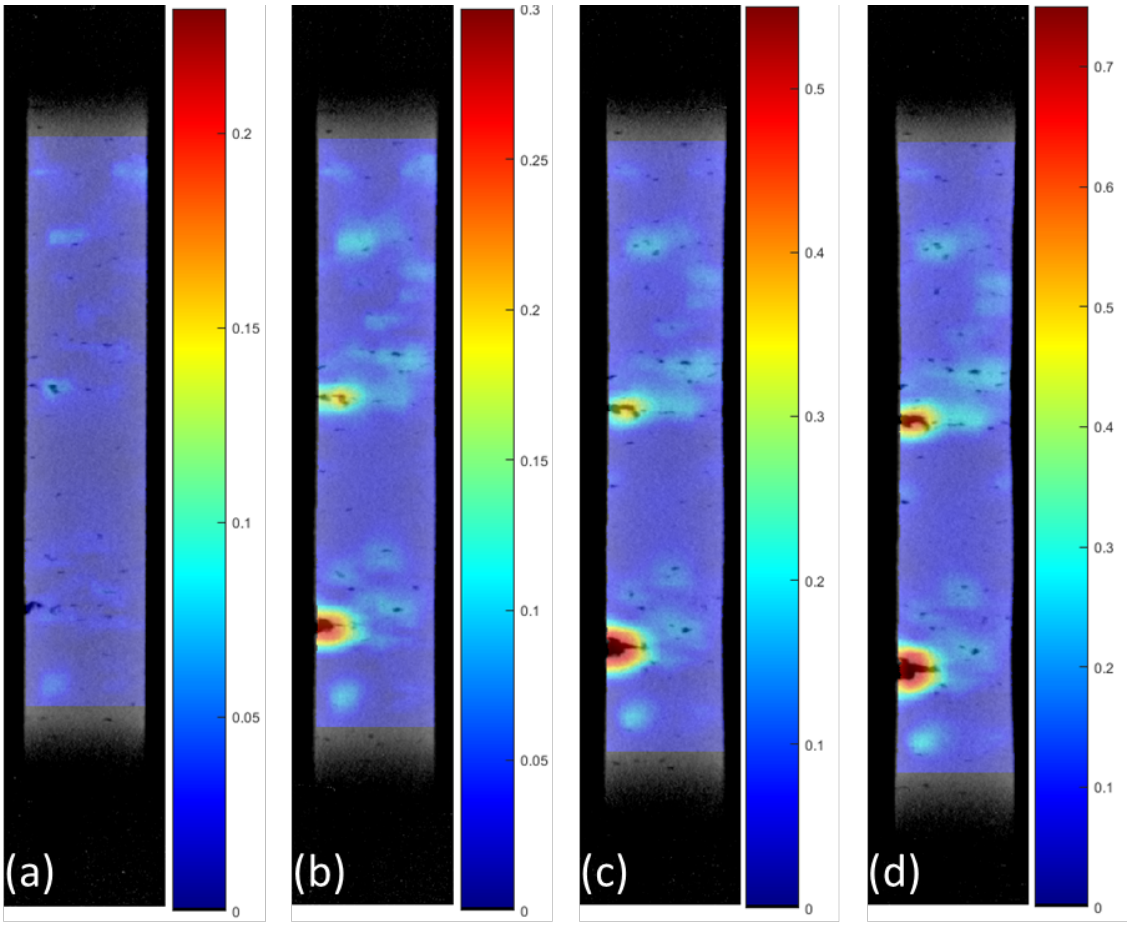

Supplementary Figure 9. Strain field evolution in sample 1. Vertical cross-sections at global strains: (a) 0.5643%, (b) 3.7354%, (c) 6.9734, (d) 10.3672.

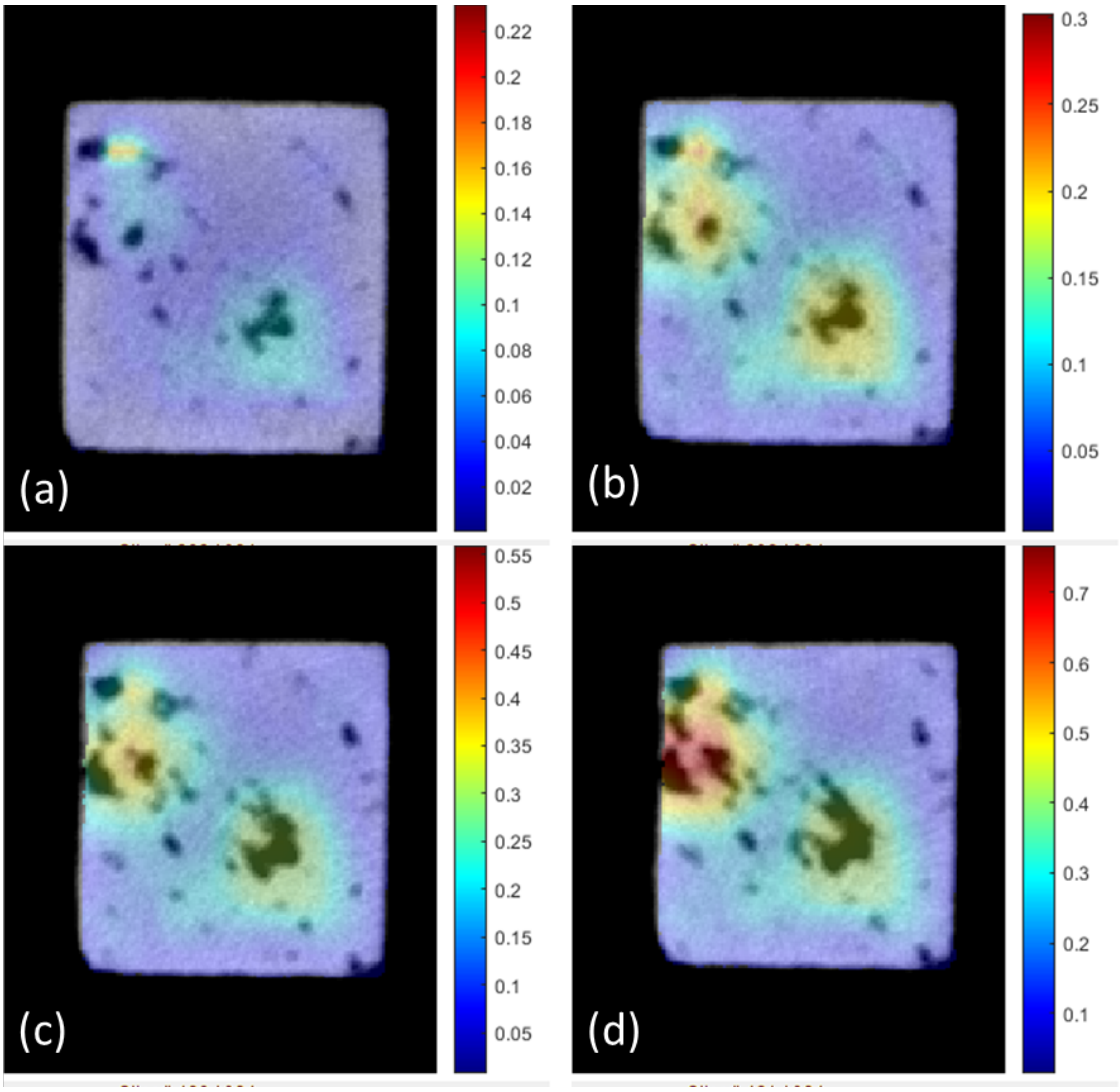

Supplementary Figure 10. Strain field evolution in Sample 1. Horizontal cross-sections at global strains: (a) 0.5643%, (b) 3.7354%, (c) 6.9734, (d) 10.3672.

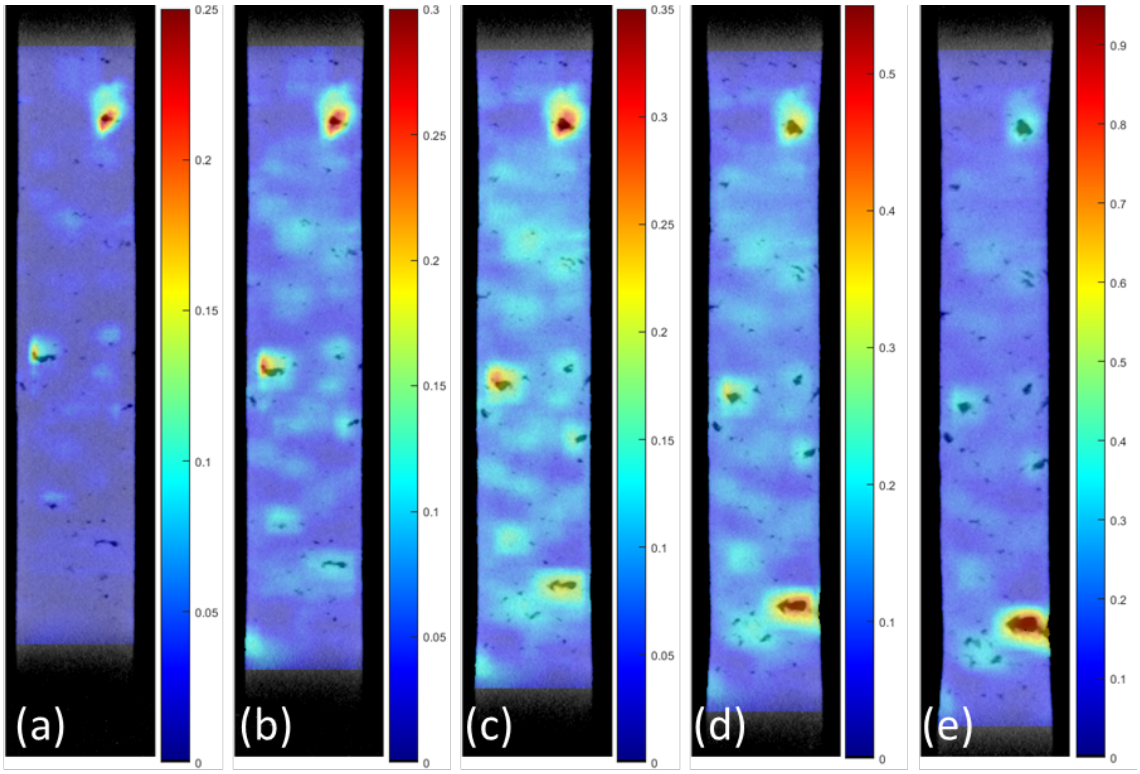

Supplementary Figure 11. Strain field evolution in Sample 2. Vertical cross-sections at global strains: (a) 1.8721%, (b) 5.2516%, (c) 8.2976%, (d) 11.9025%, (e) 15.0341%.

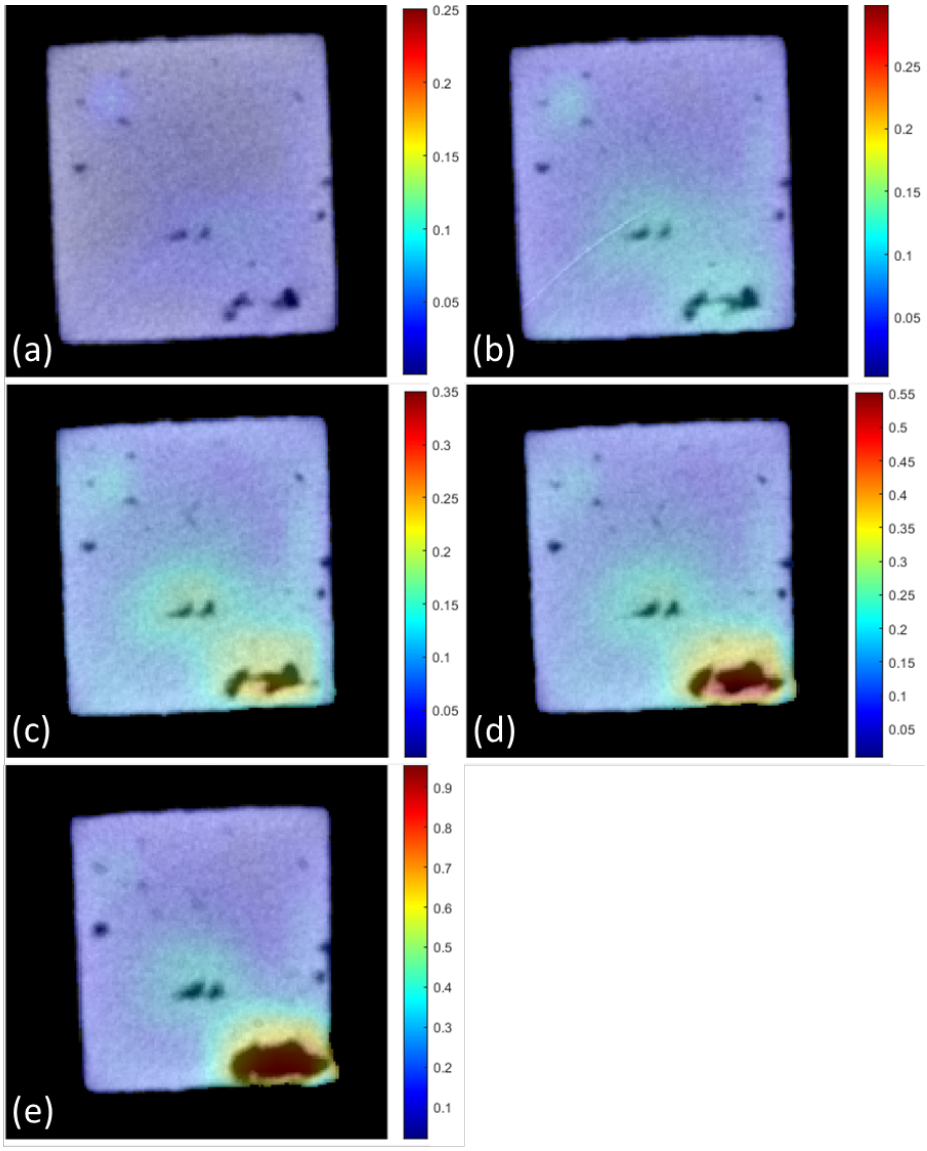

Supplementary Figure 12. Strain field evolution in Sample 2. Horizontal cross-sections at global strains: (a) 1.8721%, (b) 5.2516%, (c) 8.2976%, (d) 11.9025%, (e) 15.0341%.

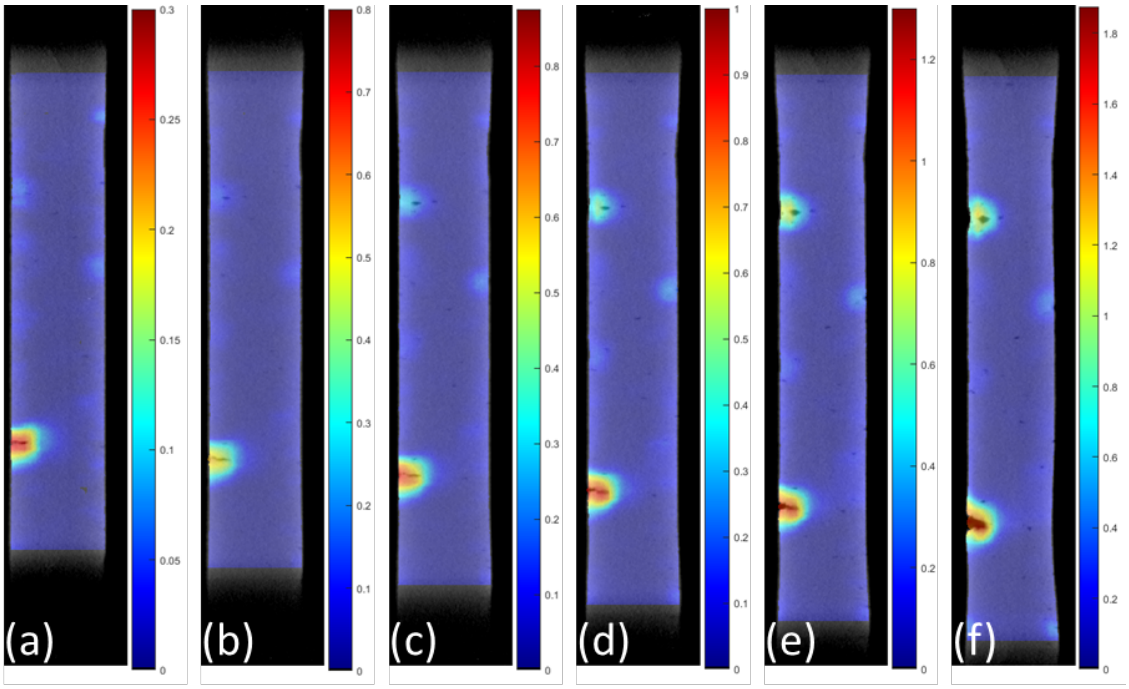

Supplementary Figure 13. Strain field evolution in Sample 3. Vertical cross-sections at global strains: (a) 5.4640%, (b) 8.2976%, (c) 11.9746%, (d) 15.2186%, (e) 18.2241%, and (f) 21.1419%.

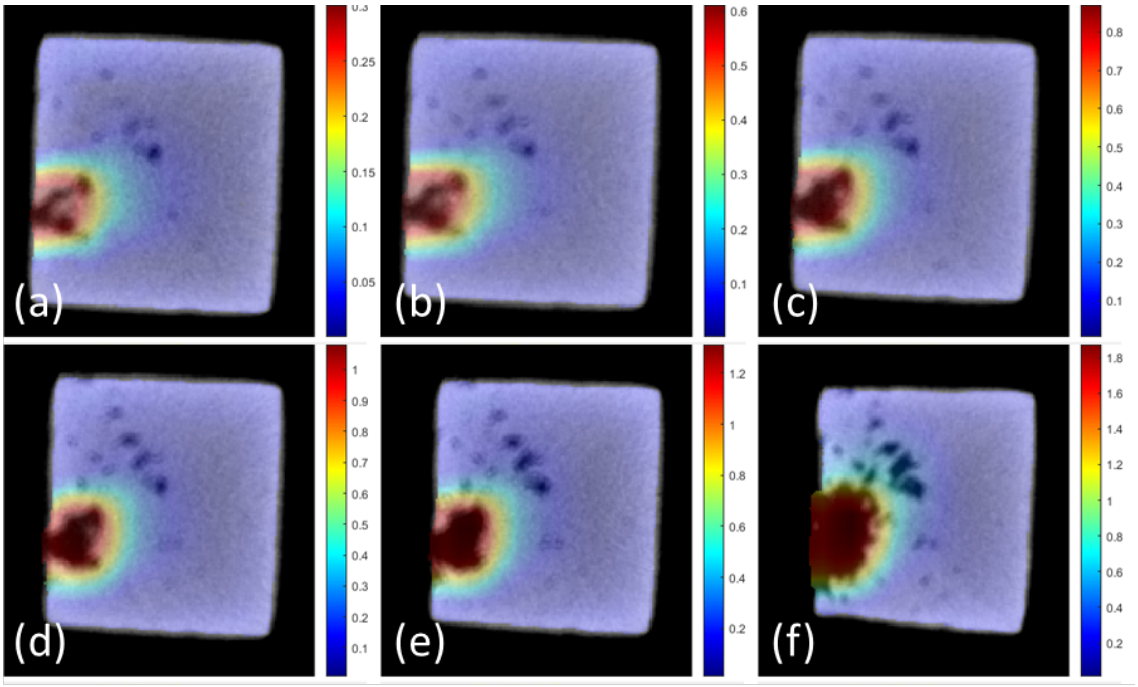

Supplementary Figure 14. Strain field evolution in Sample 3. Horizontal cross-sections at global strains: (a) 5.4640%, (b) 8.2976%, (c) 11.9746%, (d) 15.2186%, (e) 18.2241%, and (f) 21.1419%.

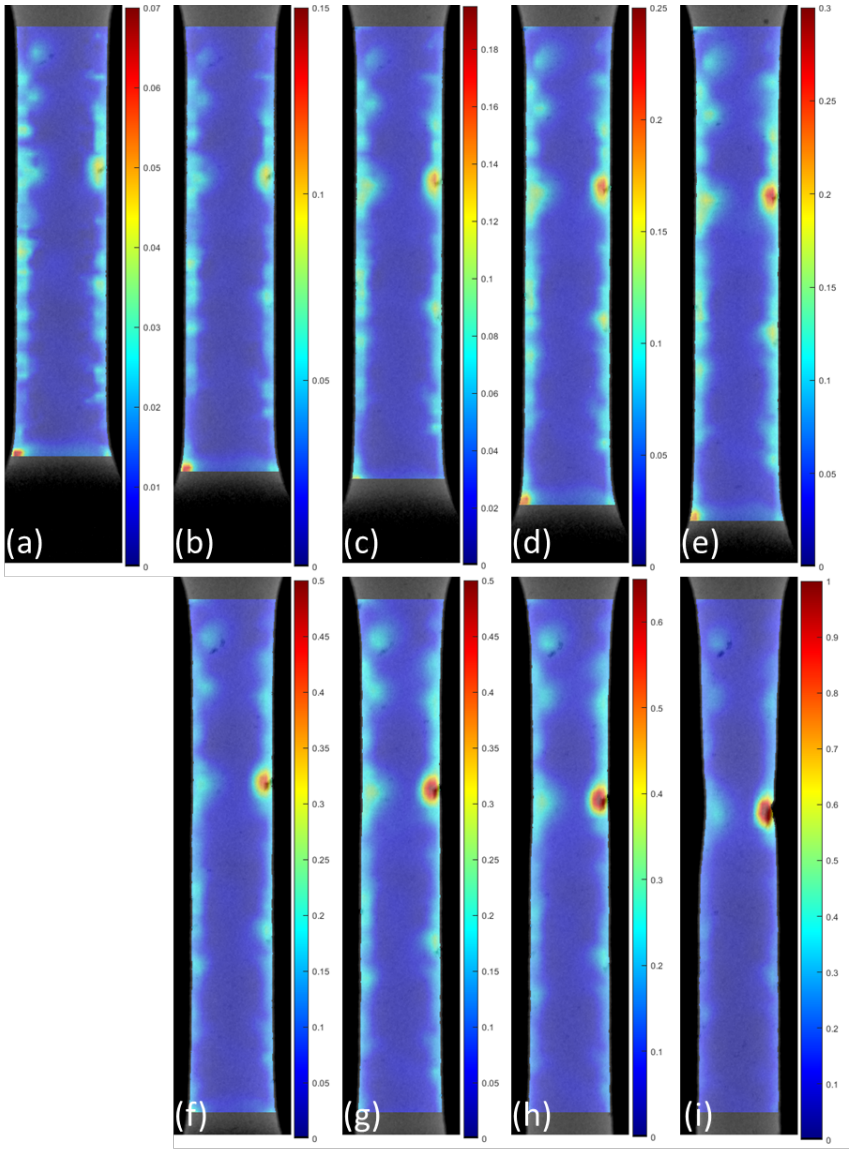

Supplementary Figure 15. Strain field evolution in Sample 4. Vertical cross-sections at global strains: (a) 7.5046%, (b) 10.6992%, (c) 13.9121%, (d) 16.8433%, (e) 19.7903%, (f) 25.5049%, (g) 27.7057%, (h) 30.5934%, and (i) 33.6317%.

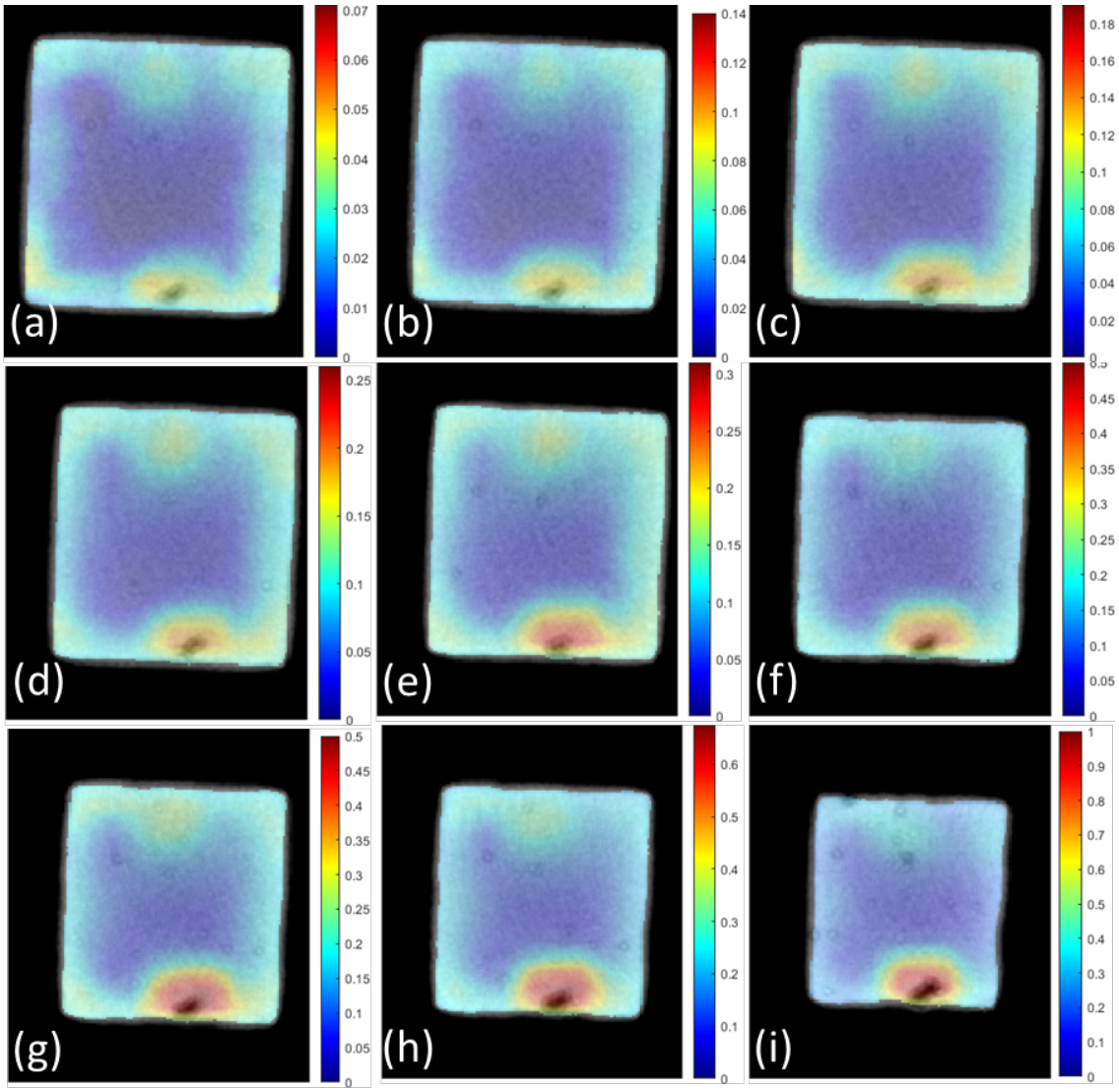

Supplementary Figure 16. Strain field evolution in Sample 4. Horizontal cross-sections at global strains: (a) 7.5046%, (b) 10.6992%, (c) 13.9121%, (d) 16.8433%, (e) 19.7903%, (f) 25.5049%, (g) 27.7057%, (h) 30.5934%, and (i) 33.6317%.

A.3 Morphological Evolution of Defects through Segmentation

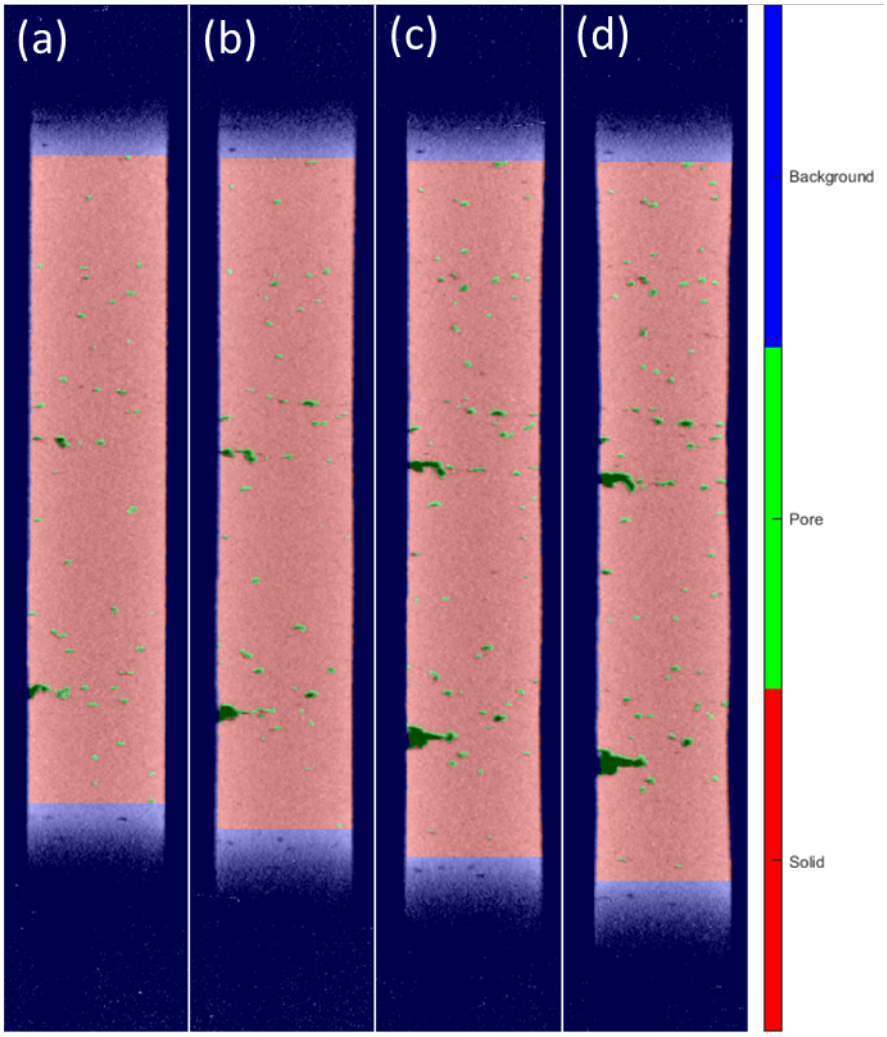

Supplementary Figure 17. Morphological evolution in Sample 1. Vertical cross-sections at global strains: (a) 0.5643%, (b) 3.7354%, (c) 6.9734, (d) 10.3672.

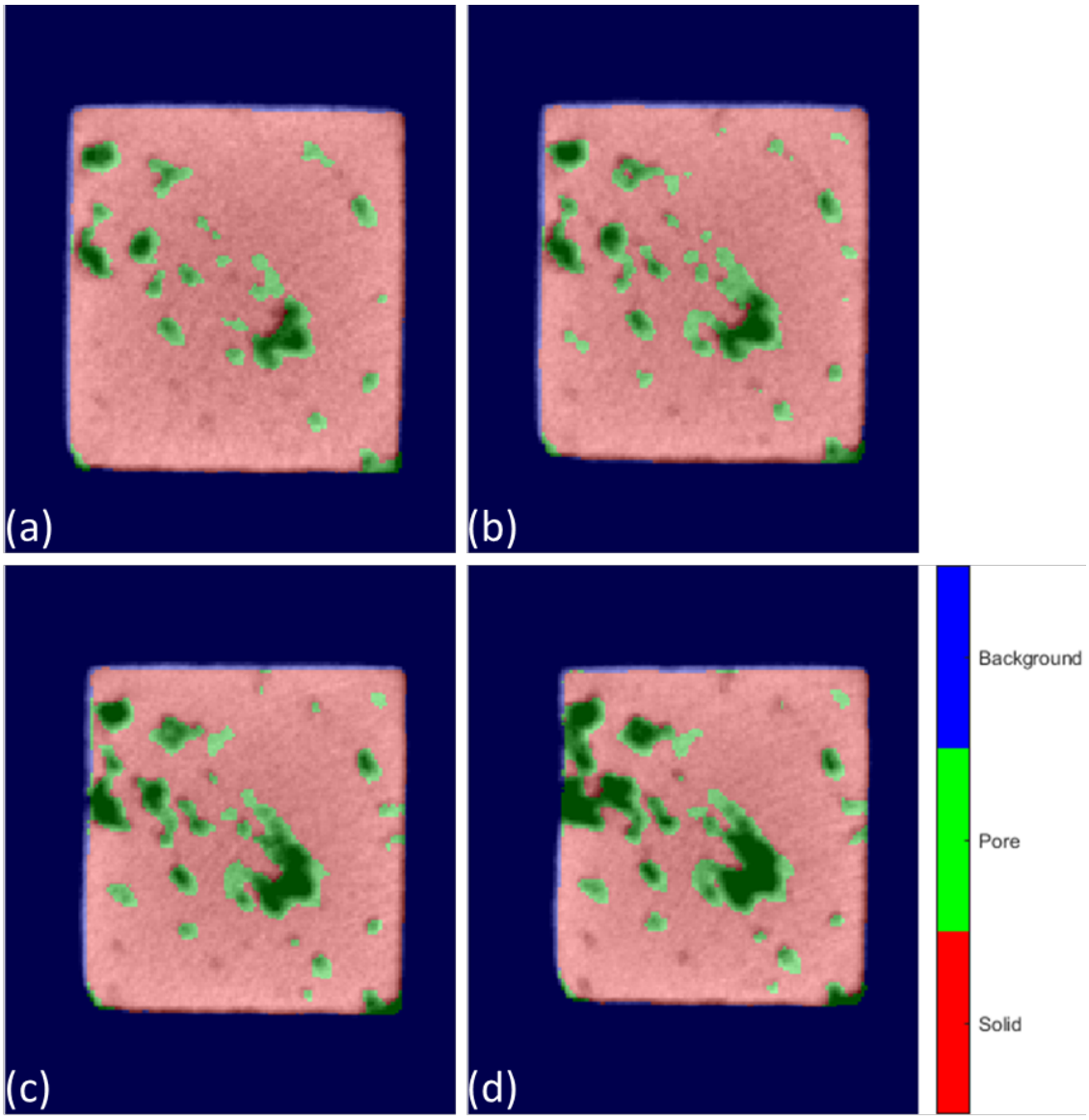

Supplementary Figure 18. Morphological evolution in Sample 1. Horizontal cross-sections at global strains: (a) 0.5643%, (b) 3.7354%, (c) 6.9734, (d) 10.3672.

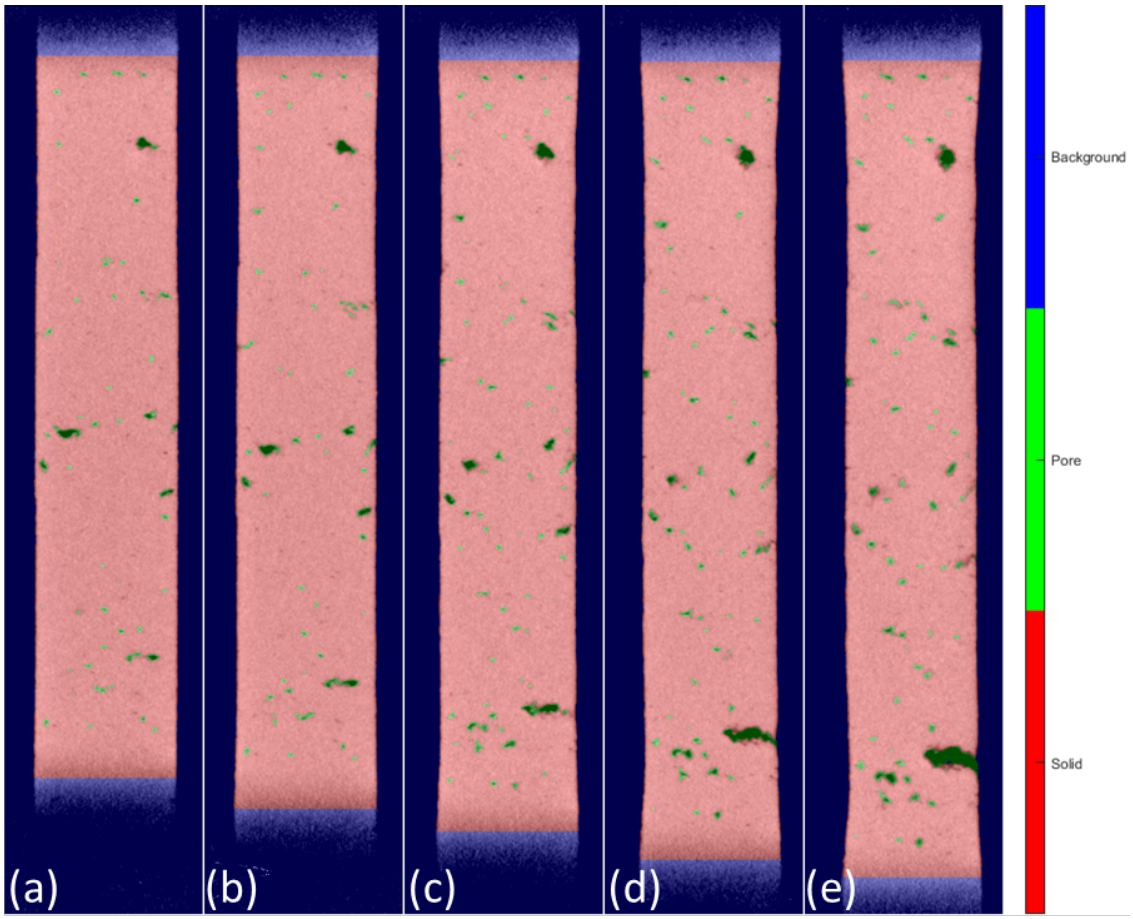

Supplementary Figure 19. Morphological evolution in Sample 2. Vertical cross-sections at global strains: (a) 1.8721%, (b) 5.2516%, (c) 8.2976%, (d) 11.9025%, (e) 15.0341%.

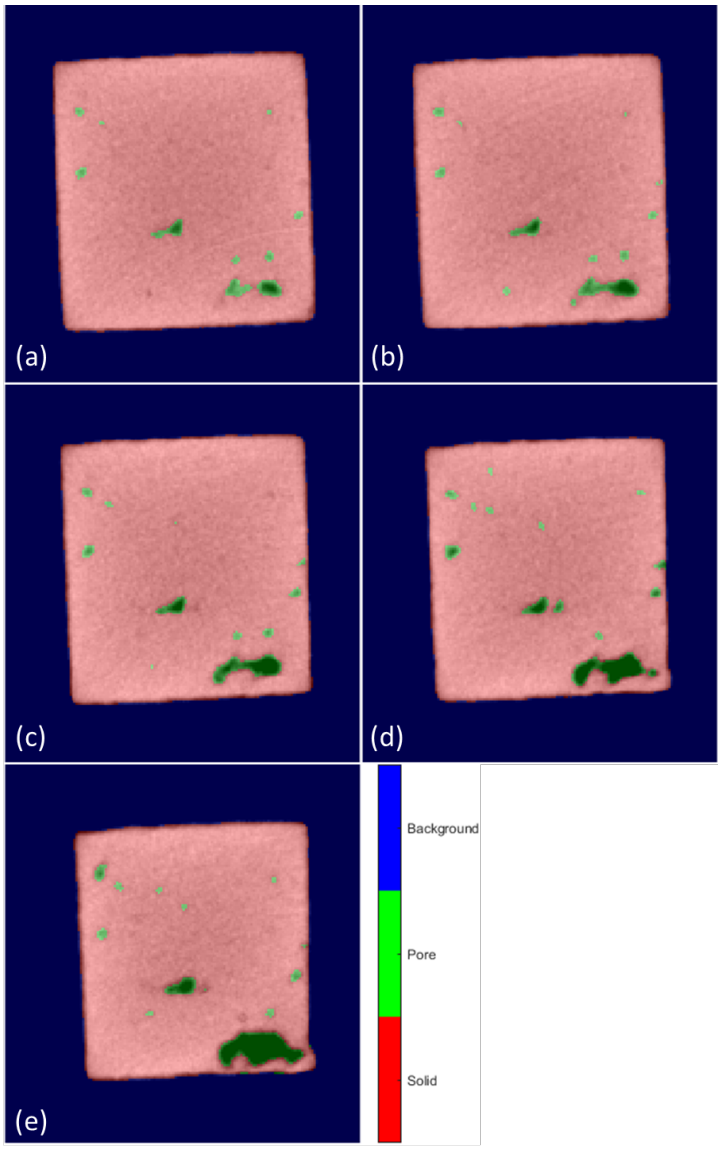

Supplementary Figure 20. Morphological evolution in Sample 2. Horizontal cross-sections at global strains: (a) 1.8721%, (b) 5.2516%, (c) 8.2976%, (d) 11.9025%, (e) 15.0341%.

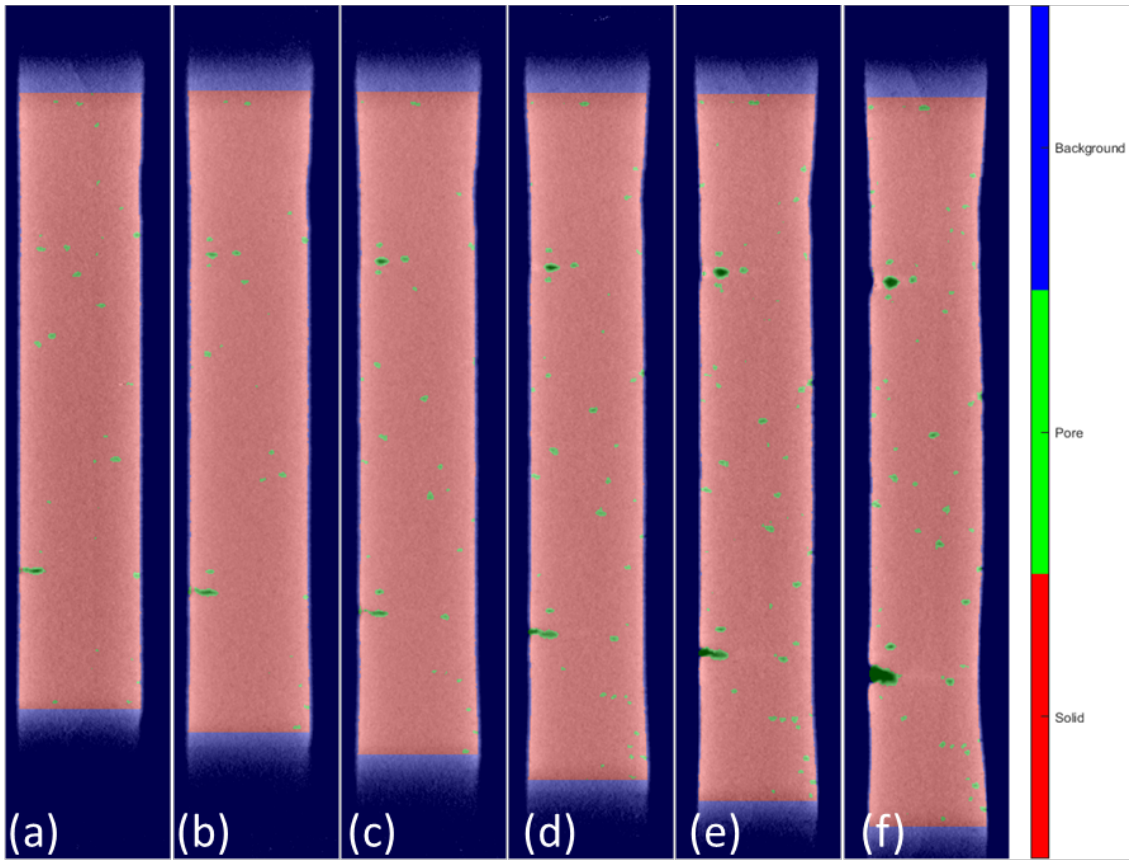

Supplementary Figure 21. Morphological evolution in Sample 3. Vertical cross-sections at global strains: (a) 5.4640%, (b) 8.2976%, (c) 11.9746%, (d) 15.2186%, (e) 18.2241%, and (f) 21.1419%.

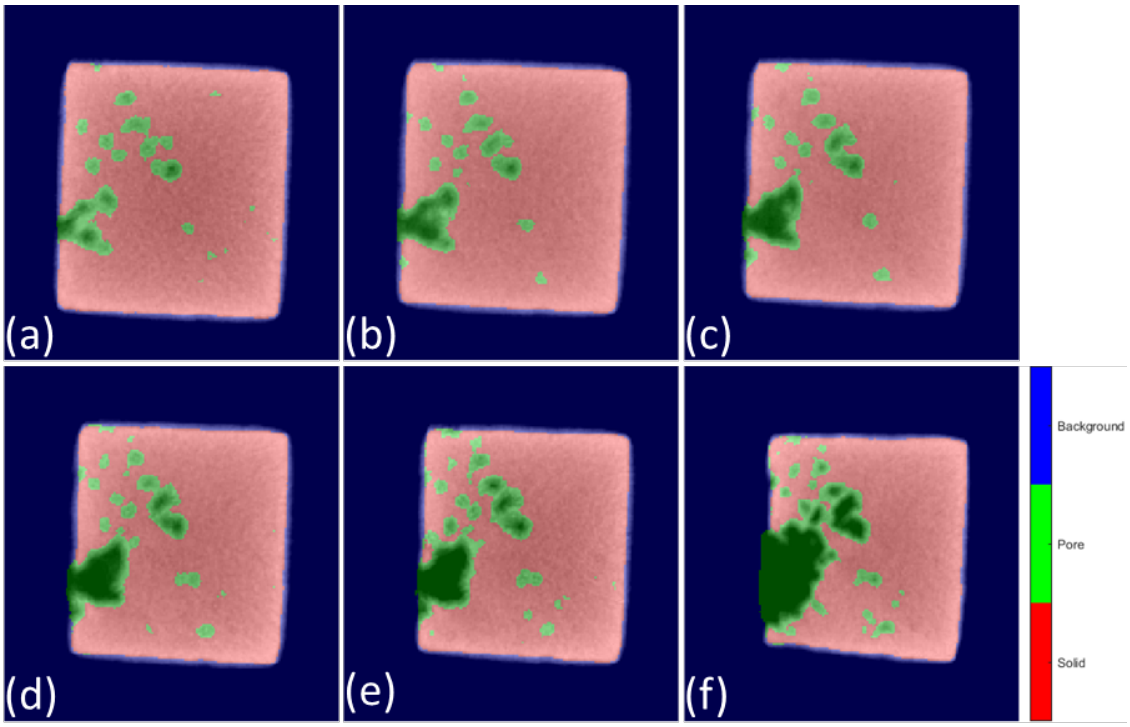

Supplementary Figure 22. Morphological evolution in Sample 3. Horizontal cross-sections at global strains: (a) 5.4640%, (b) 8.2976%, (c) 11.9746%, (d) 15.2186%, (e) 18.2241%, and (f) 21.1419%.

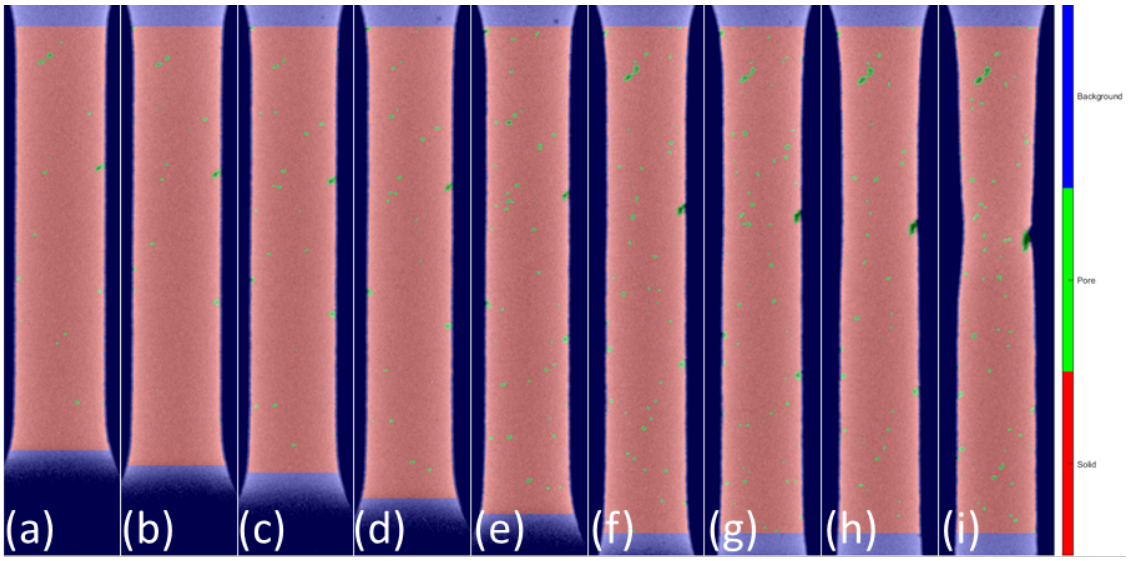

Supplementary Figure 23. Morphological evolution in Sample 4. Vertical cross-sections at global strains: (a) 7.5046%, (b) 10.6992%, (c) 13.9121%, (d) 16.8433%, (e) 19.7903%, (f) 25.5049%, (g) 27.7057%, (h) 30.5934%, and (i) 33.6317%.

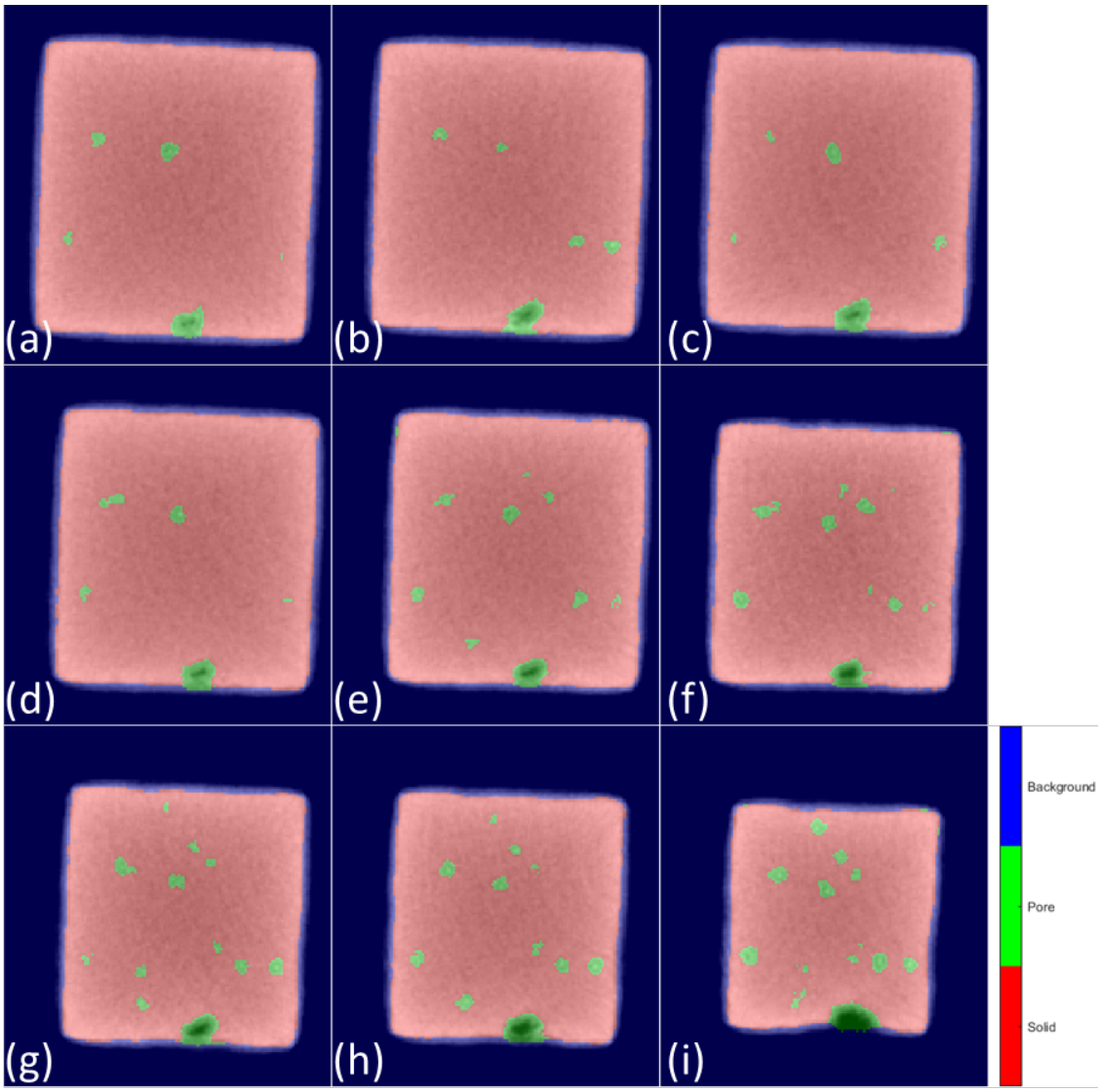

Supplementary Figure 24. Morphological evolution in Sample 4. Horizontal cross-sections at global strains: (a) 7.5046%, (b) 10.6992%, (c) 13.9121%, (d) 16.8433%, (e) 19.7903%, (f) 25.5049%, (g) 27.7057%, (h) 30.5934%, and (i) 33.6317%.

A.4 Identifying Tracked Porosity

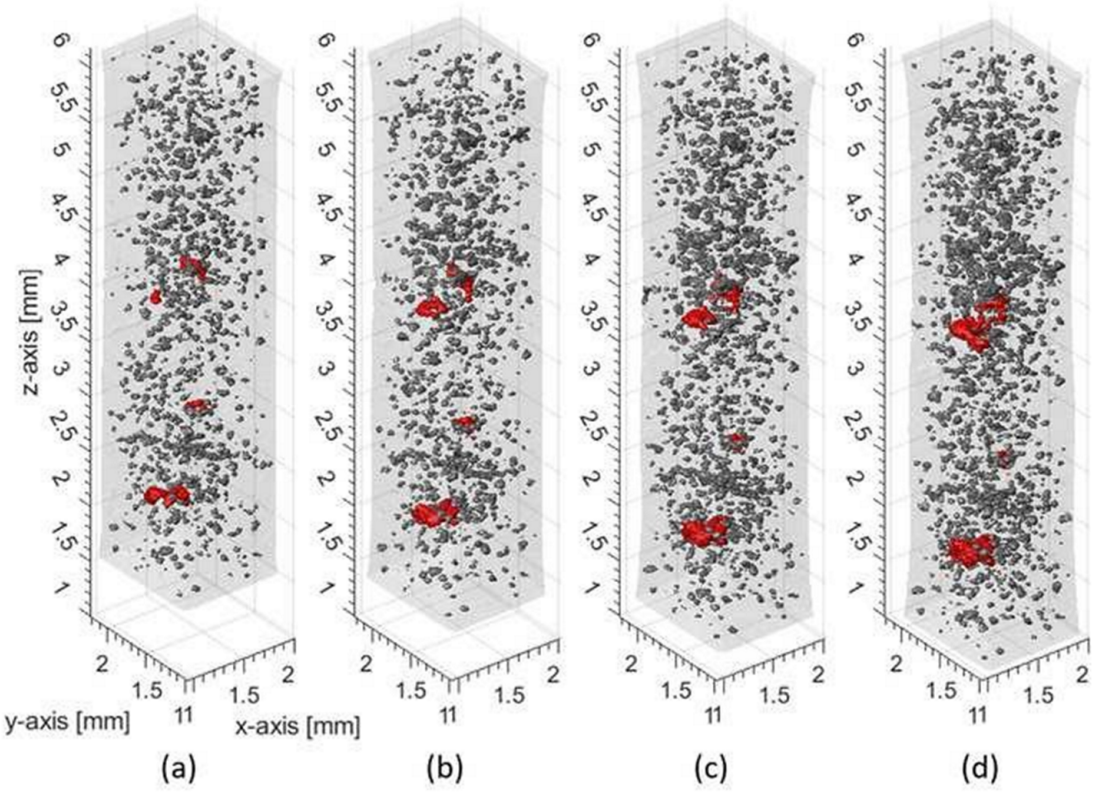

Supplementary Figure 25. Defect Tracking in Sample 1 at global strains: (a) 0.5643%, (b) 3.7354%, (c) 6.9734, (d) 10.3672.

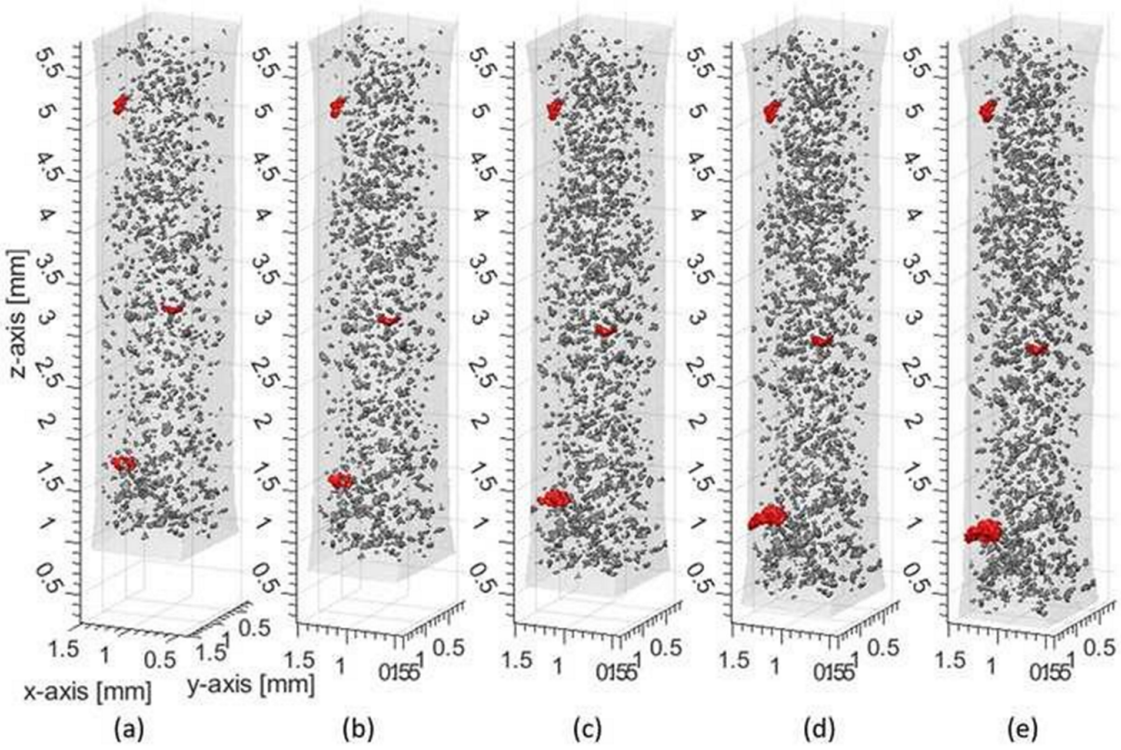

Supplementary Figure 26. Defect tracking in Sample 2 at global strains: (a) 1.8721%, (b) 5.2516%, (c) 8.2976%, (d) 11.9025%, (e) 15.0341%.

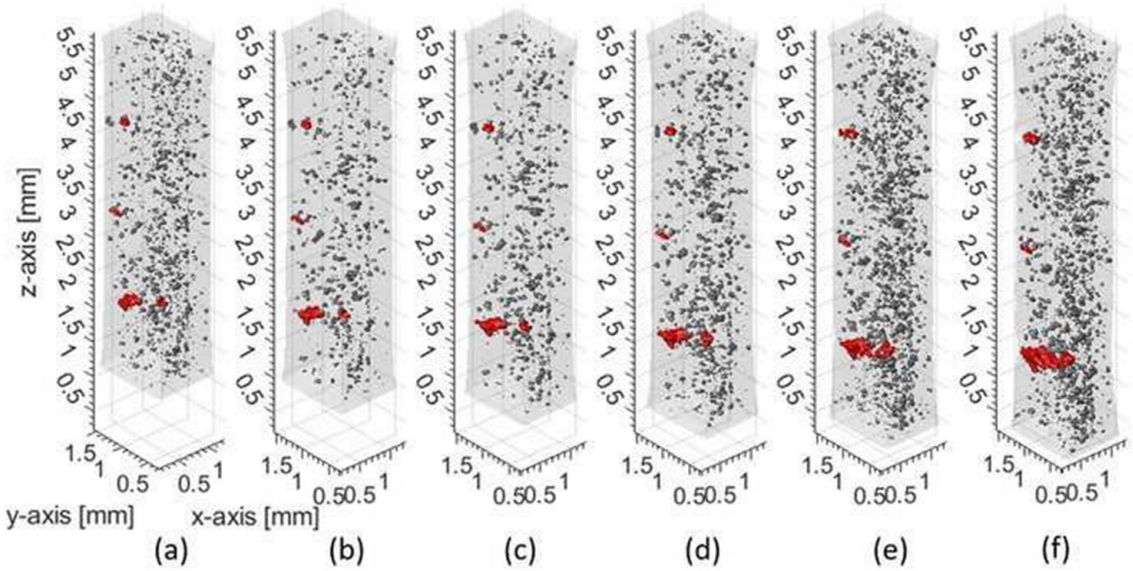

Supplementary Figure 27. Defect tracking in Sample 3 at global strains: (a) 5.4640%, (b) 8.2976%, (c) 11.9746%, (d) 15.2186%, (e) 18.2241%, and (f) 21.1419%.

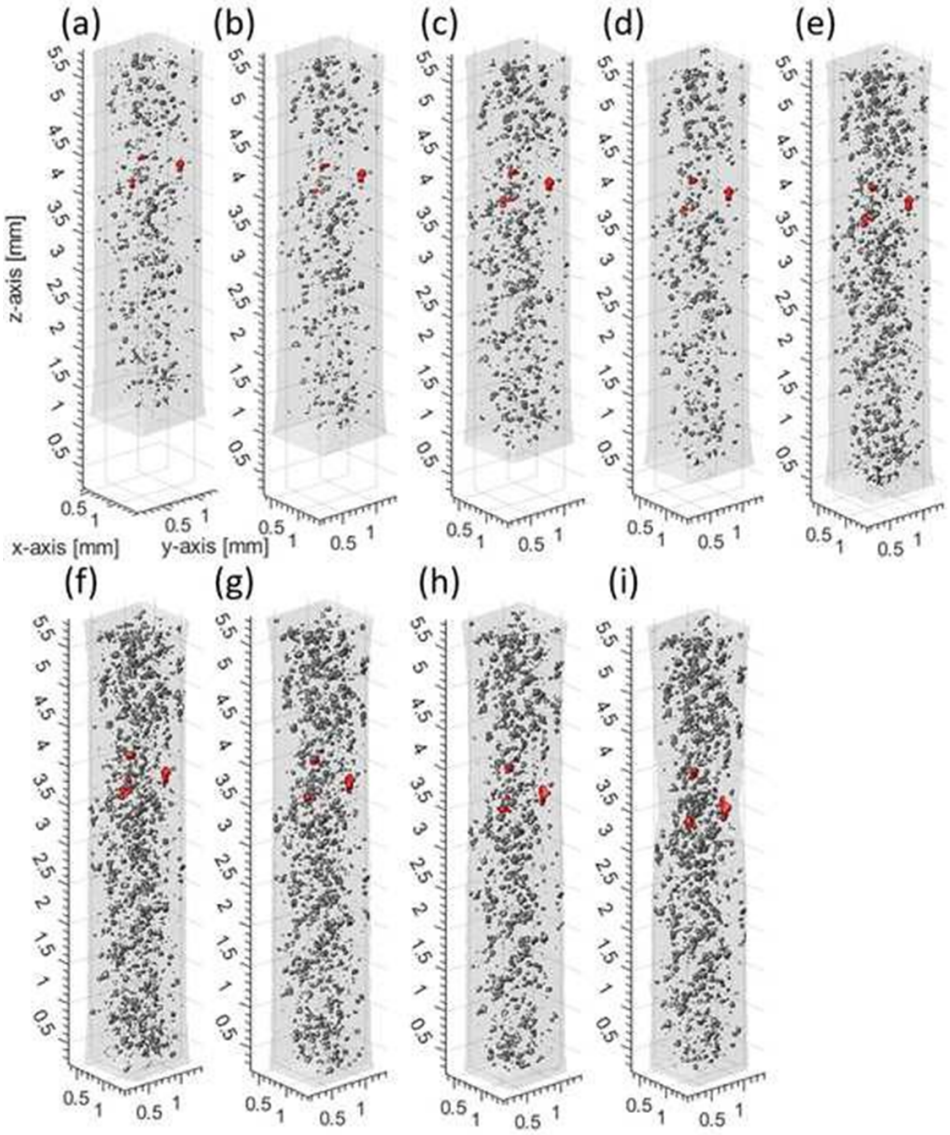

Supplementary Figure 28. Defect tracking in Sample 4 at global strains: (a) 7.5046%, (b) 10.6992%, (c) 13.9121%, (d) 16.8433%, (e) 19.7903%, (f) 25.5049%, (g) 27.7057%, (h) 30.5934%, and (i) 33.6317%.

A.5 Machine Learning Regression

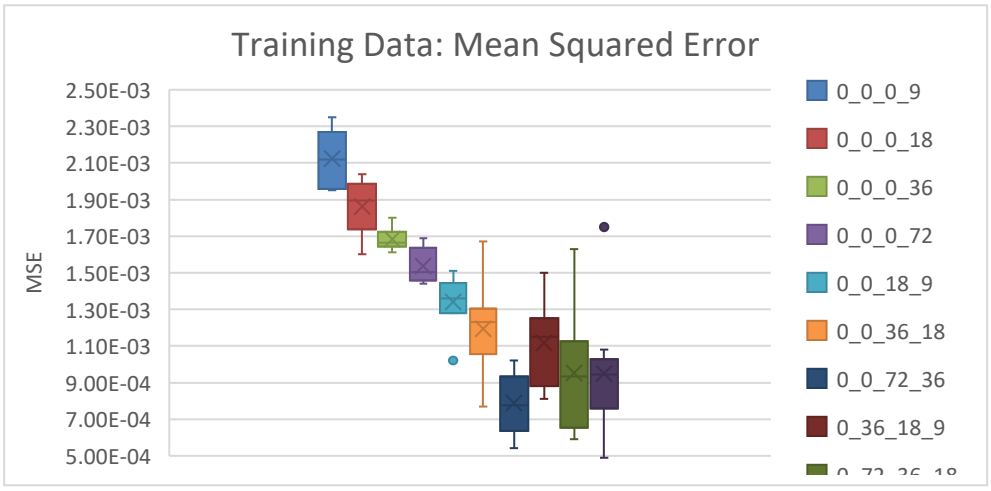

Supplementary Figure 29. Artificial neural network performance, mean squared error: training data.

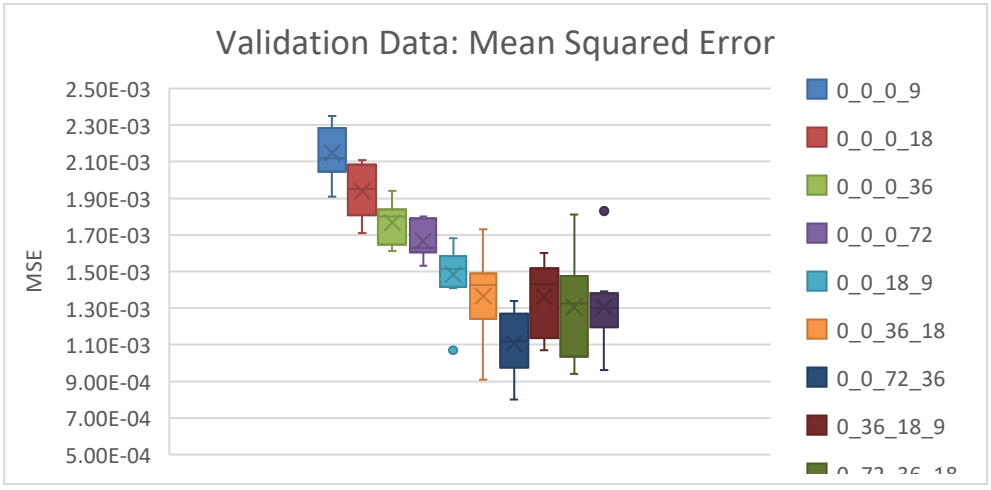

Supplementary Figure 30. Artificial neural network performance, mean squared error: validation data.

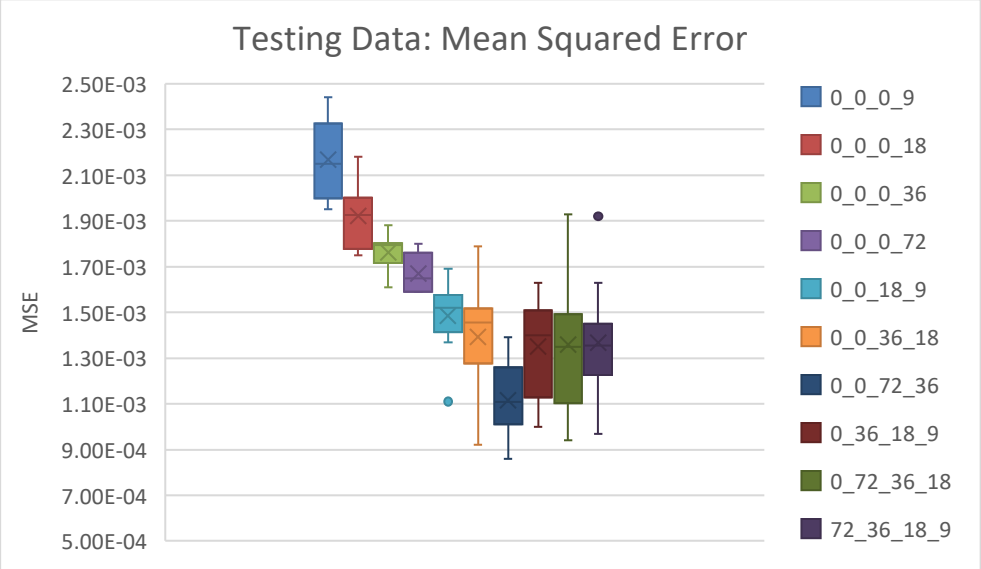

Supplementary Figure 31. Artificial neural network performance, mean squared error: testing data.

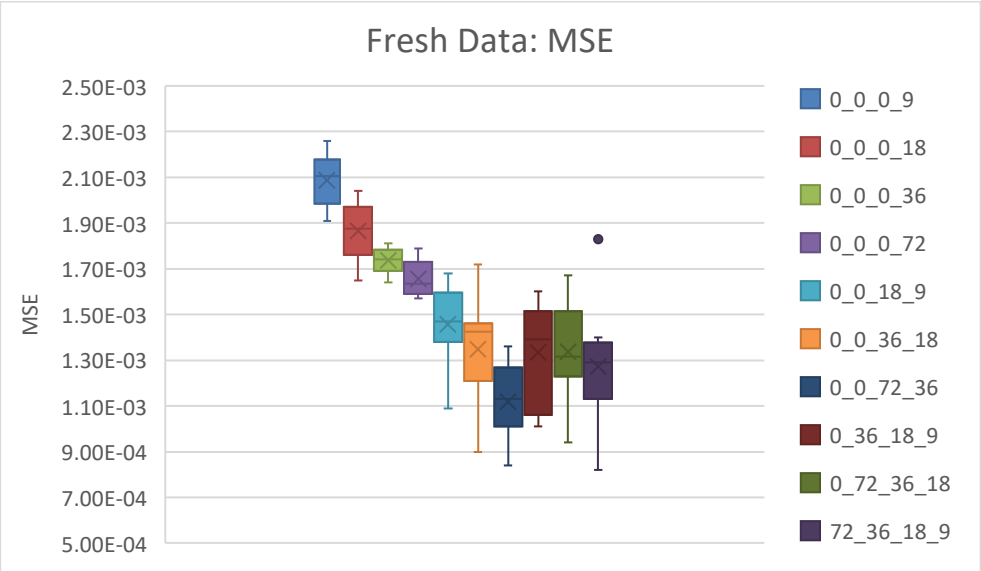

Supplementary Figure 32. Artificial neural network performance, mean squared error: fresh data.

Supplementary Figure 33. Artificial neural network performance, regression value: training data.

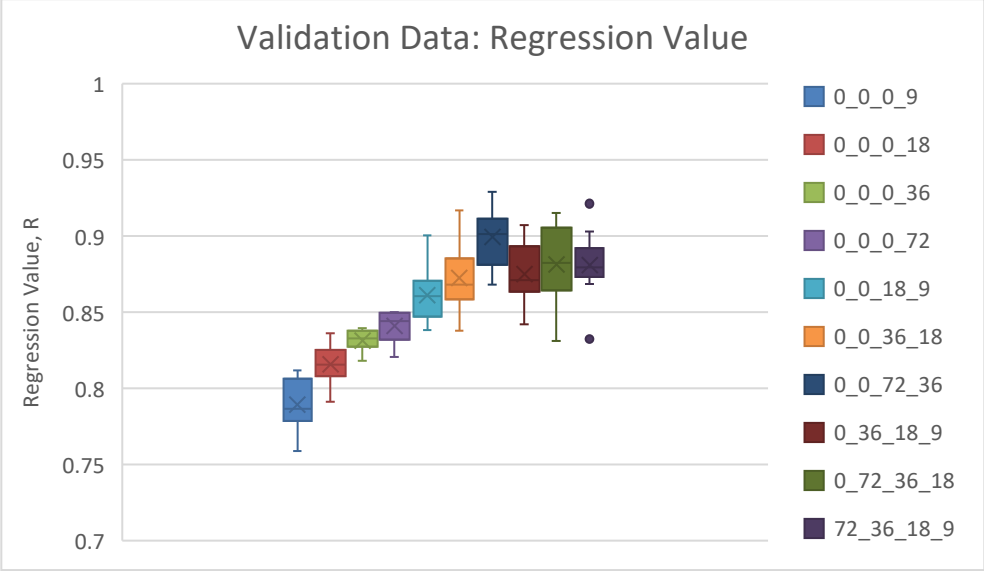

Supplementary Figure 34. Artificial neural network performance, regression value: validation data.

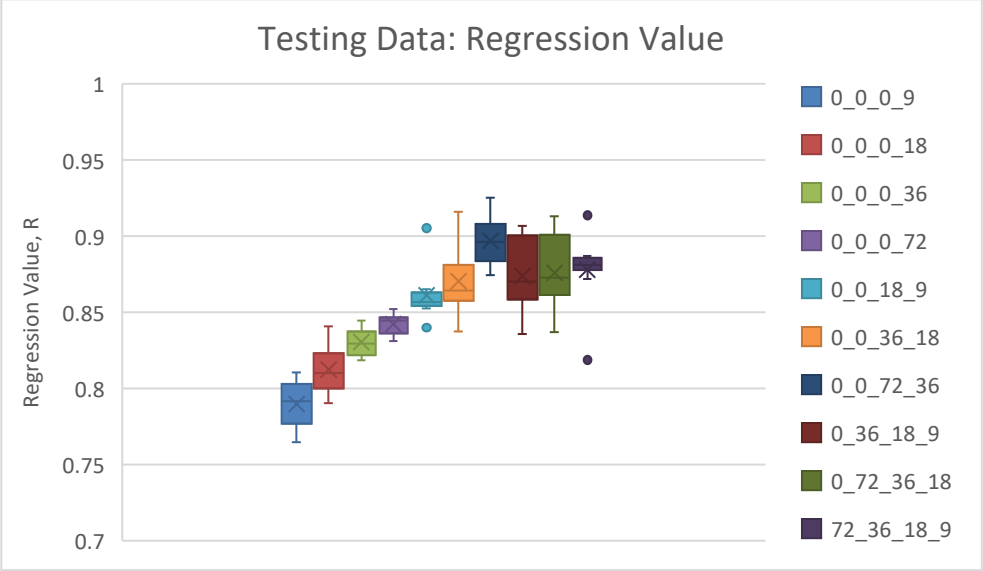

Supplementary Figure 35. Artificial neural network performance, regression value: testing data.

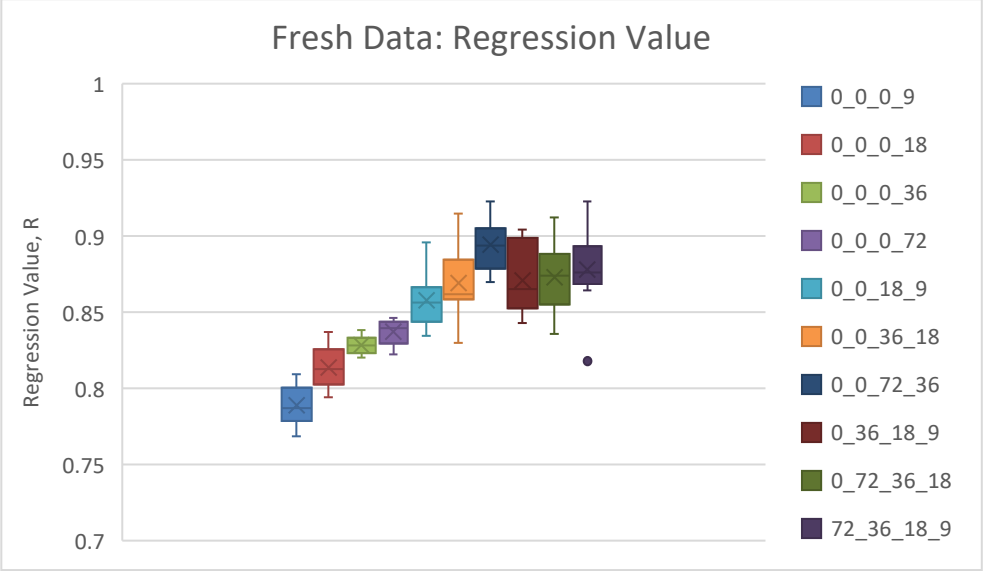

Supplementary Figure 36. Artificial neural network performance, regression value: fresh data.

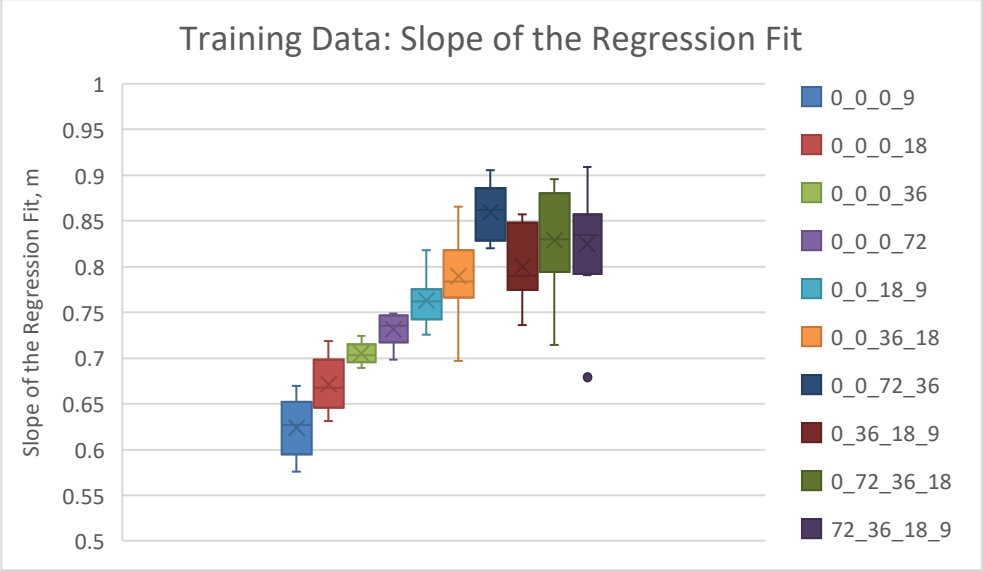

Supplementary Figure 37. Artificial neural network performance, slope of regression fit: training data.

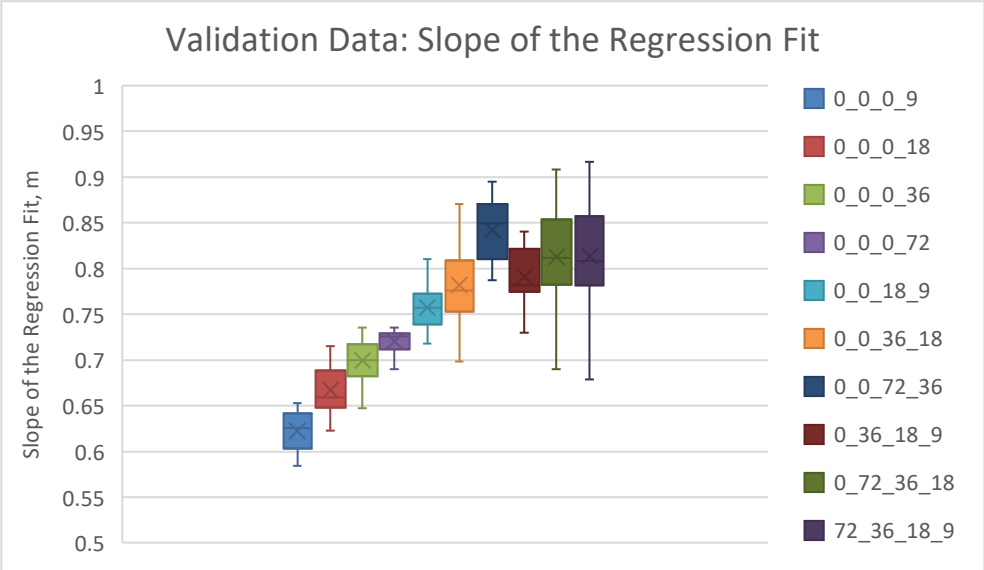

Supplementary Figure 38. Artificial neural network performance, slope of regression fit: validation data.

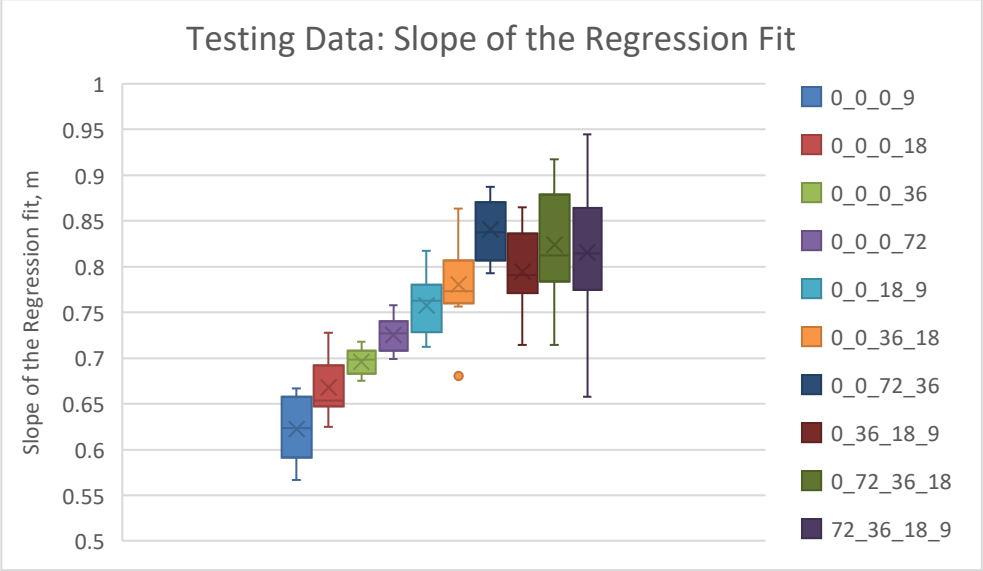

Supplementary Figure 39. Artificial neural network performance, slope of regression fit: testing data.

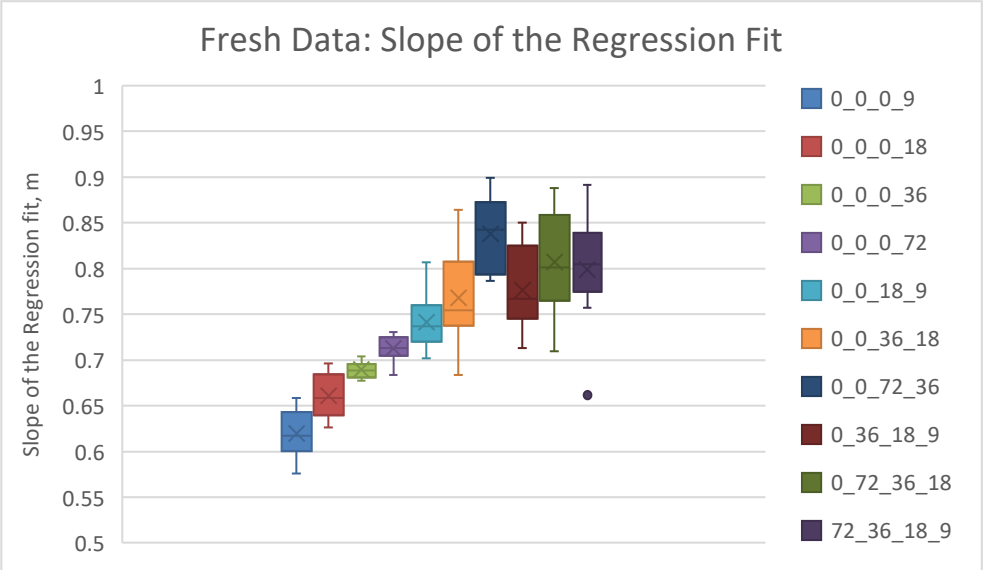

Supplementary Figure 40. Artificial neural network performance, slope of regression fit: fresh data.

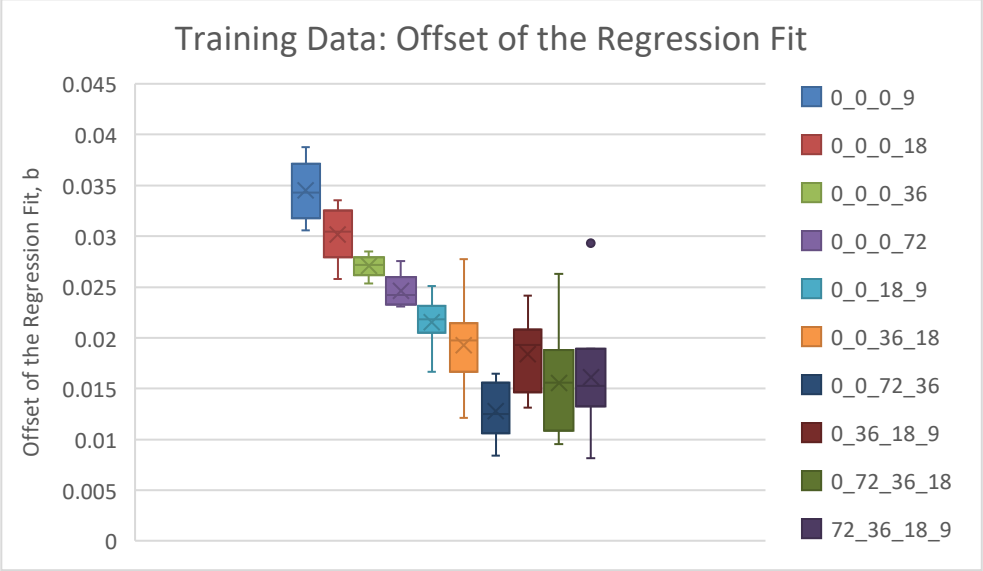

Supplementary Figure 41. Artificial neural network performance, offset of regression fit: training data.

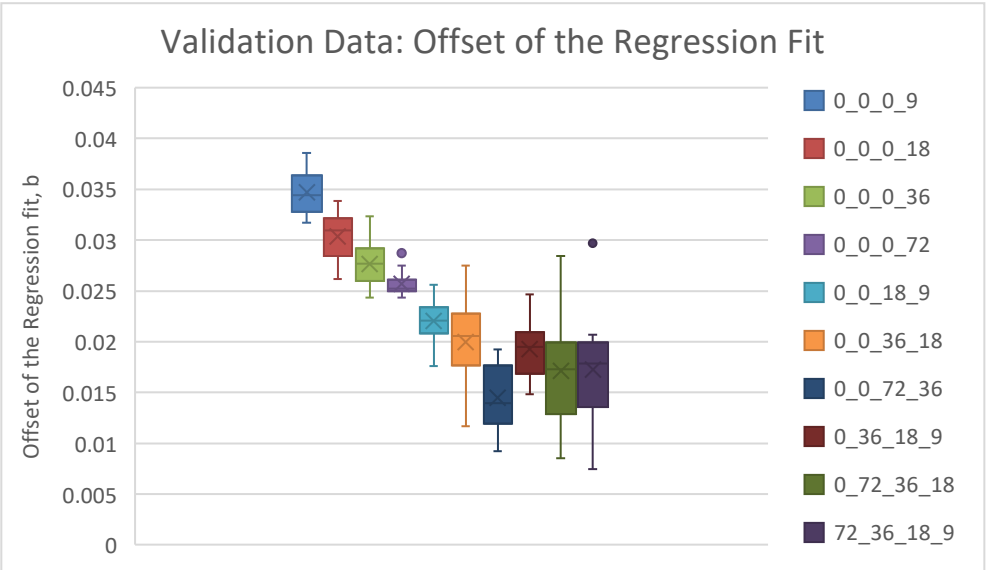

Supplementary Figure 42. Artificial neural network performance, offset of regression fit: validation data.

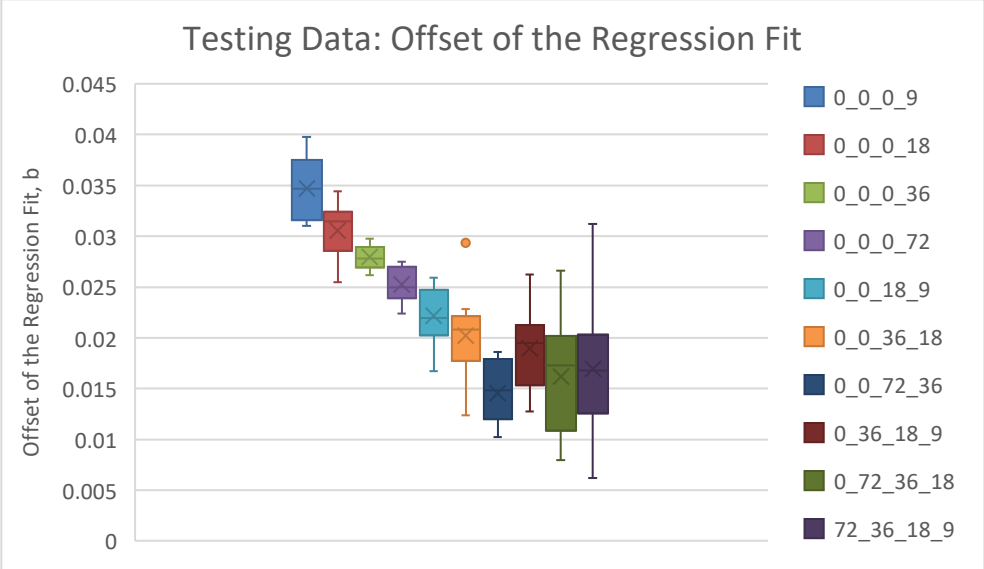

Supplementary Figure 43. Artificial neural network performance, offset of regression fit: testing data.

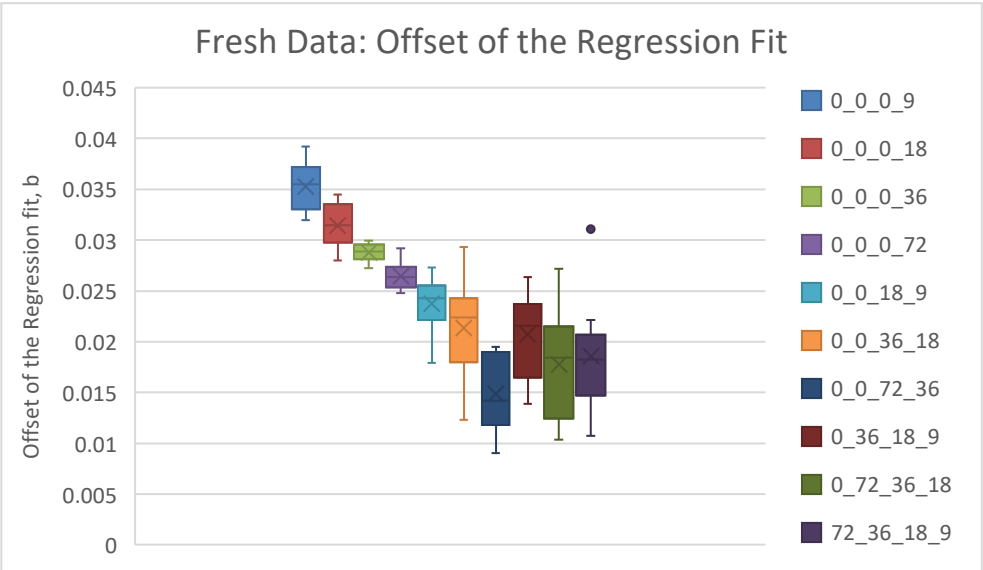

Supplementary Figure 44. Artificial neural network performance, offset of regression fit: fresh data.

APPENDIX B. SUPPLEMENTARY TABLES

B.1 Extended Feature Correlation Table

Supplementary Table 1. Correlation of distance from the external surface with local axial strain.

Sample	Global Strain	Min External Distance	Average External Distance	Max External Distance	Min Inverse External Distance	Average Inverse External Distance	Max Inverse External Distance
1	0.564331	-1.89E-01	1.31E-01	1.35E-01	-1.55E-01	-1.57E-01	-1.57E-01
	3.73549	-2.69E-01	1.17E-01	1.21E-01	-1.45E-01	-1.46E-01	-1.45E-01
	6.973407	-2.59E-01	1.33E-01	1.36E-01	-1.64E-01	-1.64E-01	-1.62E-01
	10.36721	-2.54E-01	1.24E-01	1.26E-01	-1.57E-01	-1.56E-01	-1.53E-01
2	1.87214	-1.47E-01	-5.96E-02	-5.26E-02	2.68E-02	1.65E-02	2.07E-02
	5.251557	-1.81E-01	-3.30E-02	-2.89E-02	5.03E-02	3.97E-02	3.86E-02
	8.297619	-1.88E-01	-4.33E-02	-4.00E-02	7.25E-02	6.21E-02	6.01E-02
	11.90252	-1.95E-01	-3.23E-02	-2.91E-02	6.87E-02	5.78E-02	5.54E-02
	15.03405	-1.97E-01	-5.73E-02	-5.42E-02	9.15E-02	8.15E-02	7.95E-02
3	5.464012	-1.92E-01	-1.49E-01	-1.51E-01	1.91E-01	1.87E-01	1.83E-01
	8.772282	-2.26E-01	-1.64E-01	-1.66E-01	2.05E-01	2.01E-01	1.98E-01
	11.97461	-2.36E-01	-1.90E-01	-1.92E-01	2.26E-01	2.22E-01	2.19E-01
	15.21862	-2.43E-01	-1.92E-01	-1.93E-01	2.26E-01	2.21E-01	2.18E-01
	18.22408	-2.43E-01	-1.96E-01	-1.97E-01	2.27E-01	2.22E-01	2.19E-01
	21.14185	-2.45E-01	-1.44E-01	-1.43E-01	1.68E-01	1.62E-01	1.60E-01
4	7.504601	-3.56E-02	-5.26E-01	-5.33E-01	2.72E-01	4.81E-01	5.29E-01
	10.69917	-4.43E-02	-5.50E-01	-5.58E-01	2.62E-01	4.88E-01	5.43E-01
	13.91213	-4.93E-02	-5.68E-01	-5.74E-01	2.43E-01	4.81E-01	5.42E-01
	16.84327	-5.82E-02	-5.70E-01	-5.76E-01	2.24E-01	4.63E-01	5.26E-01
	19.7903	-6.35E-02	-5.63E-01	-5.68E-01	2.03E-01	4.43E-01	5.07E-01
	25.5049	-6.90E-02	-5.72E-01	-5.77E-01	2.84E-01	4.93E-01	5.43E-01
	27.7057	-7.50E-02	-5.54E-01	-5.58E-01	2.52E-01	4.60E-01	5.12E-01
	30.59347	-7.89E-02	-5.17E-01	-5.21E-01	2.07E-01	4.07E-01	4.60E-01
	33.63166	-8.54E-02	-4.42E-01	-4.45E-01	1.62E-01	3.38E-01	3.86E-01

Supplementary Table 2. Correlation of distance from internal surfaces with local axial strain.

Sample	Global Strain	Min Internal Distance	Average Internal Distance	Max Internal Distance	Min Inverse Internal Distance	Average Inverse Internal Distance	Max Inverse Internal Distance
1	0.564331	-2.71E-01	-2.80E-01	-2.78E-01	1.55E-02	2.94E-01	3.01E-01
	3.73549	-3.20E-01	-3.38E-01	-3.45E-01	2.56E-02	3.64E-01	3.88E-01
	6.973407	-3.10E-01	-3.26E-01	-3.33E-01	2.48E-02	3.54E-01	3.78E-01
	10.36721	-3.13E-01	-3.29E-01	-3.36E-01	2.40E-02	3.56E-01	3.81E-01
2	1.87214	-2.36E-01	-2.39E-01	-2.34E-01	1.94E-01	2.39E-01	2.46E-01
	5.251557	-3.08E-01	-3.18E-01	-3.17E-01	2.49E-01	3.08E-01	3.28E-01
	8.297619	-3.29E-01	-3.43E-01	-3.43E-01	2.67E-01	3.31E-01	3.55E-01
	11.90252	-3.43E-01	-3.57E-01	-3.58E-01	2.80E-01	3.47E-01	3.72E-01
	15.03405	-3.39E-01	-3.55E-01	-3.59E-01	2.79E-01	3.48E-01	3.76E-01
3	5.464012	-1.92E-01	-2.13E-01	-2.27E-01	1.87E-01	2.27E-01	2.60E-01
	8.772282	-2.15E-01	-2.37E-01	-2.51E-01	2.03E-01	2.48E-01	2.86E-01
	11.97461	-2.35E-01	-2.58E-01	-2.73E-01	2.20E-01	2.70E-01	3.10E-01
	15.21862	-2.51E-01	-2.72E-01	-2.87E-01	2.34E-01	2.87E-01	3.26E-01
	18.22408	-2.61E-01	-2.82E-01	-2.96E-01	2.41E-01	2.97E-01	3.36E-01
	21.14185	-2.63E-01	-2.81E-01	-2.92E-01	2.54E-01	3.05E-01	3.39E-01
4	7.504601	-2.42E-01	-2.87E-01	-3.26E-01	9.82E-02	1.94E-01	2.92E-01
	10.69917	-2.61E-01	-3.09E-01	-3.50E-01	1.04E-01	2.07E-01	3.08E-01
	13.91213	-2.72E-01	-3.19E-01	-3.60E-01	1.07E-01	2.11E-01	3.11E-01
	16.84327	-2.86E-01	-3.29E-01	-3.67E-01	1.18E-01	2.19E-01	3.15E-01
	19.7903	-2.90E-01	-3.31E-01	-3.66E-01	1.17E-01	2.18E-01	3.09E-01
	25.5049	-3.10E-01	-3.51E-01	-3.87E-01	1.54E-01	2.52E-01	3.46E-01
	27.7057	-3.13E-01	-3.50E-01	-3.84E-01	1.53E-01	2.49E-01	3.38E-01
	30.59347	-3.01E-01	-3.34E-01	-3.63E-01	1.44E-01	2.34E-01	3.13E-01
	33.63166	-2.78E-01	-3.04E-01	-3.27E-01	1.36E-01	2.13E-01	2.79E-01

Supplementary Table 3. Correlation of pore diameter and pore volume with local axial strain.

Sample	Global Strain	Min Pore Diameter	Average Pore Diameter	Max Pore Diameter	Min Pore Volume	Average Pore Volume	Max Pore Volume
1	0.564331	3.24E-01	4.00E-01	3.92E-01	3.05E-01	3.91E-01	3.81E-01
	3.73549	4.23E-01	5.53E-01	5.50E-01	4.37E-01	6.07E-01	5.99E-01
	6.973407	4.20E-01	5.66E-01	5.74E-01	4.51E-01	6.50E-01	6.57E-01
	10.36721	4.20E-01	5.66E-01	5.72E-01	4.45E-01	6.37E-01	6.40E-01
2	1.87214	1.88E-01	2.63E-01	2.65E-01	2.56E-01	3.26E-01	3.19E-01
	5.251557	2.31E-01	3.23E-01	3.19E-01	2.68E-01	3.52E-01	3.35E-01
	8.297619	2.53E-01	3.54E-01	3.46E-01	2.83E-01	3.76E-01	3.54E-01
	11.90252	2.72E-01	3.83E-01	3.74E-01	2.98E-01	4.01E-01	3.76E-01
	15.03405	2.99E-01	4.16E-01	4.05E-01	3.21E-01	4.32E-01	4.06E-01
3	5.464012	5.07E-01	5.74E-01	5.61E-01	6.52E-01	7.38E-01	7.08E-01
	8.772282	5.22E-01	5.88E-01	5.72E-01	6.66E-01	7.48E-01	7.14E-01
	11.97461	5.21E-01	5.90E-01	5.75E-01	6.56E-01	7.39E-01	7.06E-01
	15.21862	5.11E-01	5.84E-01	5.71E-01	6.33E-01	7.18E-01	6.89E-01
	18.22408	4.99E-01	5.79E-01	5.70E-01	6.14E-01	7.02E-01	6.75E-01
	21.14185	4.79E-01	5.70E-01	5.76E-01	5.87E-01	6.91E-01	6.87E-01
4	7.504601	2.22E-01	2.22E-01	2.07E-01	2.40E-01	2.38E-01	2.15E-01
	10.69917	2.29E-01	2.24E-01	2.00E-01	2.51E-01	2.44E-01	2.13E-01
	13.91213	2.34E-01	2.35E-01	2.16E-01	2.57E-01	2.57E-01	2.30E-01
	16.84327	2.48E-01	2.51E-01	2.32E-01	2.75E-01	2.76E-01	2.49E-01
	19.7903	2.60E-01	2.66E-01	2.49E-01	2.92E-01	2.97E-01	2.73E-01
	25.5049	2.59E-01	2.62E-01	2.41E-01	3.02E-01	3.10E-01	2.85E-01
	27.7057	2.75E-01	2.83E-01	2.63E-01	3.25E-01	3.39E-01	3.16E-01
	30.59347	2.84E-01	2.97E-01	2.80E-01	3.43E-01	3.66E-01	3.48E-01
	33.63166	3.15E-01	3.39E-01	3.26E-01	3.98E-01	4.36E-01	4.26E-01

Supplementary Table 4. Correlation of pore gap and pore sphericity with local axial strain.

Sample	Global Strain	Min Pore Gap	Average Pore Gap	Max Pore Gap	Min Pore Sphericity	Average Pore Sphericity	Max Pore Sphericity
1	0.564331	-3.57E-01	-3.92E-01	-3.83E-01	-2.56E-02	-1.00E-02	1.40E-02
	3.73549	-4.71E-01	-5.14E-01	-5.03E-01	-6.30E-02	-4.63E-02	-2.68E-02
	6.973407	-4.85E-01	-5.27E-01	-5.16E-01	-7.41E-02	-5.51E-02	-3.46E-02
	10.36721	-4.93E-01	-5.30E-01	-5.17E-01	-9.04E-02	-7.24E-02	-5.11E-02
2	1.87214	-2.07E-01	-2.46E-01	-2.49E-01	-5.75E-04	1.02E-02	1.10E-02
	5.251557	-2.50E-01	-2.98E-01	-3.09E-01	-4.16E-03	1.29E-02	1.83E-02
	8.297619	-2.66E-01	-3.20E-01	-3.35E-01	-5.89E-03	2.00E-04	2.31E-03
	11.90252	-2.92E-01	-3.45E-01	-3.57E-01	-1.53E-02	-1.40E-02	-1.25E-02
	15.03405	-3.09E-01	-3.58E-01	-3.64E-01	-2.89E-02	-3.34E-02	-3.41E-02
3	5.464012	-2.46E-01	-2.73E-01	-2.72E-01	2.12E-02	1.96E-02	7.80E-03
	8.772282	-2.49E-01	-2.80E-01	-2.83E-01	2.96E-02	2.59E-02	1.21E-02
	11.97461	-2.58E-01	-2.90E-01	-2.93E-01	2.92E-02	2.19E-02	6.42E-03
	15.21862	-2.71E-01	-3.04E-01	-3.07E-01	2.91E-02	2.26E-02	7.80E-03
	18.22408	-2.85E-01	-3.17E-01	-3.16E-01	2.53E-02	2.05E-02	8.90E-03
	21.14185	-3.05E-01	-3.35E-01	-3.30E-01	1.74E-03	5.45E-03	6.18E-03
4	7.504601	9.15E-02	6.63E-02	3.61E-02	5.17E-02	2.55E-02	-1.09E-02
	10.69917	1.13E-01	8.16E-02	3.97E-02	5.78E-02	2.16E-02	-2.06E-02
	13.91213	1.04E-01	7.36E-02	3.19E-02	4.54E-02	1.21E-02	-2.52E-02
	16.84327	9.98E-02	6.89E-02	2.80E-02	4.17E-02	1.12E-02	-2.18E-02
	19.7903	8.88E-02	5.87E-02	2.01E-02	4.13E-02	1.40E-02	-1.48E-02
	25.5049	9.76E-02	6.35E-02	2.11E-02	5.32E-02	1.33E-02	-2.78E-02
	27.7057	9.16E-02	6.05E-02	1.94E-02	4.69E-02	1.16E-02	-2.41E-02
	30.59347	9.40E-02	6.83E-02	3.20E-02	4.68E-02	1.37E-02	-1.96E-02
	33.63166	9.73E-02	7.72E-02	4.67E-02	4.94E-02	1.98E-02	-9.07E-03

Supplementary Table 5. Correlation of pore compactness and pore tortuosity with local axial strain.

Sample	Global Strain	Min Pore Compactness	Average Pore Compactness	Max Pore Compactness	Min Pore Tortuosity	Average Pore Tortuosity	Max Pore Tortuosity
1	0.564331	-2.08E-01	-2.00E-01	-1.55E-01	2.71E-01	3.26E-01	3.17E-01
	3.73549	-2.89E-01	-2.77E-01	-2.22E-01	3.59E-01	4.57E-01	4.55E-01
	6.973407	-2.96E-01	-2.80E-01	-2.22E-01	3.57E-01	4.69E-01	4.77E-01
	10.36721	-3.00E-01	-2.84E-01	-2.26E-01	3.57E-01	4.75E-01	4.87E-01
2	1.87214	-1.51E-01	-1.33E-01	-8.21E-02	1.36E-01	2.00E-01	2.04E-01
	5.251557	-2.18E-01	-2.07E-01	-1.50E-01	1.93E-01	2.77E-01	2.78E-01
	8.297619	-2.33E-01	-2.26E-01	-1.66E-01	2.17E-01	3.10E-01	3.08E-01
	11.90252	-2.47E-01	-2.38E-01	-1.72E-01	2.37E-01	3.42E-01	3.41E-01
	15.03405	-2.62E-01	-2.54E-01	-1.88E-01	2.66E-01	3.79E-01	3.76E-01
3	5.464012	-1.41E-01	-1.53E-01	-1.44E-01	3.59E-01	3.98E-01	3.71E-01
	8.772282	-1.45E-01	-1.61E-01	-1.53E-01	3.69E-01	4.06E-01	3.76E-01
	11.97461	-1.49E-01	-1.66E-01	-1.57E-01	3.69E-01	4.09E-01	3.80E-01
	15.21862	-1.53E-01	-1.68E-01	-1.56E-01	3.61E-01	4.06E-01	3.80E-01
	18.22408	-1.58E-01	-1.69E-01	-1.51E-01	3.51E-01	4.03E-01	3.81E-01
	21.14185	-1.73E-01	-1.75E-01	-1.45E-01	3.29E-01	3.95E-01	3.88E-01
4	7.504601	-7.95E-02	-1.01E-01	-1.19E-01	1.70E-01	1.57E-01	1.32E-01
	10.69917	-6.09E-02	-9.29E-02	-1.20E-01	1.70E-01	1.49E-01	1.18E-01
	13.91213	-7.10E-02	-1.01E-01	-1.25E-01	1.71E-01	1.53E-01	1.23E-01
	16.84327	-7.52E-02	-1.03E-01	-1.24E-01	1.72E-01	1.56E-01	1.28E-01
	19.7903	-7.65E-02	-1.05E-01	-1.25E-01	1.70E-01	1.52E-01	1.22E-01
	25.5049	-6.90E-02	-1.06E-01	-1.35E-01	1.80E-01	1.55E-01	1.18E-01
	27.7057	-7.41E-02	-1.10E-01	-1.37E-01	1.77E-01	1.53E-01	1.17E-01
	30.59347	-7.30E-02	-1.09E-01	-1.35E-01	1.69E-01	1.46E-01	1.12E-01
	33.63166	-8.31E-02	-1.17E-01	-1.39E-01	1.80E-01	1.60E-01	1.25E-01

Supplementary Table 6. Correlation of cross-section area relative to the loading direction with local axial strain.

Sample	Global Strain	Min Cross-Section Area	Average Cross-Section Area	Max Cross-Section Area	Min Inverse Cross-Section Area	Average Inverse Cross-Section Area	Max Inverse Cross-Section Area
1	0.564331	-2.90E-01	-2.36E-01	-1.26E-01	2.92E-01	2.40E-01	1.25E-01
	3.73549	-4.54E-01	-3.79E-01	-2.32E-01	4.57E-01	3.85E-01	2.34E-01
	6.973407	-4.88E-01	-4.14E-01	-2.63E-01	4.92E-01	4.19E-01	2.65E-01
	10.36721	-5.26E-01	-4.48E-01	-2.88E-01	5.30E-01	4.53E-01	2.90E-01
2	1.87214	-1.50E-01	-1.51E-01	-1.48E-01	1.50E-01	1.51E-01	1.48E-01
	5.251557	-2.66E-01	-2.81E-01	-2.90E-01	2.64E-01	2.79E-01	2.89E-01
	8.297619	-3.21E-01	-3.38E-01	-3.47E-01	3.19E-01	3.35E-01	3.45E-01
	11.90252	-3.44E-01	-3.55E-01	-3.60E-01	3.42E-01	3.53E-01	3.58E-01
	15.03405	-3.39E-01	-3.42E-01	-3.39E-01	3.38E-01	3.41E-01	3.38E-01
3	5.464012	-2.32E-01	-1.41E-01	-3.79E-02	2.36E-01	1.43E-01	3.70E-02
	8.772282	-2.57E-01	-1.60E-01	-4.58E-02	2.62E-01	1.62E-01	4.45E-02
	11.97461	-2.75E-01	-1.73E-01	-5.26E-02	2.80E-01	1.76E-01	5.13E-02
	15.21862	-2.96E-01	-1.88E-01	-5.82E-02	3.02E-01	1.92E-01	5.71E-02
	18.22408	-3.01E-01	-1.90E-01	-5.59E-02	3.07E-01	1.94E-01	5.49E-02
	21.14185	-3.09E-01	-1.80E-01	-2.11E-02	3.17E-01	1.85E-01	2.01E-02
4	7.504601	-3.33E-02	-3.26E-02	-2.98E-02	4.09E-02	4.09E-02	3.86E-02
	10.69917	-5.55E-02	-5.44E-02	-5.13E-02	6.33E-02	6.30E-02	6.05E-02
	13.91213	-9.04E-02	-8.94E-02	-8.57E-02	9.79E-02	9.78E-02	9.47E-02
	16.84327	-1.18E-01	-1.16E-01	-1.10E-01	1.25E-01	1.24E-01	1.19E-01
	19.7903	-1.55E-01	-1.52E-01	-1.45E-01	1.63E-01	1.60E-01	1.54E-01
	25.5049	-9.98E-03	-1.80E-03	8.14E-03	2.04E-02	1.26E-02	2.77E-03
	27.7057	-6.26E-02	-5.36E-02	-4.27E-02	7.34E-02	6.48E-02	5.39E-02
	30.59347	-1.28E-01	-1.18E-01	-1.06E-01	1.39E-01	1.30E-01	1.18E-01
	33.63166	-1.64E-01	-1.54E-01	-1.41E-01	1.76E-01	1.67E-01	1.53E-01

Supplementary Table 7. Correlation of wall thickness with local axial strain.

Sample	Global Strain	Min Wall Thickness	Average Wall Thickness	Max Wall Thickness	Min Inverse Wall Thickness	Average Inverse Wall Thickness	Max Inverse Wall Thickness
1	0.564331	-2.92E-01	-2.66E-01	-2.15E-01	2.58E-01	2.66E-01	2.07E-01
	3.73549	-3.60E-01	-3.38E-01	-2.77E-01	3.24E-01	3.59E-01	2.84E-01
	6.973407	-3.47E-01	-3.29E-01	-2.71E-01	3.18E-01	3.56E-01	2.80E-01
	10.36721	-3.47E-01	-3.28E-01	-2.68E-01	3.14E-01	3.56E-01	2.78E-01
2	1.87214	-2.64E-01	-2.40E-01	-1.79E-01	2.44E-01	2.43E-01	1.73E-01
	5.251557	-3.60E-01	-3.55E-01	-2.96E-01	3.29E-01	3.58E-01	2.93E-01
	8.297619	-3.86E-01	-3.85E-01	-3.24E-01	3.56E-01	3.92E-01	3.27E-01
	11.90252	-3.98E-01	-3.96E-01	-3.34E-01	3.71E-01	4.09E-01	3.43E-01
	15.03405	-3.98E-01	-4.01E-01	-3.43E-01	3.75E-01	4.19E-01	3.59E-01
3	5.464012	-2.37E-01	-2.22E-01	-1.90E-01	2.16E-01	2.46E-01	1.94E-01
	8.772282	-2.63E-01	-2.48E-01	-2.11E-01	2.37E-01	2.73E-01	2.16E-01
	11.97461	-2.85E-01	-2.70E-01	-2.31E-01	2.56E-01	3.01E-01	2.42E-01
	15.21862	-3.00E-01	-2.84E-01	-2.44E-01	2.69E-01	3.20E-01	2.59E-01
	18.22408	-3.10E-01	-2.96E-01	-2.56E-01	2.76E-01	3.34E-01	2.73E-01
	21.14185	-3.11E-01	-3.01E-01	-2.65E-01	2.82E-01	3.46E-01	2.89E-01
4	7.504601	-3.39E-01	-3.28E-01	-2.81E-01	1.91E-01	1.93E-01	1.80E-01
	10.69917	-3.65E-01	-3.53E-01	-3.00E-01	1.90E-01	1.92E-01	1.80E-01
	13.91213	-3.78E-01	-3.70E-01	-3.21E-01	1.77E-01	1.86E-01	1.82E-01
	16.84327	-3.85E-01	-3.80E-01	-3.33E-01	1.61E-01	1.80E-01	1.83E-01
	19.7903	-3.82E-01	-3.79E-01	-3.35E-01	1.45E-01	1.67E-01	1.77E-01
	25.5049	-4.28E-01	-4.30E-01	-3.86E-01	2.24E-01	2.52E-01	2.41E-01
	27.7057	-4.17E-01	-4.22E-01	-3.80E-01	1.99E-01	2.34E-01	2.29E-01
	30.59347	-3.90E-01	-3.99E-01	-3.65E-01	1.63E-01	2.05E-01	2.10E-01
	33.63166	-3.46E-01	-3.61E-01	-3.40E-01	1.30E-01	1.73E-01	1.86E-01

Supplementary Table 8. Correlation of non-local field and pore volume fraction with local axial strain.

Sample	Global Strain	Min Non-local Field	Average Non-local Field	Max Non-local Field	Pore Volume Fraction
1	0.564331	4.61E-01	4.62E-01	4.52E-01	1.89E-01
	3.73549	6.23E-01	6.18E-01	6.03E-01	2.69E-01
	6.973407	6.48E-01	6.39E-01	6.23E-01	2.59E-01
	10.36721	6.52E-01	6.43E-01	6.28E-01	2.54E-01
2	1.87214	3.53E-01	3.64E-01	3.59E-01	1.47E-01
	5.251557	4.39E-01	4.51E-01	4.45E-01	1.81E-01
	8.297619	4.81E-01	4.90E-01	4.82E-01	1.88E-01
	11.90252	5.20E-01	5.27E-01	5.17E-01	1.95E-01
	15.03405	5.49E-01	5.48E-01	5.35E-01	1.97E-01
3	5.464012	6.98E-01	6.49E-01	6.04E-01	1.92E-01
	8.772282	7.13E-01	6.66E-01	6.22E-01	2.26E-01
	11.97461	7.14E-01	6.70E-01	6.27E-01	2.36E-01
	15.21862	7.09E-01	6.69E-01	6.28E-01	2.43E-01
	18.22408	6.98E-01	6.62E-01	6.25E-01	2.43E-01
	21.14185	7.47E-01	7.15E-01	6.79E-01	2.45E-01
4	7.504601	1.26E-01	1.01E-01	7.11E-02	3.56E-02
	10.69917	1.38E-01	1.15E-01	8.66E-02	4.43E-02
	13.91213	1.58E-01	1.36E-01	1.08E-01	4.93E-02
	16.84327	1.90E-01	1.68E-01	1.39E-01	5.82E-02
	19.7903	2.08E-01	1.87E-01	1.59E-01	6.35E-02
	25.5049	2.22E-01	1.95E-01	1.61E-01	6.90E-02
	27.7057	2.49E-01	2.23E-01	1.90E-01	7.50E-02
	30.59347	2.65E-01	2.42E-01	2.11E-01	7.89E-02
	33.63166	2.93E-01	2.67E-01	2.35E-01	8.54E-02

REFERENCES

[1] ASTM International International Committee F42 on Additive Manufacturing Technologies, "ASTM F2792-10 Standard Terminalogy for Additive Manufacturing," *ASTM International,* no. F2792-10, pp. 1-3, 2009.

[2] Y. Huang, M. Leu, J. Maumder and A. Donmez, "Additive Manufacturing: Current State , Future Potential, Gaps and Needs, and Recommendations," *Jounral of Manufacturing Science and Engineering,* vol. 137, no. 014001, pp. 1-10, 2015.

[3] I. Gibson, B. Stucker and D. Rosen, Additive Manufacturing Technologies: Rapid Prototyping to Direct Digital Manufacturing, Springer, Cham, 2014.

[4] T. Wohlers and T. Gornet, "History of Additive Manufacturing," *Wohlers Report,* pp. 1-38, 2016.

[5] J. Bradley, D. Moore, S. Stair, B. Boyce, J. Madison, T. Ivanoff, K. Johnson, J. Ostien, J. Rodelas, B. Salzbrenner, L. Swiler, O. Underwood, D. Saiz, B. Kernan, K. Webb, E. Jost and J. Miers, "The Impact of Critical Defects on Material Performance and Science-Based Qualification for Metal Laser Powder Bed Fussion," in *SAND Report*, Albuquerque, 2018.

[6] R. Becker, "The Effect of Porosity Distribution on Ductile Failure," *Journal of Mech. Phys. Solids,* vol. 35, no. 5, pp. 577-599, 1987.

[7] T. M. Mower and M. J. Long, "Mechanical Behavior of Additive Manufactured, Powder-Bed Laser-Fused Materials," *Materials Science and Engineering,* vol. 651, pp. 198-213, 2016.

[8] Y. J. Liu, S. Li, H. L. Wang, Y. Hao, R. Yang, T. B. Sercombe and L. C. Zhang, "Microstructure, Defects, and Mechanical Behavior of Beta-Type Titanium Porous Structures Manufactured by Electron Beam Melting and Selective Laser Melting," *Acta Materials,* vol. 113, pp. 56-57, 2016.

[9] Z. G. Lui, W. H. Wong and T. F. Guo, "Void Behaviors from Low to High Triaxialities: Transition from Void Collapse to Void Coalescence," *International Journal of Plasticity,* vol. 84, pp. 183-202, 2016.

[10] A. BauerieB, T. Sharowsky and C. Korner, "Defect Generation and Propagation Mechanism During Additive Manufacturing by Selective Beam Melting," *Journal of Materials Processing Technology,* vol. 214, no. 11, pp. 2522-2528, 2014.

[11] E. Jost, J. Miers, A. Robinson, D. Moore and C. Saldana, "Effects of Spatial Energy Distribution on Defects and Fracture of LPBF 316L Stainless Steel," in *Solid Freeform Fabrication*, Austin, 2019.

[12] A. Korbel and P. Martin, "Microstructural Events of Macroscopic Strain Localization in Prestrain Tensile Specimens," *Act Metallurgica,* vol. 36, no. 9, pp. 2575-2586, 1988.

[13] B. Jared, B. Boyce, J. Madison, J. Rodelas and B. Salzbrenner, "Defect Characterization for Material Assurance in AM Metals," Sandia National Laboratories, Albuquerque, 2016.

[14] A. du Plessis, I. Yadroitsec, I. Yadroitsava and S. G. Le Roux, "X-Ray Microcomputed Tomography in Additive Manufacturing," *3D Printing and Additive Manufacturing,* vol. 5, pp. 227-247, 2018.

[15] M. S. Fenandes de Lima and S. Sankare, "Microstructure and Mechanical Behavior of Laser Additive Manufactured AISI 315 Stainless Steel," *Materials and Design,* vol. 55, pp. 526-532, 2014.

[16] Volume Graphics, "Analyzing, Testing, Measuring," Volume Graphics, 2020. [Online]. Available: volumegraphics.com/en/products.html. [Accessed 20 February 2020].

[17] N. Sanaei, A. Fatemi and N. Phan, "Defect Characterization and Analysis of Their Variability in L-PBF Additive Manufacturing," *Materials and Design,* vol. 182, pp. 1-22, 2019.

[18] Avizo, "3D Visualization and Analysis Software," ThermoFischer, 2020. [Online]. Available: https://www.thermofisher.com/us/en/home/industrial/electron-microscopy/electron-microscopy-instruments-workflow-solutions/3d-visualization-analysis-software.html. [Accessed 20 February 2020].

[19] D. R. Eo, S. H. Park and J. W. Cho, "Inclusion Evolution in Additively Manufactured 316L Stainless Steel by Laser Metal Deposition Process," *Materials and Design,* vol. 155, pp. 212-219, 2018.

[20] H. Taheri, M. Rasgud Bin Mohammad Shoaib, L. Koester, T. Bigelow and P. C. Collins, "Powder-Based Additive Manufacturing - A Review of Types of Defects, Generation Mechanisms, Detection, Property Evaluation and Metrology," *International Journal of Additive and Subtractive Materials Manufacturing,* vol. 1, no. 2, pp. 172-209, 2017.

[21] M. N. Ahsan, A. J. Pinkerton, R. J. Moat and J. Shakleton, "A Comparative Study of Laser Direct Metal Deposition Characteristics Using Gas and Plasma-Atomized Ti-6Al-4V Powders," *Materials Science and Engineering: A,* vol. 528, no. 25-26, pp. 7648-7657, 2011.

[22] G. K. Ng. , A. E. Jarfors, G. Bi and H. Y. Zheng, "Porosity Formation and Gas Bubble Retention in Laser Metal Deposition," *Applied Physics A: Materials Science and Processing,* vol. 97, pp. 641-649, 2009.

[23] J. Gockel, N. KlingBeil and S. Bontha, "A Closed-Form Solution for the Effect of Free Edges on Melt Pool Geometry and Solidification Microstructure in Additive Manufacturing of Thin-Wall Geometries," *Metallurgical and Materials Transactions: Process Metallurgy and Materials Processing Science,* vol. 47, no. 2, pp. 1400-1408, 2016.

[24] F. H. Kim and S. P. Moylan, "Literature Review of Metal Additive Manufacturing Defects," *NIST Additive Manufacturing Series ,* vol. 100, no. 16, pp. 1-17, 2018.

[25] G. Ameta, R. Lipman, S. Moylan and P. Witherell, "Investigating the Role of Geometric Dimensioning and Tolerancing in Additive Manufacturing," *Journal of Mechanical Design,* vol. 137, no. 11, pp. 1-10, 2015.

[26] L. Schild, A. Kraemer, D. Reiling, H. Wu and G. Lanza, "Influence of Surface Roughness on Measurement Uncertainty in Computed Tomography," in *8th Conference on Industrial Computed Tomography*, Wels, Austria, 2018.

[27] A. Townsend, N. Senin, L. Blunt, R. K. Leach and J. S. Taylor, "Surface Texture Metrology for Metal Additive Manufacturing: a Review," *Precision Engineering,* vol. 46, pp. 34-47, 2016.

[28] A. Weckenmann, T. Estler, G. Peggs and D. McMurthy, "Probing Systems in Dimensional Metrology," *CIRP Annals,* vol. 53, pp. 657-684, 2004.

[29] J. E. Spowart, "Automated Serial Sectioning for 3-D Analysis of Microstructures," *Scripta Materialia,* vol. 55, no. 1, pp. 5-10, 2006.

[30] D. Cerniglia, M. Scafidi, A. Pantano and J. Rudlin, "Inspection of Additive Manufactured Layered Components," *Ultrasonics,* vol. 62, pp. 292-298, 2015.

[31] S. C. Kottilingam, L. Going and E. DehghanNiri, "Method and System for Thermographic Inpsection of Additive Manufacture Parts". United States of America Patent US 2018/0104742 A1, 19 April 2018.

[32] F. H. Kim, S. P. Moylan, E. J. Garboczi and J. A. Slotwinski, "Investigation of Pore Structure in Cobalt Chrome Additively Manufactured Parts Using X-ray Computed Tomography and Three-Dimensional Image Analysis," *Additive Manufacturing,* vol. 17, pp. 23-38, 2017.

[33] A. du Plessis, S. G. le Roux, G. Booysen and J. Els, "Directionality of Cavities and Porosity Formation in Powder-Bed Laser Additive Manufacturing of Metal Components Investigated Using X-Ray Tomography," *3D Printing and Additive Manufacturing,* vol. 3, no. 1, pp. 48-55, 2016.

[34] A. D. Dressler, E. W. Jost, J. C. Miers, D. G. Moore, C. C. Seepersad and B. L. Boyce, "Heterogeneities Dominate Mechanical Performance in Additively Manufactured Metal Lattice Struts," *Additive Manufacturing,* vol. 28, pp. 692-703, 2019.

[35] H. D. Carlton, A. Haboub, G. Gallegos, D. Parkinson and A. A. MacDowell, "Damage Evolution and Failure Mechanisms in Additively Manufactured Stainless Steel," *Materials Science and Engineering: A,* vol. 651, pp. 406-414, 2016.

[36] B. Pan, D. Wu and Z. Wang, "Internal Displacement and Strain Measurement Using Digital Volume Correlation: A Least-Squares Framework," *Measurement Science and Technology,* vol. 23, pp. 1-13, 2012.

[37] F. Kharfi, "Demonstrations and Practical Examples, Imaging and Radioanalytical Techniques in Interdisciplinary Research," in *Mathematics and Physics of Computed Tomography (CT)*, Intech Open, 2013, pp. 81-106.

[38] P. P. Vaidyanathan, "Generalizations of the Sampling Theorem: Seven Decades of Nyquist," *IEEE Transactions on Circuits and Systems,* vol. 48, no. 9, pp. 1094-1109, 2001.

[39] D. Hatcher, "Operational Principles for Cone-Beam Computed Tomography," *Journal of the American Dental Association,* vol. 141, pp. 3S-6S, 2010.

[40] A. Cantatore and P. Müller, "Introduction to Computed Tomography," DTU Mechanical Engineering, 2011.

[41] B. L. Boyce, S. L. B. Kramer, H. E. Fang, T. E. Cordova, M. K. Neilsen, K. Dion, A. K. Kaczmarowski, E. Karasz, L. Xue, A. J. Gross, A. Ghahremaninezhad, K. Ravi-Chandar, S. P. Lin, S. W. Chi, J. S. Chen, E. Yreux, M. Ruter, D. Qian, Z. Zhou, S. Bhamare, D. O'Connor, S. Tang, K. Elkhodary, J. Zhao, J. Hochhalter, A. Cerrone, A. Ingraffea, P. Wawrzynek, B. Carter, J. Emery, M. Veilleux, P. Yang, Y. Gan, X. Zhang, Z. Chen, E. Madenci, B. Kilic, T. Zhang, E. Fang, P. Liu, J. Lua, K. Nahshon, M. Miraglia, J. Cruce, R. DeFrese, E. Moyer, S. Brinckmann, L. Quinkert, K. Pack, M. Luo and T. Wierzbicki, "The Sandia Fracture Challenge: blind round robin predictions of ductile tearing," *International Journal of Fractography,* vol. 186, pp. 5-68, 2014.

[42] B. L. Boyce, S. L. B. Kramer and L. Xue, "The Second Sandia Fracture Challenge: predictions of ductile failure under quasi-static and moderate-rate dynamic loading," *International Journal of Fracture,* vol. 198, pp. 5-100, 2016.

[43] S. L. B. Kramer, A. Jones and B. L. Boyce, "The Third Sandia Fracture Challenge: predictions of ductile fracture in additively manufactured metal," *International Journal of Fracture,* vol. 218, pp. 5-61, 2019.

[44] D. F. Susan, T. B. Crenshaw and J. S. Gearhart, "The Effects of Casting Porosity on the Tensile Behavior of Investment Cast 17-4PH Stainless Steel," *Journal of Materials Engineering and Performance,* vol. 24, pp. 2917-2924, 2015.

[45] Z. Wang, T. A. Palmer and A. M. Beese, "Effect of Processing Parameters on Microstructure and Tensile Properties of Austenitic Strainless Steel 304L Made by Directed Energy Deposition Additive Manufacturing," *Acta Materialia,* vol. 110, pp. 226-235, 2016.

[46] W. F. Frazier, "Metal Additive Manufacturing: A Review," *Journal of Materials Engineering and Performance,* vol. 23, pp. 1917-1928, 2014.

[47] F. H. Kim, S. P. Moylan, T. Q. Phan and E. J. Garboczi, "Investigation of the Effect of Artificial Internal Defects on the Tensile Behavior of Laser Powder Bed Fusion 17-4 Stainless Steel Samples: Simultaneous Tensile Testing and X-ray Computed Tomography," *Experimental Mechanics,* 2020.

[48] A. Leicht and E. O. Wennberg, "Analyzing the Mechanical Behavior of Additive Manufactured Ti-6Al-4V Using Digital Image Correlation," Department of Materials and Manufacturing Technology at Chalmers University of technology, Gothenburg, 2015.

[49] R. J. Bourcier, R. E. Smelser, D. A. Koss and O. Richmond, "The Influence of Porosity on the Deformation and Fracture of Alloys," Office of Naval Research, Arlington, 1984.

[50] A. R. Ragab, "Application of an Extended Void Growth Model With Strain Hardening and Void Shape Evolution to Ductile Fracture Under Axisymmetric Tension," *Engineering Fracture Mechanics,* vol. 71, pp. 1515-1534, 2004.

[51] A. R. Ragab, "A Model for Ductile Fracture Based on Internal Necking of Spheroidal Voids," *Acta Materialia,* vol. 52, no. 13, pp. 3997-4009, 2004.

[52] M. E. Torki, C. Tekoglu, J.-B. Leblond and A. A. Benzerga, "Theoretical and Numerical Analysis of Void Coalescence in Porous Ductile Solids Under Arbitrary Loadings," *International Journal of Plasticity,* vol. 91, pp. 160-181, 2017.

[53] A. A. Benzerga, J.-B. Leblond, A. Needleman and V. Tvergaard, "Ductile Failure Modeling," *International Journal of Fracture,* vol. 201, pp. 29-80, 2016.

[54] M. Jirasek, "Objective Modeling of Strain Localization," *European Journal of Environmental and Civil Engineering,* vol. 6, pp. 1119-1132, 2011.

[55] B. Croom, H. Jin, P. Noell, B. Boyce and X. Li, "Collaborative Ductile Rupture Mechanisms of High-Purity Copper Identified by In Situ X-ray Computed Tomography," *Acta Materialia,* vol. 181, pp. 377-384, 2019.

[56] Z. Shan and A. M. Gokhale, "Digital Image Analysis and Microstructure Modeling Tools for Microstructure Sensitive Desgin Materials," *International Journal of Plasticity,* vol. 20, no. 7, pp. 1347-1370, 2004.

[57] H. Singh and Y. Mao, "Application of digital image processing for implementation of complex realistic particle shapes/morphologies in computer simulated heterogeneous microstructures," *Modelling and Simulation in Materials Science and Engineering,* vol. 14, pp. 351-363, 206.

[58] L. Qian, H. Toda, K. Uesugi, M. Kobayashi and T. Kobayashi, "Direct Observation and Image-Based Simulation of Three-Dimensional Tortuous Crack Evolution inside Opaque Materials," *Physical Review Letters,* vol. 100, no. 115505, pp. 1-4, 2008.

[59] A. Bulijac, L. Helfen, F. Hild and T. F. Morgeneyer, "Effect of void arrangement on ductile damage mechanisms in nodular graphite cast iron: in-situ 3D measurements," *Engineering Fracture Mechanics,* vol. 192, pp. 242-261, 2018.

[60] A. Bulijac, F. Hild, L. Helfen and T. F. Morgeneyer, "On Deformation and damage micromechanisms in strong work hardening 2198 T3 Aluminum alloy," *Acta Materialia,* vol. 149, pp. 29-45, 2018.

[61] C. C. Roth, T. F. Morgeneyer, Y. Cheng, L. Helfen and D. Mohr, "Ductile damage mechanisms under shear-dominated loading: In-situ tomography experiments on dual phase steel and localization analysis," *International Journal of Plasticity,* vol. 109, pp. 169-192, 2018.

[62] E. Maire and P. J. Withers, "Quantitative X-ray Tomography," *Internation Materials Reviews,* vol. 59, no. 1, pp. 1-43, 2014.

[63] T. L. Burnett, S. A. McDonald, A. Gholinia, R. Geurts, M. Janus, T. Slater, S. J. Haigh, C. Ornek, F. Almuaili, D. L. Engelberg, G. E. Thompson and P. J. Withers, "Correlative Tomography," *Science Reports,* vol. 4, no. 4711, 2015.

[64] C. Landron, E. Maire, O. Bouaziz, J. Adrien, L. Lecarme and A. Bareggi, "Validation of Void Growth Models Using X-ray Microtomography Characterization of Damage in Dual Phase Steels," *Acta Materialia,* vol. 59, no. 20, pp. 7564-7573, 2011.

[65] A. Buljac, C. Jailin, A. Mendoza, J. Neggers, T. Taillandier-Thomas, A. Bouterf, F. Hild and S. Roux, "Digital Volume Correlation: Review of Progress and Challenges," *Experimental Mechanics,* vol. 58, pp. 661-708, 2018.

[66] V. Cnudde and M. N. Boone, "High-Resolution X-Ray Computed Tomography in Geosciences: A Review of the Current Technology and Applications," *Earth-Science Reviews,* vol. 123, pp. 1-17, 2013.

[67] G. N. Hounsfield, "Compurterized Transverse Axial Scanning (Tomography): Part 1. Description of System," *British Journal of Radiology,* vol. 46, pp. 1016-1022, 1973.

[68] J. Ambrose, "Computerized Transverse Axial Scanning (Tomography): Part 2. Clinical Application," *The British Journal of Radiology,* vol. 46, no. 552, pp. 1023-1047, 1976.

[69] A. K. Ommaya, G. Murray, J. Ambrose, A. Richardson and G. Hounsfield, "Computerized Axial Tomography: Estimation of Spatial and Density Resolution Capability," *The British Journal of Radiology,* vol. 49, pp. 604-611, 1976.

[70] F. Natterer, The Mathematics of Computerized Tomography, New York: Wiley and Sons, 1986.

[71] B. De Man, J. Nuyts, P. Dupont, G. Marchal and P. Suetens, "Metal Streak Artifacts in X-ray Computed Tomography: A Simulation Study," in *1998 IEEE Nuclear Science Symposium Conference Record*, Toronto, 1998.

[72] G. H. Glover and N. J. Pelc, "Nonlinear Partial Volume Artifacts in X-ray Computed Tomography," *Medical Physics,* vol. 7, no. 3, pp. 238-248, 1980.

[73] A. Lyckegaard and P. Tafforeau, "Correction of Ring Artifacts in X-Ray Tomographic Images," *International Journal of Tomography and Statistics,* vol. 18, no. F11, pp. 1-9, 2011.

[74] L. Borg, J. Frikel, J. S. Jorgensen and E. T. Quinto, "Analyzing Reconstruction Artifacts fro Arbitrary Incomplete X-Ray CT Data," *Imaging Sciences,* vol. 11, no. 4, pp. 2786-2814, 2018.

[75] H. Villarrraga-Gomez, J. D. Thousand and S. T. Smith, "Empirical Approaches to Uncertainty Analysis of X-Ray Computed Tomography Measurements: A Review with Examples," *Precsion Engineering,* vol. 64, pp. 249-268, 2020.

[76] B. Salzbrenner, J. Rodelas, J. Madison, B. Jared, L. Swiler, Y.-L. Shen and B. Boyce, "High-Throughput Stochastic Tensile Performance of Additively Manufactured Stainless Steel," *Journal of Materials Processing Technology,* vol. 241, pp. 1-12, 2017.

[77] Galil Motion Control, "DMC-30000: Manual Rev. 1.3c2," October 2019. [Online]. Available: http://www.galilmc.com/download/manual/dmc-30000-r13c2-manual.pdf. [Accessed 3 March 2020].

[78] B. Pan, K. Qian, H. Xie and A. Asundi, "Two-Dimensional Digital Image Correlation for In-Plane Displacement and Strain Measurement: A Review," *Measurement Science and Technology,* vol. 20, p. 17, 2009.

[79] H. Qiao, T. G. Murthy and C. Saldana, "Structure and Deformation of Gradient Metal Foams Produced by Machining," *Journal of Manufacturing Science and Engineering,* vol. 141, p. 7, 2019.

[80] W. Wcislik, "Experimental Determination of Critical Void Volume Fraction f for the Gurson Tvergaard Needleman (GTN) Model," *Procedia Structural Integrity ,* vol. 2, pp. 1676-1683, 2016.

[81] R. A. Hardin and C. Beckermann, "Effect of Porosity on Deformation, Damage, and Fracture of Cast Steel," *The Minerals, Metals, and Materials Society and ASM*

International: Metallurgical and Materials Transactions A, vol. 44A, pp. 5316-5332, 2013.

[82] A. A. Benzerga and J.-B. Leblond, "Ductile Fracture by Void Growth to Coalescence," *Advances in Applied Mechanics,* Vols. 169-305, p. 44, 2010.

[83] M. Shakoor, A. Bulijac, J. Neggers, F. Hild, T. F. Morgeneyer, L. Helfen, M. Bernacki and P.-O. Bouchard, "On the choice of boundary conditions for micromechanical simulations based on 3D imaging," *International Journal of Solids and Structures,* vol. 112, pp. 83-96, 2017.

[84] C. E. Ingles, "Stresses in a Plate due to the Presence of Cracks and Sharp Corners," *Trans. Institute of Naval Architects,* vol. 55, pp. 219-230, 1913.

[85] F. Scheyvaerts and T. Pardoen, "A New Model for Void Coalescence," *International Journal of Damage Mechanics,* vol. 19, pp. 95-126, 2010.

[86] H. Yu, K. Tieu, C. Lu, Y. Lou, X. Liu, A. Godbole and C. Kong, "Tensile Fracture of Ultrafine Grained Aluminum 6061 Sheets by Asymmetric Cryorolling fo Microforming," *International Journal of Damage Mechanics,* vol. 23, no. 8, pp. 1077-1095, 2014.

[87] A. Bulijac, V.-M. T. Navas, M. Shakoor, A. Bouterf, J. Neggers, M. Bernacki, P.-O. Bouchard, T. F. Morgeneyer and F. Hild, "On the calibration of elastoplastic parameters at the microscale via X-ray microtomography and digital valume correlation for the simulatoin of ductile damage," *European Journal of Mechanics - A/Solids,* vol. 72, pp. 287-297, 2018.

[88] A. Hosokawa, D. S. Wilkinson, J. Kang and E. Maire, "Effect of Triaxiality on Void Growth and Coalescence in Model Materials Investigated by X-ray Tomography," *Acta Matterialia,* vol. 60, no. 6-7, pp. 2829-2839, 2012.

[89] H. Taud, R. Martinez-Angeles, J. Parrot and L. Hernandez-Escobedo, "Porosity Estimation Method by X-Ray Computed Tomography," *Journal of Petroleum Science and Engineering,* vol. 47, no. 3-4, pp. 209-217, 2005.

[90] G. Ziolkowski, E. Chlebus, P. Szymckzyck and J. Kurzac, "Application of X-Ray CT Method for Discontinuity and Porosity Detection in 316L Stainless Steel Parts Produced with SLM Technology," *Archives of Civil and Mechanical Engineering,* vol. 14, pp. 608-614, 2014.

[91] M. Sezgin and B. Sankur, "Survey Over Image Thresholding Techniques and Quantitative Performance Evaluation," *Journal of Electronic Imaging,* vol. 13, no. 1, pp. 146-168, 2004.

[92] T. Chan and L. Vese, "Acrive Contours Without Edges," *IEEE Transactions of Image Processing,* vol. 10, no. 2, pp. 266-277, 2001.

[93] P. Iassonov, T. Gebrenegus and M. Tuller, "Segmentation of X-ray Computed Tomography Images of Porous Materials: A Crucial Step for Characterization and Quantitative Analysis of Pore Structures," *Water Resources Research,* vol. 45, pp. 1-12, 2009.

[94] R. Chou, A. Ghosh, S. C. Chou, M. Paliwal and M. Brochu, "Microstructure and Mechanical Properties of Al10SiMg Fabricated by Pulsed Laser Powder Bed Fusion," *Materials Science and Engineering,* vol. 689, pp. 53-62, 2017.

[95] I. Carreras, V. Kaynig, C. Rueden, K. Eliceiri, J. Schindelin, A. Cardona and H. S. Seung, "Trainable Weka Segmentation: A Machine Learning Tool for Microscopy Pixel Classification," *Bioinformatices,* vol. 33, p. 15, 2017.

[96] L. Assirati, "Performing Edge Detection by Difference of Gaussians Using q-Gaussian Kernals," *Journal of Physics: Conference Series,* vol. 490, pp. 1-4, 2013.

[97] S. Arseneau, "Structure Tensor: Tutorial and Demonstration of the Uses of Structure Tensors Using Gradient Representation," Carnegie Mellon University: Robotics Institute, 21 September 2006. [Online]. Available: https://www.cs.cmu.edu/~sarsen/structureTensorTutorial/. [Accessed 7 January 2020].

[98] T. K. Ho, "The Random Subspace Method for Constructing Decision Forests," *IEEE Transactions on Pattern Analysis and Machine Intelligence,* vol. 20, no. 8, pp. 832-844, 1998.

[99] K. C. Yee and M. E. Mear, "Effect of Void Shape on the Macroscopig Response of Non-Linear Porous Solids," *International Journal of Plasticity,* vol. 12, no. 1, pp. 45-68, 1996.

[100] C. Maurer, Q. Rensheng and V. Raghavan, "A Linear Time Algorithm for Computeing Exact Euclidean Distance Transforms of Binary Images in Arbitratry Dimensions," *IEEE Transactions on Pattern Anaysis and Machine Intelligence,* vol. 25, no. 2, pp. 265-270, 2003.

[101] M. Inui, N. Umezu and R. Shimane, "Shringking Sphere: A Parallel Algorithm for Computing the Thickness of 3D Objects," *Computer Aided Design and Applications,* vol. 13, no. 2, pp. 199-207, 2016.

[102] M. G. Kendall and A. Stuart, The Advanced Theory of Statistics: Volume 2 Inference and Relationship, New York: Hafner Publishing Company, 1961.

[103] T. D. Ngo, A. Kashani, G. Imbalzano, K. T. Nguyen and D. Hui, "Additive Manufacturing (3D Printing): A Review of Materials, Methods, Applications, and Challenges," *Composites Part B: Engineering,* vol. 143, pp. 172-196, 2018.

[104] O. Fergani, F. Berto, T. Welo and S. Y. Liang, "Analytical Modelling of Residual Stress in Additive Manufacturing," *Fatigue and Fracture of Engineering Materials and Structures,* vol. 40, pp. 971-978, 2017.

[105] H. Liu, T. Sparks and F. Liou, "Residual Stress and Deformation Modelling for Metal Additive Manufacturing Processes," in *Proceedings of the World Congress on Mechanical, Chemical, and Material Engineering*, 2015.

[106] J. M. Chacon, A. Caminero, E. Garcia-Plaza and P. J. Nunez, "Additive Manufacturing of PLA Structures Using Fused Deposition Modelling: Effects of Processing Parameters on Mechanical Properties and Their Optimal Selection," *Materials and Design,* vol. 124, pp. 143-157, 2017.

[107] D. Garcia, Z. Wu, J. Y. Kim, H. Z. Yu and Y. Zhu, "Heterogeneous Materials Deisng in Additive Manufacturing: Model Calibrations and Uncertainty-Guided Model Selection," *Additive Manufacturing,* vol. 27, pp. 61-71, 2019.

[108] G. Dong, Y. Tang and Y. F. Zhao, "A Survey of Modelling of Lattice Structures Fabricated by Additive Manufacturing," *Journal of Mechanical Design,* vol. 139, no. 10, pp. 1-13, 2017.

[109] S.-I. Park, D. W. Rosen, S.-K. Choi and C. E. Duty, "Effective Mechanical Properties of Lattice Material Fabricated by Material Extrusion Additive Manufacturing," *Additive Manufacturing,* Vols. 1-4, pp. 12-23, 2014.

[110] A. Yadollahi, N. Shamsaei, Y. Hammi and M. Horstemeyer, "Quantification of Tensile Damage Evolution in Additive Manufactured Austenitic Stainless Steels," *Materials Science and Engineering: A,* vol. 657, pp. 399-405, 2016.

[111] J. R. Rice, "The Localization of Plastic Deformation," in *Proceedings of the 14th International Congress of Theoretical and Applied Mechanics*, Delft, 1976.

[112] R. J. Asaro and J. R. Rice, "Strain Localization in Ductile Single Crystals," United States Energy Research and Development Administration, Providence, 1977.

[113] G. Pijaudier-Cabot and Z. P. Bazant, "Nonlocal Damage Theory," *Journal of Engineering Mechanics,* vol. 113, no. 10, pp. 1512-1533, 1987.

[114] V. Tvergaard, "Material Failure by Void Coalescence in Localized Shear Bands," *International Journal of Solid Structures,* vol. 18, no. 8, pp. 659-672, 1982.

[115] M. F. Horstemeyer and S. Ramaswamy, "On Factors Affecting Localization and Void Growth in Ductile Metals: A Parametric Study," *International Journal of Damage Mechanics,* vol. 9, pp. 5-28, 2000.

[116] S. D. Antolovich and R. W. Armstrong, "Plastic Strain Localization in Metals: Origins and Consequences," *Progress in Materials Science,* vol. 59, pp. 1-160, 2014.

[117] V. Tvergaard, "Material Failure by Void Growth to Coalescence," *Advances in Applied Mechanics,* vol. 27, pp. 83-151, 1990.

[118] H. Chalal and F. Abed-Meraim, "Hardening Effects on Strain Localization Predictions in Porous Ductile Materials Using the Bifurcation Approach," *Mechanics of Materials,* vol. 91, pp. 152-166, 2015.

[119] J. Bessen, "Continuum Models of Ductile Fracture: A Review," *International Journal of Damage Mechanics,* vol. 19, pp. 3-52, 2010.

[120] A. L. Gurson, "Continuum Theory of Ductile Rupture by Void Nucleation and Growth: Part 1 Yield Criteria and Flow Rules for Porous Ductile Media," *Transactions of the ASME,* pp. 1-14, 1977.

[121] T. Pardoen and J. W. Hutchinson, "An Extended Model for Void Growht and Coalescence," *Journal of the Mechanics and Physics of Solids,* vol. 48, no. 12, pp. 2467-2512, 2000.

[122] B. J. Lee and M. E. Mear, "Axisymmetric Deformation of Power-Law Solids Containing a Dilute Concentration of Aligned Spheroidal Voids," *Journal of the Mechanics and Physics of Solids,* vol. 40, no. 8, pp. 1805-1836, 1992.

[123] M. Gologanu, J.-B. LeBlond and J. Devaux , "Approximate Models for Ductile Metals containing Non-Spherical Voids - Case of Axisymmetric Prolate Ellipsiodal Cavaties," *Journal of the Mechanics and Physics of Solids,* vol. 41, no. 11, pp. 1723-1754, 1993.

[124] M. Gologanu, J.-B. Leblond and J. Devaux, "Approximate Models for Ductile Metals Conataining Nonspherical Voids - Case of Axisymmetric Oblate Ellipsiodal Cavities," *Journal of Engineering Material Technology,* vol. 116, pp. 290-297, 1994.

[125] Y. Zhu and Z. Pan, "Simulation of Ductile Fracture Initiation in Steels by Stress Triaxiality and Shear Stress Coupled Model," *Acta Mechanica,* vol. 35, no. 3, pp. 600-614, 2018.

[126] A. A. Benzerga, "Micromechanics of Coalescence in Ductile Fracture," *Journal of the Mechanics and Physics of Solids,* vol. 50, pp. 1331-1362, 2002.

[127] D. Morin, O. S. Hopperstad and A. Benallal, "On the Description of Ductile Fracture in Metals by the Strain Localization Theory," *International Journal of Fracture,* pp. 27-51, 2017.

[128] L. Morin, J.-B. Leblond and A. A. Benzerga, "Coalescence of Voids by Internal Necking: Theoretical Estimates and Numerical Results," *Journal of the Mechanics and Physics of Solids,* vol. 75, pp. 140-158, 2015.

[129] W. Muhammad, A. P. Brahme, O. Ibragimova, J. Kang and K. Inal, "A Machine Learning Framework to Predict Local Strain Distribution and the Evolution of Plastic Anisotropy and Fracture in Additively Manufactured Alloys," *International Journal of Plasticity,* vol. 136, pp. 1-29, 2021.

[130] MathWorks, "Neural Network Architectures," MathWorks, 2021. [Online]. Available: https://www.mathworks.com/help/deeplearning/ug/neural-network-architectures.html. [Accessed 15 Febuary 2021].

[131] I. Barsoum and J. Faleskog, "Rupture Mechanisms in Combined Tension and Shear - Micromechanics," *International Journal of Solids and Structures ,* vol. 44, pp. 5481-5498, 2007.

[132] H. Yamamoto, "Conditions for Shear Localization in the Ductile Fracture of Void-Containing Materials," *International Journal of Fracture,* vol. 14, no. 4, pp. 347-365, 1978.

[133] P. J. Noell, J. D. Carroll and B. L. Boyce, "The Mechanisms of Ductile Rupture," *Acta Materialia,* vol. 161, pp. 83-89, 2018.

[134] S. Basu and A. A. Benzerga, "On the Path-Dependence of the Fracture Locus in Ductile Materials: Experiments," *International Journal of Solids and Strucutres,* vol. 71, pp. 79-90, 2015.

[135] A. A. Benzerga, D. Surovik and S. M. Keralavarma, "On the Path-Dependence of the Fracture Locus in Ductile Materials - Analysis," *International Journal of Plasticity,* vol. 37, pp. 157-170, 2012.

[136] M. E. Torki and A. A. Benzerga, "A Mechanism of Failure in Shear Bands," *Extreme Mechanics Letters,* vol. 23, pp. 67-71, 2018.